QUANTIFICATION OF UNCERTAINTY IN THE MAGNETIC CHARACTERISTIC OF STEEL AND PERMANENT MAGNETS AND THEIR EFFECT ON THE PERFORMANCE OF A PERMANENT MAGNET SYNCHRONOUS MACHINE

A Dissertation

Submitted to the Faculty

of

Purdue University

by

Abhijit Sahu

In Partial Fulfillment of the

Requirements for the Degree

of

Master of Science

August 2019

Purdue University

West Lafayette, Indiana

THE PURDUE UNIVERSITY GRADUATE SCHOOL
STATEMENT OF DISSERTATION APPROVAL

Dr. Dionysios Aliprantis

School of Electrical and Computer Engineering

Dr. Ilias Bilionis

School of Mechanical Engineering

Dr. Steven D. Pekarek

School of Electrical and Computer Engineering

Approved by:

Dr. Dimitrios Peroulis

Head of the School Graduate Program

Dedicated to my parents Arjun and Bhagyalata, and my sister, Akankhya.

ACKNOWLEDGMENTS

I would like to express my deepest gratitude to my advisors, Prof. Dionysios Aliprantis and Dr. Ilias Bilionis for their able guidance throughout the course of this thesis. I would also like to express my gratitude to Prof. Steven D. Pekarek for agreeing to serve as a member of my committee.

I am thankful to the Power group for having made this journey so meaningful. It has been my pleasure being a part of this knowledgeable and resourceful group. Here, I would also like to express my gratitude to Rohit for helping me during the course of this thesis.

Lastly, I would like to thank my parents and my sister for having supported me throughout this journey. I am lucky to have got such a wonderful family.

This research was supported by the Grainger Center for Electric Machinery and Electromechanics (CEME) and I am thankful to them for having supported me financially during my time in Purdue.

TABLE OF CONTENTS

Page

LIST OF TABLES

Table Page

LIST OF FIGURES

Figure Page

Figure Page

Figure Page

ABSTRACT

Sahu, Abhijit M.Sc., Purdue University, August 2019. Quantification of Uncertainty in the Magnetic Characteristic of Steel and Permanent Magnets and their Effect on the Performance of a Permanent Magnet Synchronous Machine. Major Professors: Dionysios Aliprantis, Ilias Bilionis.

The numerical calculation of the electromagnetic fields within electric machines is sensitive to the magnetic characteristics of steel. However, the properties of steel are uncertain due to fluctuations in alloy composition, possible contamination, and other manufacturing process variations including punching. Previous attempts to quantify magnetic uncertainty due to punching are based on parametric analytical models of *B*-*H* curves, where the uncertainty is reflected by model parameters. In this work, we set forth a data-driven approach for quantifying the uncertainty due to punching in *B*-*H* curves. In addition to the magnetic characteristics of steel lamination, the remanent flux density (B_r) exhibited by the permanent magnets in a permanent magnet synchronous machine (PMSM) is also uncertain due to unpredictable variations in the manufacturing process. Previous studies consider the impact of uncertainties in *B*-*H* curves and B_r of the permanent magnets on the average torque, cogging torque, torque ripple and losses of a PMSM. However, studies pertaining to the impact of these uncertainties on the combined machine/drive system of a PMSM is scarce in the literature. Hence, the objective of this work is to study the effect of *B*-*H* and B_r uncertainties on the performance of a PMSM using a validated finite element simulator. Our approach is as follows. First, we use principal component analysis to build a reduced-order stochastic model of *B*-*H* curves from a synthetic dataset containing *B*-*H* curves affected by punching. Second, we model the the uncertainty in B_r and other uncertainties in *B*-*H* characteristics e.g., due to unknown state of the material composition and unavailability of accurate data in deep saturation region. Third, to

overcome the computational limitations of the finite element simulator, we replace it with surrogate models based on Gaussian process regression. Fourth, we perform propagation studies to assess the effect of B-H and B_r uncertainties on the average torque, torque ripple and the PMSM machine/drive system using the constructed surrogate models.

1. INTRODUCTION

1.1 Background

The electromagnetic fields that permeate electric machines are sensitive to the magnetic characteristics of the ferromagnetic materials employed in their construction. A robust design of an electric machine hinges on accurate numerical calculations of these fields at all operating points. Such analysis requires information regarding the nonlinear B-H function(s) of the material(s) used, which is typically reflected by a nominal curve provided in a datasheet. However, the actual B-H curve may deviate from the nominal due to difference in grain size [1] and presence of impurities in the material [2, 3], operating conditions such as temperature and frequency [4–6], and various manufacturing processes that can alter the micro-structure of the material [7–13]. Furthermore, the limited availability of accurate B-H curve data in the deep saturation region [14] introduces additional epistemic uncertainty. Quantifying the effect of these uncertainties on the performance of an electric machine is a challenging problem.

The primary cause of behavioral uncertainty in the B-H curve of a steel lamination is the manufacturing process it undergoes [15]. In particular, punching has the most noticeable influence [7, 16–18]. Previous studies have shown that the plastic stress introduced during punching deteriorate the magnetic characteristics of steel near the cut edge [13]. The effect of various punching parameters including the sharpness of the punch and die, and the cutting speed and clearance has been described in [10–12, 19]. These studies, whose main purpose was to deduce the physical mechanisms responsible for the degradation, have been conducted in controlled environments. In practice, mass production of steel laminations cannot be precisely controlled, due to unforeseen variations in the manufacturing process that are not known in advance. Thus, the unpredictable variation of these punching parameters leads to the uncertainty in B-H curves.

Furthermore, behavioral uncertainty in a B-H curve is also governed by the the material composition of its corresponding steel lamination. Depending on the type of annealing process the lamination undergoes, the grain size of silicon in it may vary [1]. As a result, its B-H curve characteristic varies [20]. Besides, steel contains impurities in the form of compounds such as Nitrogen, Sulphur, Carbon, etc.. The amount of these impurities in a steel lamination also dictate the variation in its B-H curve characteristic [3].

An additional source of magnetic uncertainty is the limited availability of B-H curve data in the deep saturation region. The maximum value of B-H data point of a material published by the manufacturers is generally well below the value that corresponds to its saturation magnetization. In literature, various methods have been proposed to extrapolate the B-H curves beyond their last recorded data points [21–23]. However, it is unlikely that the extrapolated magnetization characteristic matches with the actual physical curve [14]. One would assume that the problem could be overcome by obtaining experimental measurements at high saturation levels. Nonetheless, such measurements using Epstein frames (used by manufacturers), are prone to measurement errors [14]. Thus, modeling this epistemic uncertainty is important especially to quantify the variation in the performance of the machines operating in deep saturation region [14].

Previous attempts to quantify magnetic uncertainty are based on parametric models of the B-H curves [24, 25] where the uncertainty is reflected by model parameters. These attempts do not incorporate local variations due to punching as well. Thus, our goal in this project is to overcome the short-comings of the previous attempts and propose methodologies to quantify the behavioral and epistemic uncertainty in the experimental data set of B-H curves and as an illustrative case study, we propagate this uncertainty to the torque response of a permanent magnet synchronous machine (PMSM).

In an extended work of this study, we consider an additional uncertainty, the uncertainty of remanent flux density (B_r) of permanent magnets in the PMSM. The variation in B_r occurs due to the variability in magnetization of PMs during the manufacturing process [26], from misuse of the machine [27] and the deterioration of B_r with time [27]. In a PMSM, B_r has a significant influence on the electromagnetic behavior of the machine. Therefore, the impact of its corresponding uncertainty on the performance of the machine is considered in this extended work. A detailed account of the objectives of this thesis is provided below.

1.2 Objective of the thesis

The first objective of this work is to propose a methodology for constructing a stochastic model that can quantify the uncertainty due to punching using a dataset of *B*-*H* curves. This dataset encodes the uncertainty introduced due to the uncertain state of the punching tool. We use principal component analysis (PCA) to reduce the dimensionality of uncertainty of this dataset. Furthermore, we also model the uncertainty in *B*-*H* curves due to the unknown material composition of steel and the limited availability of accurate data in deep saturation region.

The second objective is to analyze the effect of the modeled uncertainties on the output torque of a PMSM. To achieve this objective, a finite element (FE) simulator is designed. Additional layers are added in the stator and rotor of the PMSM model in the FE simulator representing the regions that show local degradation in the magnetic characteristics of steel. These regions reflect the uncertainty in *B*-*H* curves due to punching tool variation. The material uncertainty is reflected in the *B*-*H* curves of the remaining regions of the stator and rotor. Furthermore, we also incorporate the epistemic uncertainty in deep saturation region of all the *B*-*H* curves from the dataset (reflecting punching and material uncertainty in the machine). The brute force method to propagate these uncertainties is to run a large number of simulations using the FE simulator on samples of *B*-*H* curves and obtain relevant statistics.

However, evaluation using a FE simulator is computationally expensive. Instead, we train a surrogate model by running few of these expensive simulations on samples from the entire input space and use the trained surrogate to quantify the effect of B-H curve uncertainty on the output torque of a PMSM.

Surrogate models have gained eminence in various engineering applications. But, only recently they have gained popularity in the electric machines community. Quantification and propagation of uncertainty in an electric machine due to manufacturing processes using surrogate models is presented in [25]. In [28], the authors study the effect of uncertainty in rotor eccentricity on the air gap field using polynomial chaos expansion (PCE) and [29] describes the methodology to quantify the uncertainty in the magnetic field of magnets using PCE. As dimensionality of the problem increases, the number of simulations required to train these non-intrusive polynomial chaos models grows. Thus, in this study, we use Gaussian process (GP) regression to build the surrogate model. GP regression is a powerful Bayesian technique that combines the prior assumptions about the output with input-output observations using Bayes rule to form a posterior GP that complies with the prior assumptions and the observations simultaneously. The posterior GP can be used to make point-wise prediction for any new input sample and these predictions can be made accurate by training the GP regression surrogate with adequate number of simulations. Additionally, GP regression provides information about the epistemic uncertainty due to limited data availability as well. Depending on this information, the training data can be strategically sampled.

The observed quantity of interest in this study is the output torque of a PMSM. Torque waveform computed from a magneto-static FE simulator is a vector containing magnitudes of torque corresponding to distinct rotor positions of the PMSM. Generally, the torque vector has significantly high output dimension. In this high dimensional space, the surrogate is inefficient in predicting the torque as high number of scalar functions (equal to the number of dimensions) are required to learn the torque response. Physics based models contain inherent few dominant modes which have the most influence on the output [30]. By predicting only these modes, it is possible to predict the output with significant accuracy. In this study, we use PCA to identify these dominant modes contributing to the output torque and learn them using GP regression to build the surrogate. Finally, our aim is to assess the effect of *B-H* curve uncertainty on the output torque profile of the PMSM using the surrogate model.

We extend this work further by considering the effect of uncertainty in the remanent flux density (B_r) of the permanent magnets. We study the combined impact of uncertainties in *B-H* curve and B_r on the PMSM machine/drive system. Our goal is to assess the effect of all the modeled uncertainties on the maximum average torque vs speed characteristics of the machine, minimum DC-link voltage required for the motor/drive system and the current limit of the machine operating under maximum torque per ampere (MTPA) condition.

1.3 Organization

The organization of the thesis is as follows. Chapter 2 provides an insight into the FE simulator design of a PMSM with degraded zones. In the final section of this chapter, we validate the in house code with the commercial software, *ANSYS Maxwell 2D*. Chapter 3 explains in detail the concept of PCA and its use in dimensionality reduction. Chapter 4 provides the methodology to incorporate the uncertainty in *B-H* curves due to punching defect, unpredictability in material composition and the limited availability of accurate data of saturation magnetization, and the uncertainty in remanent flux density of permanent magnets. Chapter 5 provides the methodology of constructing surrogate models using GP regression. This chapter also gives details related to the methodology used for constructing a surrogate model using GP regression that learns the principal components of the output torque. In the final section of this chapter, we construct surrogate models that learn the average torque and average flux-linkages of the machine. Chapter 6 discusses two case studies for propagating the modeled uncertainties in B-H curves to the average torque and torque ripple profiles of the PMSM. In chapter 7, we propagate the combined effect of B-H uncertainties and uncertainty in remanent flux density of permanent magnets to PMSM machine/drive system. Finally, chapter 8 provides the conclusion of the conducted studies in this research.

2. FINITE ELEMENT SIMULATOR

This chapter begins by describing the drawbacks of a linear lumped parameter model based on analytical machine equations. The second section of this chapter introduces the underlying concept of designing a two-dimensional (2-D) finite element (FE) simulator and calculating the quasi-magnetostatic field of a permanent magnet synchronous machine (PMSM) made of steel following non-linear magnetic characteristics. Additionally, we modify the FE mesh in this section to incorporate the degraded zones caused by the punching tool during manufacturing process. In the final section, we validate the finite element simulator against the results from the commercial software, *ANSYS Maxwell 2D*.

2.1 Drawbacks in analysis using a linear lumped parameter model

In this research, we consider the interior PMSM of the 2004 Toyota Prius, which has been documented in detail in [31]. The dimensions of the stator slot, teeth and back-iron are illustrated in Fig. 2.1 and the rotor and permanent magnet dimensions are illustrated in Fig. 2.2. The parameters are provided in Table 2.1. This is a 8-pole motor, rated for 400 Nm and 50 kW, at 1500 rpm. In this study, we consider a no-load system where the 3-phase currents, i_a, i_b and i_c, excite the machine for operation. Here the currents are given by

$$\begin{bmatrix} i_\mathrm{a} \\ i_\mathrm{b} \\ i_\mathrm{c} \end{bmatrix} = I_\mathrm{pk} \begin{bmatrix} \cos\left(\theta_e + \phi_c\right) \\ \cos\left(\theta_e + \phi_c - \frac{2\pi}{3}\right) \\ \cos\left(\theta_e + \phi_c + \frac{2\pi}{3}\right) \end{bmatrix} \tag{2.1}$$

where I_pk is the peak magnitude of current, ϕ_c is the current angle and θ_e is the rotor electrical angular position, given by

$$\theta_e = \omega_e t, \tag{2.2}$$

where t is the time (in s), and ω_e is the rotor angular speed (in rad/s).

For simplicity of analysis, in a linear lumped parameter model, we consider only the linear relationship between the parameters. Although these equations make the analysis simpler, they fail to capture the dynamics of the machine accurately. To analyze the machine, the q-d transformed currents in rotor reference frame are used [32]. The transformation is given by

$$\begin{bmatrix} i^r_{\text{qs}} \\ i^r_{\text{ds}} \\ i^r_{0\text{s}} \end{bmatrix} = \begin{bmatrix} \cos\theta_e & \cos\left(\theta_e - \frac{2*\pi}{3}\right) & \cos\left(\theta_e + \frac{2*\pi}{3}\right) \\ \cos\theta_e & \cos\left(\theta_e - \frac{2*\pi}{3}\right) & \cos\left(\theta_e + \frac{2*\pi}{3}\right) \\ \frac{1}{2} & \frac{1}{2} & \frac{1}{2} \end{bmatrix} \begin{bmatrix} i_a \\ i_b \\ i_c \end{bmatrix}, \tag{2.3}$$

where i_{qs}, i_{ds} and $i_{0\text{s}}$ are the q-axis, d-axis and the zero-sequence currents respectively. However, since we are dealing with balanced sinusoidal currents, the zero-sequence current is absent [32]. Thus, using these transformations, the state of the machine can be defined by the q- and d- axes voltages.

$$v^r_{\text{qs}} = r_s i^r_{\text{qs}} + \omega_e \lambda^r_{\text{ds}} + \frac{d\lambda^r_{\text{qs}}}{dt}, \tag{2.4}$$

$$v^r_{\text{ds}} = r_s i^r_{\text{ds}} + \omega_e \lambda^r_{\text{qs}} + \frac{d\lambda^r_{\text{ds}}}{dt}, \tag{2.5}$$

where r_s is the resistance of single phase winding,

$$\lambda^r_{\text{qs}} = L_q i^r_{\text{qs}} \tag{2.6}$$

and

$$\lambda^r_{\text{ds}} = L_d i^r_{\text{ds}} + \lambda'^r_m \tag{2.7}$$

where L_q is the q-axis inductance, L_d is the d-axis inductance and λ'^r_m is the flux linkage due to the permanent magnets. In a linear model, L_q and L_d are assumed to be constant. Subsequently, the torque, T, of the machine is given by [32]

$$T = \left(\frac{3}{2}\right)\left(\frac{P}{2}\right)\left(\lambda^r_{\text{ds}} i^r_{\text{qs}} - \lambda^r_{\text{qs}} i^r_{\text{ds}}\right). \tag{2.8}$$

There are a number of problems with the linear lumped parameter model. The approximation of the model assuming a linear behavior of the magnetic material is one of them. This approximation provides a linear relationship between the applied currents (i^r_{qs}, i^r_{ds}) and the flux linkages (λ^r_{qs}, λ^r_{ds}) as observed in Eqns. (2.6) and (2.7). However in reality, the behavior of the magnetic material is dictated by non-linear B-H curve affecting the relationship between the currents and flux linkages (as we will see later in this chapter). Furthermore, as L_q and L_d are assumed to be constants, the harmonics due to the stator teeth and slots of the machine are not captured by the lumped parameter model. Thereby, the torque given by Eq. (2.8) fails to capture these harmonics. In this study, we intend to quantify the effect of B-H curve uncertainty on the torque profile of a PMSM. Thus, it is important for us to model the behavior of the machine accurately so that its sensitivity to the considered uncertainties can be precisely quantified. Considering the disadvantages of the linear lumped parameter model, we use the FE analysis approach to obtain the torque waveform of the PMSM. The details on the design of a FE simulator are provided in the following sections. For simplicity of notation, henceforward, we refer to i^r_{qs} as I_q and i^r_{ds} as I_d.

2.2 Development of 2-D FE simulator

The torque produced by a PMSM is a result of interaction between the magnetic fields produced by the rotor magnets and stator currents. The interaction of these electromagnetic fields is analyzed using a 2-D FE solver. This analysis is simplified by making following assumptions. The currents are considered to flow only in the axial direction (z- axis) and the displacement current in Ampere's law is ignored [33]. Additionally, the dynamics of the machine are assumed to be fast enough to ignore the transients. Such FE solver is called a magnetostatic solver. In a magnetostatic solver, the magnetic field is obtained by solving a non-linear Poisson's equation. The following equations form the basis for deriving Poisson's equation:

$$\nabla \times \vec{H} = \vec{J}_e \tag{2.9}$$

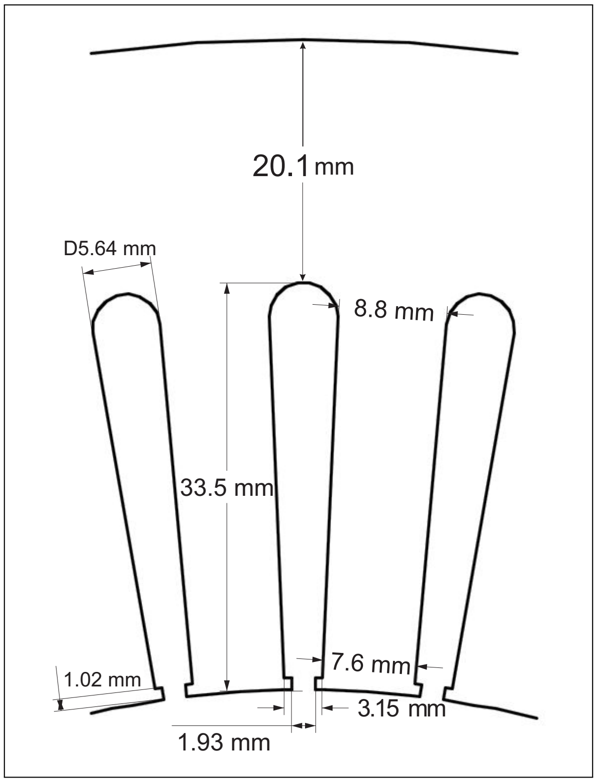

Fig. 2.1.: PMSM stator dimensions

$$\nabla \cdot \vec{B} = 0 \tag{2.10}$$

$$\vec{B} = \mu \vec{H} \tag{2.11}$$

$$\vec{B} = \nabla \times \vec{A} \tag{2.12}$$

where $\vec{H}$ is the magnetic field intensity, $\vec{B}$ is the magnetic flux density, $\vec{A}$ is magnetic vector potential (MVP), $\vec{J_e}$ is the equivalent current density which is a vector sum of current density due to the currents in the stator and perceived current density due

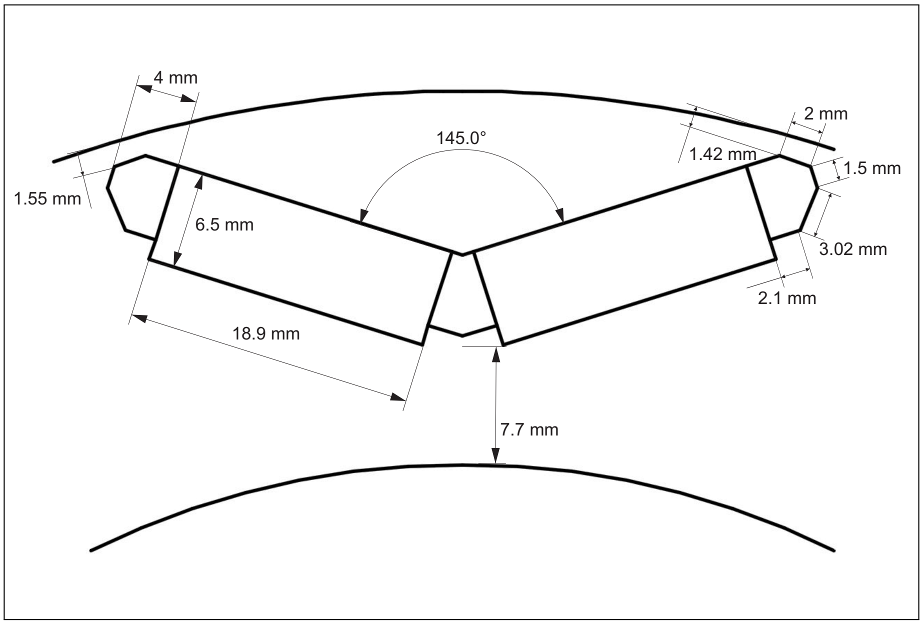

Fig. 2.2.: PMSM rotor and permanent magnet dimensions

to the magnets in the rotor, and μ is the absolute permeability of the region under consideration. From Eq. (2.9), Eq. (2.11) and Eq. (2.12), we get

$$\nabla \times \left(\nabla \times \vec{A}\right) = \mu \vec{J}_e. \tag{2.13}$$

In 2-D, Eq. (2.13) reduces to

$$\frac{\partial^2 A}{\partial x^2} + \frac{\partial^2 A}{\partial y^2} = -\mu \vec{J}_e, \tag{2.14}$$

where A and J_e are functions of x and y and correspond to the $z-$ components of the MVP and equivalent current density respectively.

Eq. (2.14) is the non-linear Poisson's equation which is equal to the Euler-Lagrange equation for an energy related functional, F, defined in a 2-D domain of interest, D. In magnetostatic problems, F is defined as

$$F = \int\int\int_D m(A)dxdy - \int\int\int_D AJdxdy - \nu_m \int\int\int \vec{B_r} \cdot (\frac{\partial A}{\partial y}\hat{a_x} - \frac{\partial A}{\partial x}\hat{a_y}) \tag{2.15}$$

Table 2.1.: Dimensions and parameters of the PMSM

Parameter	**Value**
Stator outer diameter (mm)	269
Stator inner diameter (mm)	161.93
Stator stack length (mm)	8.35
Rotor outer diameter (mm)	160.47
Air gap (mm)	0.73025
Slot depth (mm)	33.5
Slot opening (mm)	1.93
Magnet residual flux density (T)	1.23
Total number of slots ( )	48
Stator turns per coil ( )	9
Parallel circuits per phase ( )	0
Relative permeability of the magnet()	1.12

where ν_m is the absolute reluctivity of the magnet, $\hat{a}_x$ is the unit vector in x- direction, $\hat{a}_y$ is the unit vector in the y- direction, and $m(A)$ is the energy density of the system given by

$$m(A) = \frac{1}{2}\int_0^{B^2} \nu(b^2)db^2 = m(B^2), \tag{2.16}$$

where ν is the reciprocal of μ and $\vec{B_r}$ is the residual magnetic flux density of the magnet defined as

$$\vec{B_r} = \mu_o(M_x\hat{a_x} + M_y\hat{a_y}). \tag{2.17}$$

The function $A(x, y)$ that minimizes F must satisfy Eq. (2.14). Hence, instead of finding a solution to Eq. (2.14), we solve for $A(x, y)$ that minimizes F. To achieve this, D is discretized into triangular elements assuming that the current density within each element remains constant and the variation of A inside the element is linear w.r.t. x and y. Thus, inside each element, $A(x,y)$ is given by

$$A(x,y) = a + bx + cy. \tag{2.18}$$

Consider a triangle element with nodes (x_1, y_1), (x_2, y_2) and (x_3, y_3). The MVP's at these nodes is given by

$$A_1(x_1, y_1) = a + bx_1 + cy_1, \tag{2.19}$$

$$A_2(x_2, y_2) = a + bx_2 + cy_2, \tag{2.20}$$

$$A_3(x_3, y_3) = a + bx_3 + cy_3. \tag{2.21}$$

Solving Eq. (2.19), Eq. (2.20) and Eq. (2.21), we get

$$a = \frac{1}{2\triangle}[(x_2y_3 - x_3y_2)A_1 + (x_3y_1 - x_1y_3)A_2 + (x_1y_2 - x_2y_1)A_3], \tag{2.22}$$

$$b = \frac{1}{2\triangle}[(y_2 - y_3)A_1 + (y_3 - y_1)A_2 + (y_1 - y_2)A_3], \tag{2.23}$$

$$c = \frac{1}{2\triangle}[(x_3 - x_2)A_1 + (x_1 - x_3)A_2 + (x_2 - x_1)A_3]. \tag{2.24}$$

where $\triangle$ is the area of the triangle element given by:

$$\triangle = \frac{1}{2}[(x_2 - x_1)(y_3 - y_1) - (y_2 - y_1)(x_3 - x_1)]. \tag{2.25}$$

Substituting Eq. (2.19), Eq. (2.20) and Eq. (2.21) into Eq. (2.18), we get

$$A = \sum_{i=1}^{3} \alpha_i A_i. \tag{2.26}$$

where for $i = 1, 2, 3$,

$$\alpha_i(x,y) = \frac{1}{2\triangle}[p_i + q_i x + r_i y], \tag{2.27}$$

$$p_1 = x_2y_3 - x_3y_2, \tag{2.28}$$

$$p_2 = x_3y_1 - x_1y_3, \tag{2.29}$$

$$p_3 = x_1y_2 - x_2y_1, \tag{2.30}$$

$$q_1 = y_2 - y_3, \tag{2.31}$$

$$q_2 = y_3 - y_1, \tag{2.32}$$

$$q_3 = y_1 - y_2, \tag{2.33}$$

$$r_1 = x_3 - x_2, \tag{2.34}$$

$$r_2 = x_1 - x_2, \tag{2.35}$$

$$r_3 = x_2 - x_1. \tag{2.36}$$

$\alpha_i(x, y)$ are called basis functions which possess the property

$$\begin{aligned} \alpha_i(x_j, y_j) &= 1, \text{ if } i = j, \\ &= 0, \text{ if } i \neq j. \end{aligned} \tag{2.37}$$

Substituting Eq. (2.37) in Eq. (2.26), we get

$$A = \sum_{i=1}^{3} A_i \alpha_i(x, y). \tag{2.38}$$

Taking into account the discretization of the domain and linear interpolation inside the triangle elements, the functional, F, can be approximated as F_{apx} given by

$$\begin{aligned} F_{apx} = \sum_{k=1}^{K} \int\int_{\triangle^k} m(B^2) dxdy - \sum_{k=1}^{K} \int\int_{\triangle^k} AJdxdy \\ - \sum_{k=1}^{K} \nu^k \mu_0 \int\int_{\triangle^k} (M_x \frac{\partial A}{\partial y} - M_y \frac{\partial A}{\partial x}) dxdy. \end{aligned} \tag{2.39}$$

In each triangle element, k, the functional takes the form, F^k_{apx}, given by:

$$\begin{aligned} F^k_{apx} &= \int\int_{\triangle^k} m(B^2) dxdy - \int\int_{\triangle^k} AJdxdy - \nu^k \mu_0 \int\int_{\triangle^k} (M_x \frac{\partial A}{\partial y} - M_y \frac{\partial A}{\partial x}) dxdy \\ &= m(B^2)\triangle^k - \frac{J^k \triangle^k}{3}(A_1 + A_2 + A_3) - \frac{\nu^k \nu_0}{2} \sum_{i=1}^{3} A_i (M^k_x r^k_i - M^k_y q^k_i). \end{aligned} \tag{2.40}$$

In Eq. (2.40), the first term is a function of B^2 which is dependent on A (Eq. (2.12)). Thus, find F_{apx} in terms of A, B^2 needs to be calculated as a function of A. Thus, B^2 is given by

$$\begin{aligned} B^2 &= (\frac{\partial A}{\partial x})^2 + (\frac{\partial A}{\partial y})^2 = |\boldsymbol{\nabla} A|^2 \\ &= \sum_{i=1}^{3} \sum_{j=1}^{3} A^k_i A^k_j (\nabla \alpha_i \cdot \nabla \alpha_j). \end{aligned} \tag{2.41}$$

A normalized element stiffness matrix, S^k is defined such that,

$$s_{ij}^k = \triangle^k(\nabla\alpha_i \cdot \nabla\alpha_j), \tag{2.42}$$

where s_{ij}^k is the element of S^k corresponding to its i^{th} row and j^{th} column. Substituting Eq. (2.42) in Eq. (2.41), we get

$$B^2 = \frac{A^{kT} S^k A^k}{\triangle^k}. \tag{2.43}$$

The solution to Eq. (2.40) can be obtained by solving a simple linear equation when ν^k is constant or independent of B^2 which is possible if the material used in the stator and rotor of the machine exhibits linear magnetic characteristics. However, in practice, the material is non-linear in nature. Thus, an additional iterative algorithm is used to reach to the solution of A numerically that minimizes Eq. (2.40). The next subsection discusses more about the implementation of this algorithm.

Integration of the non-linear material

The absolute permeability, μ, in Eq. (2.11), for a material, varies depending on the magnetic field intensity, $\vec{H}$. At low excitation, μ increases with increase in $|\vec{H}|$ whereas at high excitation μ decreases with increase in $|\vec{H}|$ until it reaches μ_0, the absolute permeability of free space. Due to the presence of this non-linearity in the magnetic property of the material, a solution of A that minimizes F cannot be obtained analytically. Therefore, a numerical technique based on Newton-Raphson algorithm is implemented in this study to find the solution of A.

By Fermat's theorem, the partial derivative of F w.r.t A, is given by

$$\frac{\partial F}{\partial A}_{atA=A_m} = 0 = g(A_m), \tag{2.44}$$

where A_m is a vector of nodal values of A that minimizes F_{apx}, and $g = \frac{\partial F}{\partial A}$. By expanding Eq. (2.44) using Taylor's series at A_m and neglecting higher order terms, we get

$$g(A) = g(A_m) + \frac{\partial^2 F}{\partial A^2}(A - A_m). \tag{2.45}$$

Solving further, the iterative formula of Newton-Raphson is obtained which is given by

$$A^{t+1} = A^t - H^{-1} g(A^t), \tag{2.46}$$

where A^t is the value of A at t^{th} iteration of Newton-Raphson and $H = \frac{\partial^2 F}{\partial A^2}$. Substituting Eq. 2.40 in Eq. (2.44), we get

$$\begin{aligned} \frac{\partial F^k}{\partial A_i^k} &= \frac{\partial}{\partial A_i^k} m^k(B^2)\triangle^k - \frac{J^k \triangle^k}{3} - I_i^k \\ &= \triangle^k \frac{dm^k}{dB^2} \frac{\partial B^2}{\partial A_i} - \frac{J^k \triangle^k}{3} - I_i^k \end{aligned} \tag{2.47}$$

where I_i^k is considered as the equivalent nodal current due to the permanent magnets in the rotor and is given by

$$I_i^k = \frac{\nu^k \mu_0}{2} (M_x^k r_i^k - M_y^k q_i^k). \tag{2.48}$$

Solving Eq. (2.16), we get

$$\frac{dm^k}{dB^2} = \frac{1}{2} \nu(B^2). \tag{2.49}$$

Thus, using Eq. (2.49), Eq. (2.47) can be reduced to

$$\frac{\partial F^k}{\partial A_{n_i}^k} = \nu(B^2)(S^k A^k)_i - \frac{J^k \triangle^k}{3} - I_i^k. \tag{2.50}$$

Similarly following necessary substitutions, $\frac{\partial F^k}{\partial A_i^k \partial A_j^k}$ can be expanded to get the hessian matrix, H. H^k, the sub-matrix of H for each element is given by:

$$H^k(A^k) = \frac{\partial^2 F^k}{\partial A_i^k \partial A_j^k} = \nu(B^2) s_{ij} - \frac{2}{\triangle^k} \frac{d\nu(B^2)}{dB^2} (S^k A^k)_i (S^k A^k)_j \tag{2.51}$$

Substituting Eq. (2.47) and Eq. (2.51) in Eq. (2.46), the MVP at each node is evaluated iteratively till the stopping criteria is met. The stopping criteria is defined as:

$$\frac{||g(Am)||_2}{||I||_2} \leq 10^{-6} \tag{2.52}$$

where I is the vector of nodal currents of the discretized elements.

After the solution of MVP at each node is obtained, the electromagnetic torque waveform is calculated using three different algorithms. The three algorithms correspond to the Maxwell stress tensor (MST) [34], the virtual distortion of triangles [35] (VDM), and the Arkkio's [36] (Arkkios) method.

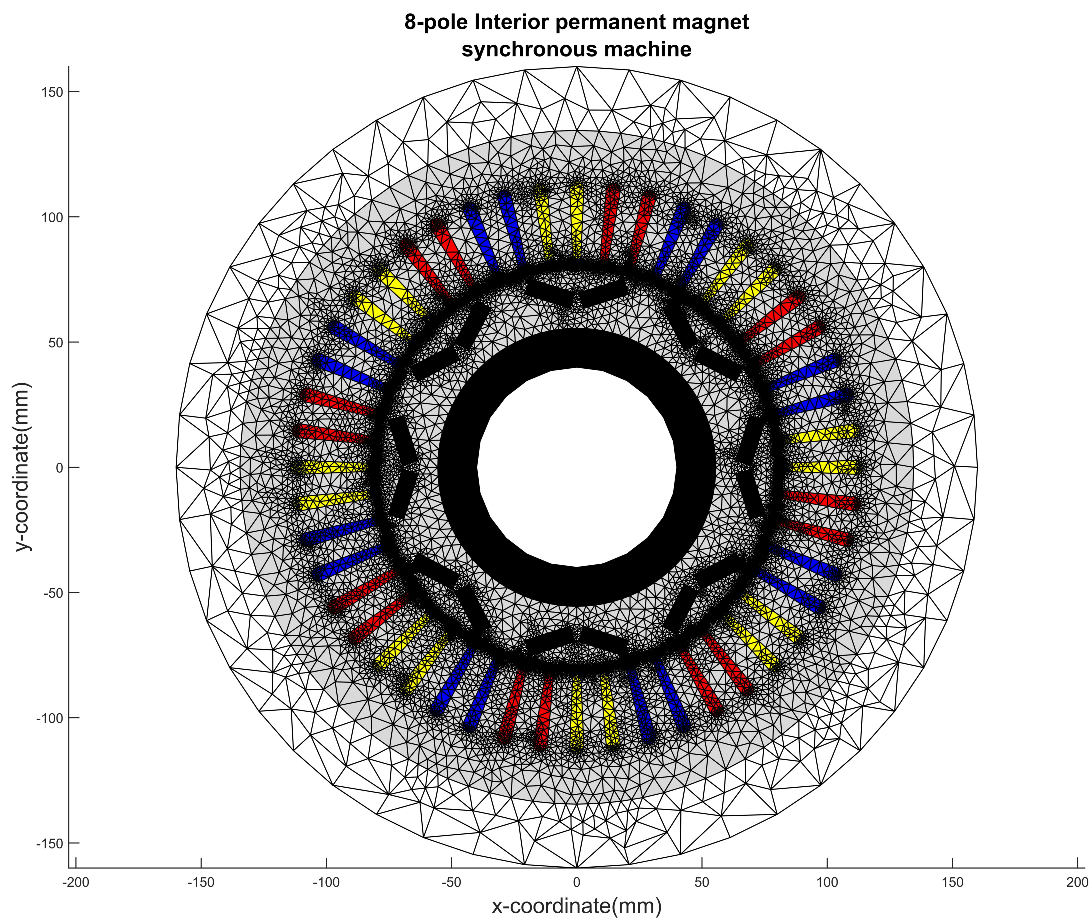

Fig. 2.3.: Discretized domain of a nominal Interior permanent magnet synchronous machine in 2-D

Incorporation of the degraded zones

The process of punching introduces plastic deformation in the region near the cut edge of the lamination, thereby deteriorating its magnetic characteristics locally [37]. This region is henceforward referred to as a degraded zone. To model this effect, we introduce a number of degraded zones in the FE mesh, as shown in Fig. 2.4. In the stator, we assume the presence of two degraded zones, as if they are caused by two separate punching tools with potentially different effect; the first is at the outer boundary, whereas the second is at the inner boundary and follows the shape of the stator teeth and slots. In the rotor, we assume 10 degraded zones; 2 zones at the outer and inner boundaries of the rotor, and 8 zones surrounding the magnet pockets. We assume that the outer and inner boundaries of the rotor are shaped by two different punching tools, whereas the 8 magnet pockets are punched by the same punching tool.

Zones are represented by 1-mm thick layers in the FE mesh [13]. The material in each degraded zone is assigned an uncertain *B-H* curve characteristic dictated by the uncertain state of its corresponding punching tool. For instance, although there are 8 geometrically separate degraded zones surrounding the magnet pockets, they all share a single *B-H* curve characteristic. The magnetization uncertainty corresponds to the combined effect of cutting speed, cutting clearance, wearing and sharpness of the punch and die of the punching tool. Henceforward, the combined effect of these parameters on the punching tool is referred to as the state of the punching tool.

2.3 Validation of the FE simulator

In the in-house FE code, we calculate the torque waveform using three different algorithms. It can be observed in Fig. 2.5 that the torque waveform computed using all of these methods produce identical results with no significant error. Henceforward, we use the Arkkio's method to compute the torque waveform for all the conducted studies.

We validate the in-house FE code against the results from the commercial software *ANSYS Maxwell 2D*. The torque waveform as a function of the mechanical rotor position, θ_{rm} and the operating points, defined by the magnitude of peak current, I_{pk}, and the current angle, ϕ_c, is obtained from *ANSYS Maxwell 2D* using the Magnetostatic solution mode. We use the Optimetrics option to feed the input parameters, θ_{rm}, I_{pk} and ϕ_c, as discrete values to *ANSYS Maxwell 2D* and evaluate the torque waveform at these values. We consider 32 equally spaced mechanical rotor positions

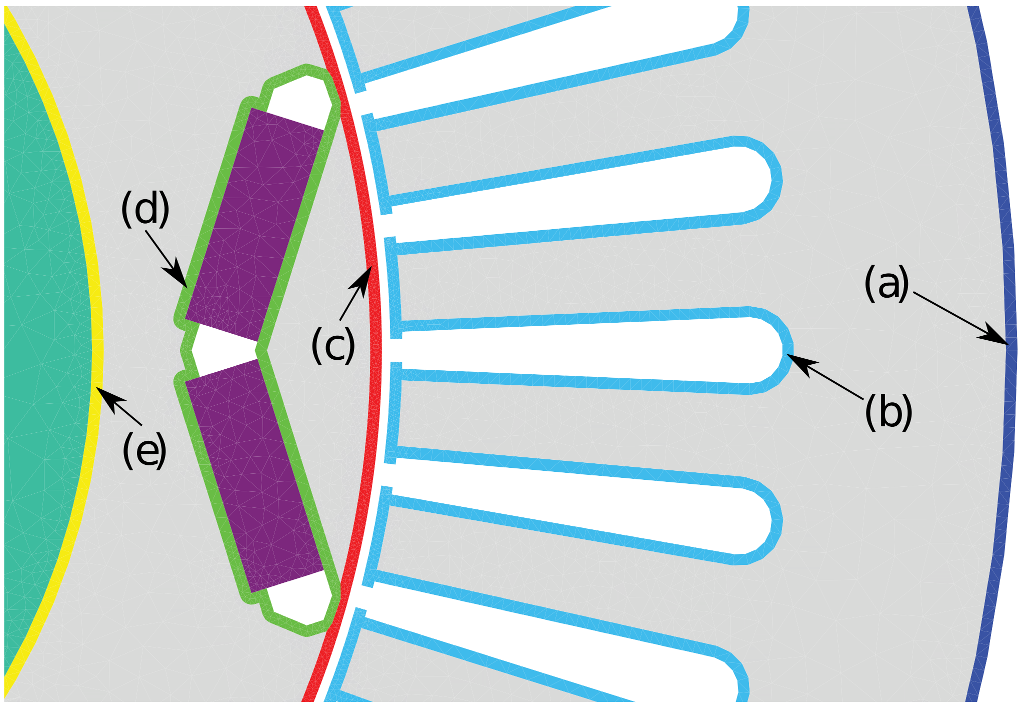

Fig. 2.4.: Illustration of degraded zones in the FE mesh of the PMSM under study. Degraded layers correspond to (a) Stator outer edge, (b) Stator teeth and slots, (c) Rotor outer edge, (d) Rotor magnet pockets and (e) Rotor inner edge

Table 2.2.: Operating points for validation study

Operating point	**Currents (A)**
1	$I_q = 10.000$ A, $I_d = 0.000$ A
2	$I_q = 9.469$ A, $I_d = -3.214$ A
3	$I_q = 7.934$ A, $I_d = -6.088$ A
4	$I_q = 5.556$ A, $I_d = -8.315$ A
5	$I_q = 2.588$ A, $I_d = -9.659$ A
6	$I_q = 70.000$ A, $I_d = 0.000$ A
7	$I_q = 66.285$ A, $I_d = -22.501$ A
8	$I_q = 55.535$ A, $I_d = -42.613$ A
9	$I_q = 38.890$ A, $I_d = -58.203$ A
10	$I_q = 18.117$ A, $I_d = -67.615$ A
11	$I_q = 130.000$ A, $I_d = 0.000$ A
12	$I_q = 123.101$ A, $I_d = -41.787$ A
13	$I_q = 103.136$ A, $I_d = -79.139$ A
14	$I_q = 72.224$ A, $I_d = -108.091$ A
15	$I_q = 33.646$ A, $I_d = -125.570$ A
16	$I_q = 190.000$ A, $I_d = 0.000$ A
17	$I_q = 179.917$ A, $I_d = -61.073$ A
18	$I_q = 150.737$ A, $I_d = -115.665$ A
19	$I_q = 105.558$ A, $I_d = -157.979$ A
20	$I_q = 49.176$ A, $I_d = -183.526$ A
21	$I_q = 250.000$ A, $I_d = 0.000$ A
22	$I_q = 236.733$ A, $I_d = -80.360$ A
23	$I_q = 198.338$ A, $I_d = -152.190$ A
24	$I_q = 138.893$ A, $I_d = -207.867$ A
25	$I_q = 64.705$ A, $I_d = -241.481$ A

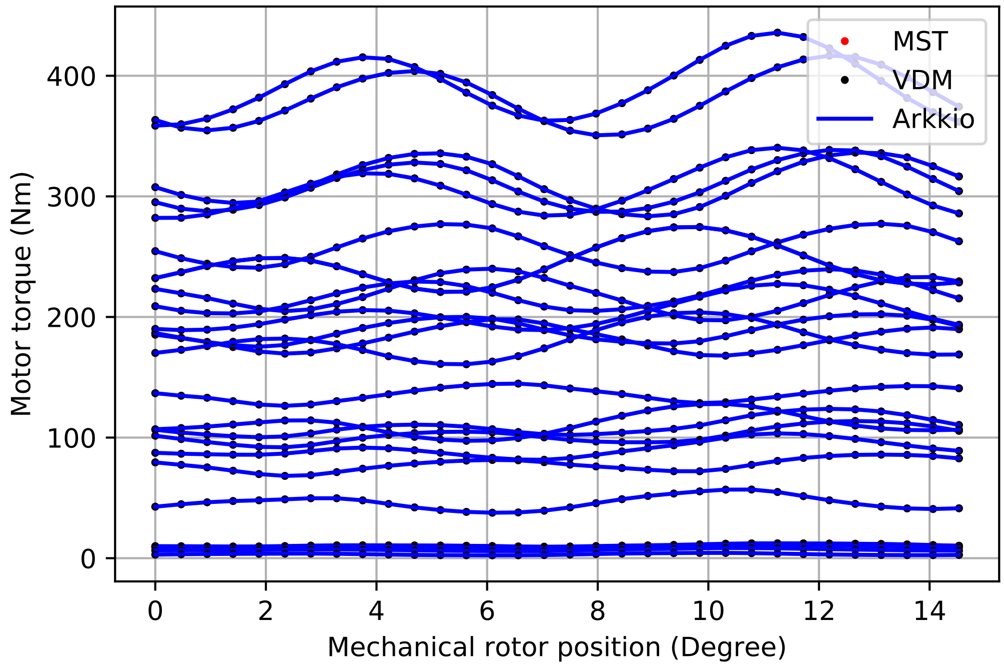

Fig. 2.5.: Computation of torque using MST, VDM and Arkkios method at 25 operating points

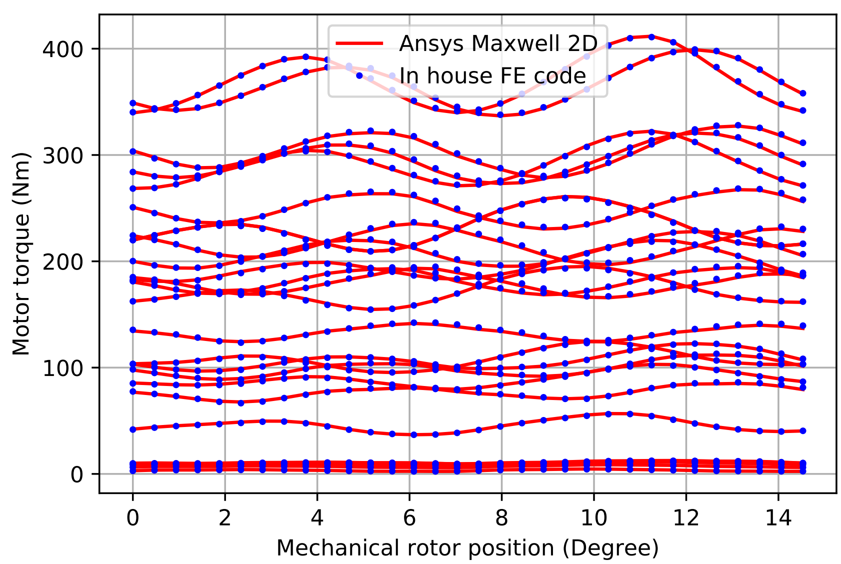

Fig. 2.6.: Validation of the FE simulator at 25 different operating points

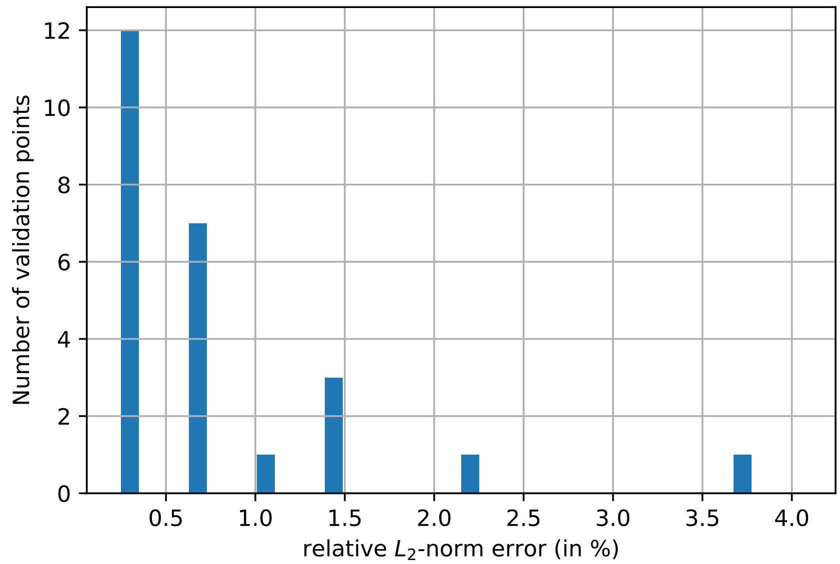

Fig. 2.7.: Histogram of L_2-norm error between the torque waveforms from *ANSYS Maxwell 2D* and in-house FE code

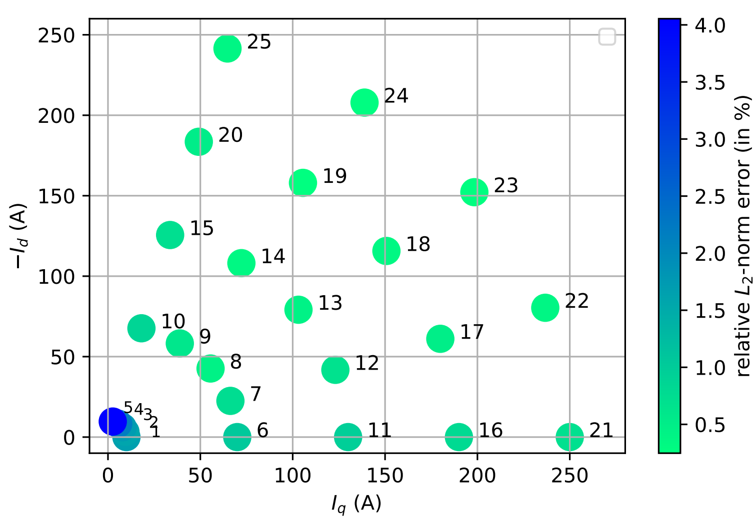

Fig. 2.8.: Relative L_2-norm error between the torque waveforms from *ANSYS Maxwell 2D* and in-house FE code in I_q-I_d plane

Table 2.3.: Relative L_2-norm error between the torque waveforms obtained from *ANSYS Maxwell 2D* and in-house FE code

Operating point	**relative L_2-norm error(%)**
1	1.6612
2	1.5919
3	1.7320
4	2.1940
5	4.0541
6	1.0626
7	0.7553
8	0.4500
9	0.6137
10	0.8749
11	0.9628
12	0.6906
13	0.4521
14	0.3600
15	0.7242
16	0.8104
17	0.5126
18	0.3567
19	0.2476
20	0.5183
21	0.7099
22	0.3849
23	0.2652
24	0.2918
25	0.3914

Table 2.4.: Torque error obtained using *ANSYS Maxwell 2D* and in-house FE code

Operating point	**Torque error(Nm)**
1	0.0312
2	0.0304
3	0.0294
4	0.0272
5	0.0241
6	0.1451
7	0.1338
8	0.0857
9	0.0970
10	0.0709
11	0.2278
12	0.2231
13	0.1680
14	0.1248
15	0.1380
16	0.2584
17	0.2272
18	0.1869
19	0.1277
20	0.1575
21	0.2734
22	0.2078
23	0.1716
24	0.1913
25	0.1599

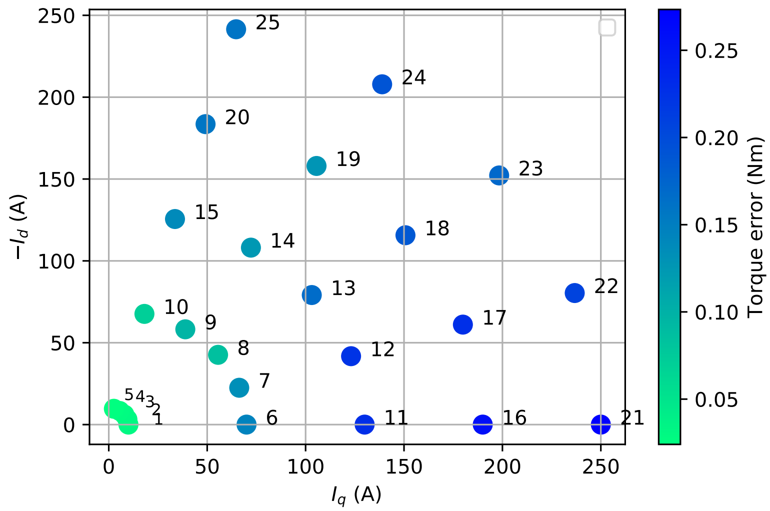

Fig. 2.9.: Torque error between the torque waveforms from *ANSYS Maxwell 2D* and in-house FE code in I_q-I_d plane

within 0 and 15 degrees where the magnitude of torque is computed. The range of 0-15 degrees is strategiclly chosen as the torque waveform for a symmetric 3 phase machine repeats itself after every 60 electrical degrees (15 mechanical degrees for a 8 pole machine as the PMSM considered in the study). For each of the considered rotor position, *ANSYS Maxwell 2D* implements an adaptive meshing technique to reduce the local error associated with the energy of the system such that between two consecutive passes, it would not exceed 0.01%. The relative L_2-norm error between the torque waveforms evaluated using *ANSYS Maxwell 2D*, $\mathbf{t}_{\text{am}}$, and the in-house FE code, $\mathbf{t}_{\text{ih}}$, is given by

$$\text{relative } L_2\text{-norm error} = \frac{\|\mathbf{t}_{\text{am}} - \mathbf{t}_{\text{ih}}\|_2}{\|\mathbf{t}_{\text{ih}}\|_2}. \tag{2.53}$$

The torque waveform is computed at 25 different operating points. I_{pk} and ϕ_c are considered at 5 equally spaced points between 10 A and 250 A, and 0 degree and 75 degrees respectively. The operating points are reported in the form of I_q and I_d in Table 2.2. It can be observed in Fig. 2.7 that the errors of 12 of the validation points are below 0.5% and 7 of them are below 1%. The error is also illustrated in the I_q-I_d

plane in Fig. 2.8 and reported in Table 2.3. It can be seen that the 5 outliers (error $> 1.25\%$) correspond to the low current region. Figs. 2.13, 2.14, 2.15, 2.16 and 2.17 illustrate the different torque waveforms with their relative L_2-norm errors. We also consider another error criteria called the torque error between the two codes where the torque error, e_t, is given by

$$e_t = \frac{\|\mathbf{t}_{\text{am}} - \mathbf{t}_{\text{ih}}\|_2}{N_r}, \tag{2.54}$$

where N_r corresponds to the number of discrete rotor positions where the magnitude of torque is computed. Fig. 2.9 shows the torque error for the 25 operating points and Table 2.4 reports them. It can be observed that although the relative L_2-norm error was high near the low current region, the torque error is high near the high current region. However, the maximum torque error is approximately around 0.25 Nm which is acceptable.

The purpose of this study is to consider the effect of *B-H* uncertainties on our quantities of interests (QoIs) where the QoIs are given by the average torque, the sixth and twelfth harmonic components of torque. Thus, it is important that the QoIs are accurately evaluated by the in-house FE code. Hence, we also calculate the difference between the QoIs obtained from *ANSYS Maxwell 2D* and the in-house FE code in our study. The magnitude of average torque at any operating point is given by

$$t_{\text{avg}} = \frac{1}{N_r} \sum_{n=1}^{N_r} t_{\text{c}}^{(n)} \tag{2.55}$$

where $t_c^{(n)}$ is the n-th value of the torque waveform, $\mathbf{t}_c$, obtained using the in-house FE code/*ANSYS Maxwell 2D*. The sixth and the twelfth harmonic components of torque are given by the discrete-fourier transform (DFT) of $\mathbf{t}_c$. The evaluation of DFT is computationally intensive. Instead, we use the Fast-fourier transform (FFT) which is computationally inexpensive. To obtain the FFT, we use the *numpy* package of *python*. Fundamentally, the DFT decomposes $\mathbf{t}_c$ such that its each component, T_k is given by

$$T_k = \sum_{n=0}^{N_r-1} t_c^{(n)} \exp\left\{ \frac{\dot{i}2\pi kn}{N_r} \right\}. \tag{2.56}$$

In this interpretation, each component, T_k is a complex number that encodes both amplitude and phase of a complex sinusoidal component, $\exp\{i2\pi kn\}$, of $t_c^{(n)}$. The sinusoid's frequency is k cycles per N_r samples. It's amplitude is given by

$$|T_k|/N_r = \sqrt{\mathrm{Re}(T_k)^2 + \mathrm{Im}(T_k)^2}/N_r \tag{2.57}$$

Since, we work with just one period of the torque waveform, the absolute value of the second component, $|T_1|/N_r$ corresponds to the magnitude of sixth harmonic component of the torque waveform and the absolute value of third component, $|T_2|/N_r$, corresponds to the magnitude of twelfth harmonic component of the torque waveform. We obtain the difference between the magnitudes of the QoIs from *ANSYS Maxwell 2D* and the in-house FE code. We plot these differences in the $I_q - I_d$ plane (see Figs. 2.10, 2.11 and 2.12)and their values are reported in Tables 2.5, 2.7 and 2.6 respectively.

ANSYS Maxwell 2D implements a quadratic interpolation of the magnetic vector potential where as in the in-house FE code, we implement a bilinear interpolation of MVP (see Eq.(2.18)). Thus, the elements of the stiffness matrix corresponding to *ANSYS Maxwell 2D* and the in-house FE code will be different which results in different values of MVPs. Consequently, the torque calculated from the two sources will be different as well. However, if the triangular elements are sufficiently small, the deviation is expected to be small. The mesh used by *ANSYS Maxwell 2D* is different from the mesh of in-house FE code which is yet another factor contributing to the error. Considering these sources of error, the discrepancy between the quantities evaluated from in-house FE code and *ANSYS Maxwell 2D* is acceptable.

In addition to validating the torque waveforms obtained from the in-house FE code at 25 operating points, we also study the change in the QoIs with the change in *B-H* curve of steel from both the solvers. We prepare the study by perturbing the

B-H curve such that it has a slope greater than the nominal B-H curve. To obtain the perturbed curve, we decrease the H-values of the nominal curve by 30% at same B-values (as the nominal curve) and extrapolate the generated curve with a slope of μ_0. *ANSYS Maxwell 2D* uses a straight line extrapolation algorithm [22] to extrapolate the B-H curve using the last two data points from the provided curve where as in the in-house FE code, we extrapolate the B-H curve with a slope of μ_0 beyond the last available data point. Thus, the extrapolation of the nominal and perturbed curve is necessary to ensure that the extrapolated B-H curve of *ANSYS Maxwell 2D* matches that of in-house FE code. To this end, we introduce an additional H-value in the deep saturation region, i.e. $H_e = 1.8e5$ A/m, after the last data point of the nominal and perturbed curve. At $H_e = 1.8e5$ A/m, the B-value is given by

$$B_e = (H_e - H_l)\mu_0 + B_l, \tag{2.58}$$

where H_l and B_l correspond to be the last H- and B-values of the B-H data respectively. The value, H_e, is arbitrarily chosen and its choice doesn't affect the study since we assume that after the last data point, $\{H_l, B_l\}$, the slope of the B-H curve is μ_0. Thereafter, we construct a shape-preserving polynomial cubic Hermite interpolating polynomials (PCHIP) function with the B-H data points, given by $B(H)$ and using this function, we sample 50 B-values at 50 equally spaced H-values in the log-scale. The PCHIP is constructed to ensure that the slope of the curve is smooth till the last extrapolated data point which is essential in the iterative solution of the MVP (refer to Section 2.2 for details). The data points of the 2 B-H curves are provided in Tables 2.8 and 2.9 and illustrated in Fig. 2.18.

The torque waveforms corresponding to these B-H curves were obtained from the in-house FE code and *ANSYS Maxwell 2D* separately. They can be observed in Figs. 2.19, 2.20, 2.21, 2.22 and 2.23. We also compute the difference of QoIs corresponding to these B-H curves using the 2 solvers. Fig. 2.24 shows the difference between the average torque computed from the in-house FE code and *ANSYS Maxwell 2D*. The scatter plots reveal that the difference of average torque obtained from the 2 solvers is approximately the same. Small discrepancies can be observed in the values

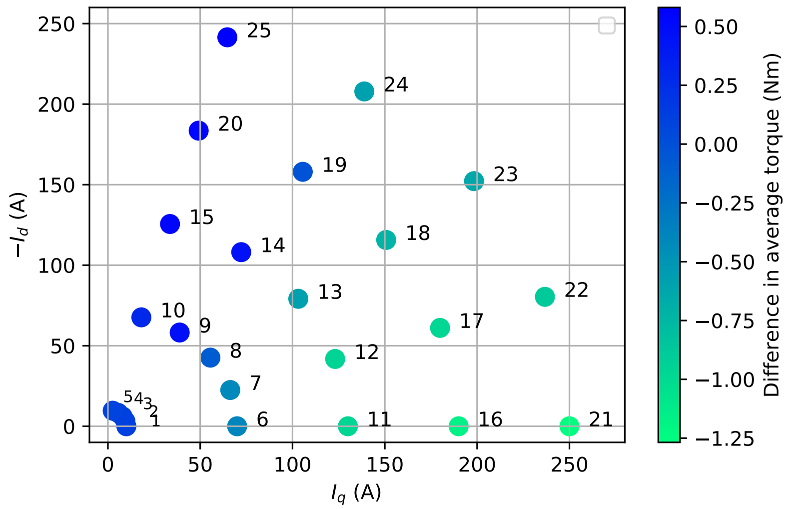

Fig. 2.10.: Difference in the average torque from *ANSYS Maxwell 2D* and in-house FE code in I_q-I_d plane

reported in Table 2.10. These discrepancies are acceptable considering the reasoning (pertaining to the basis functions of MVP and the mesh of the solvers) provided earlier in this section. A similar phenomena is observed for the difference between the sixth and twelfth harmonic components of the torque waveforms at the nominal and perturbed *B-H* curves as illustrated in Figs. 2.25 and 2.26 and their corresponding reported values in Table 2.11 and 2.12. In conclusion, it can be said that the in-house FE code is validated against results from *ANSYS Maxwell 2D*.

Table 2.5.: Difference in the average torque obtained using *ANSYS Maxwell 2D* and in-house FE code

Operating point	**Difference (Nm)**
1	0.1228
2	0.1252
3	0.1229
4	0.1121
5	0.0928
6	-0.3852
7	-0.4144
8	-0.0897
9	0.4714
10	0.2892
11	-0.9699
12	-0.9562
13	-0.5879
14	0.4608
15	0.5422
16	-1.1677
17	-0.9722
18	-0.7306
19	-0.0239
20	0.5434
21	-1.2680
22	-0.8810
23	-0.6385
24	-0.5887
25	0.5807

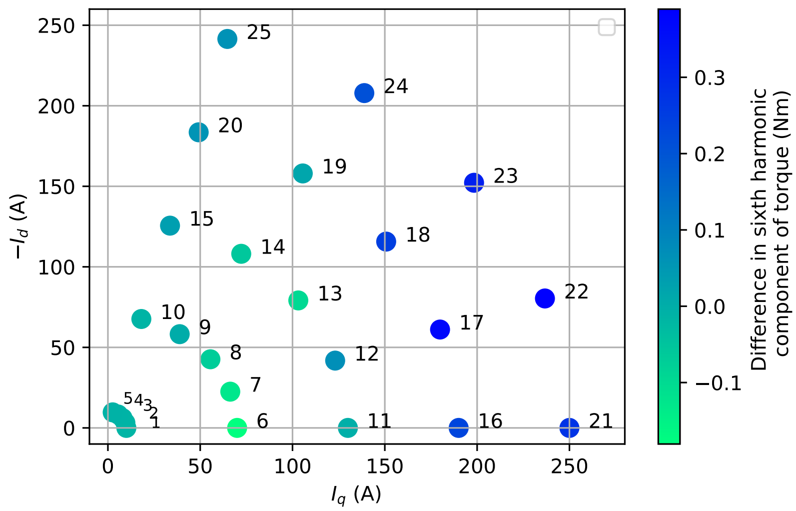

Fig. 2.11.: Difference in sixth harmonic component of torque from *ANSYS Maxwell 2D* and in-house FE code in I_q-I_d plane

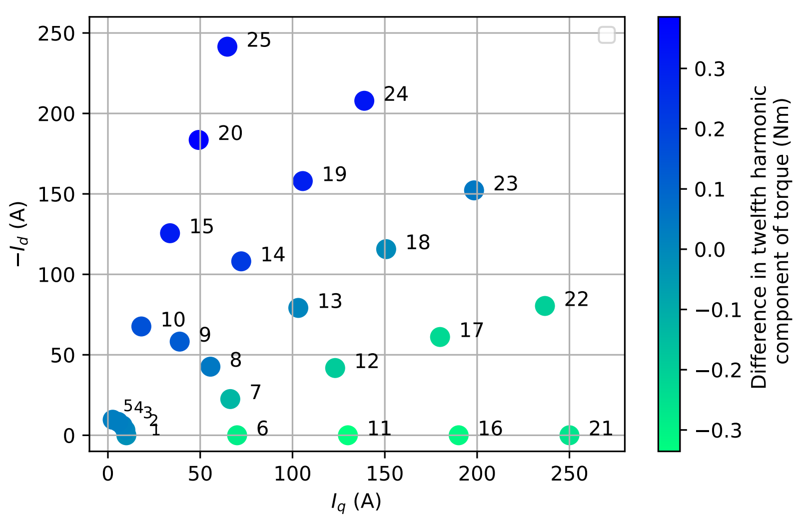

Fig. 2.12.: Difference in twelfth harmonic component of torque *ANSYS Maxwell 2D* and in-house FE code in I_q-I_d plane

Table 2.6.: Difference in the sixth harmonic component of torque obtained using *ANSYS Maxwell 2D* and in-house FE code

Operating point	**Difference (Nm)**
1	−0.0151
2	−0.0144
3	−0.0127
4	−0.0111
5	−0.0079
6	−0.1805
7	−0.1266
8	−0.0684
9	0.0062
10	−0.0131
11	−0.0008
12	0.0689
13	−0.0939
14	−0.0552
15	0.0339
16	0.2344
17	0.3751
18	0.2492
19	0.0197
20	0.0590
21	0.2755
22	0.3893
23	0.3179
24	0.2112
25	0.0641

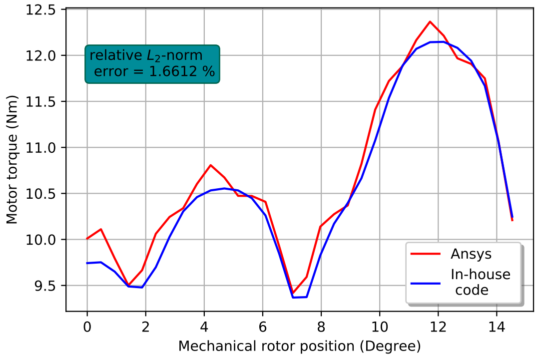

(a)

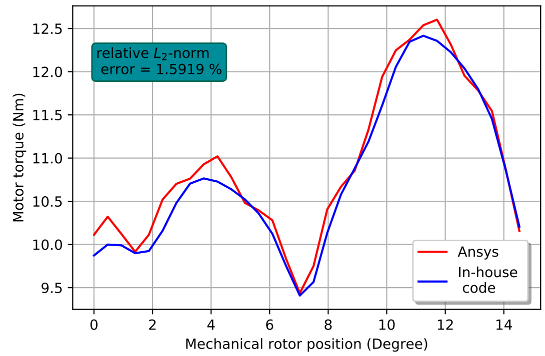

(b)

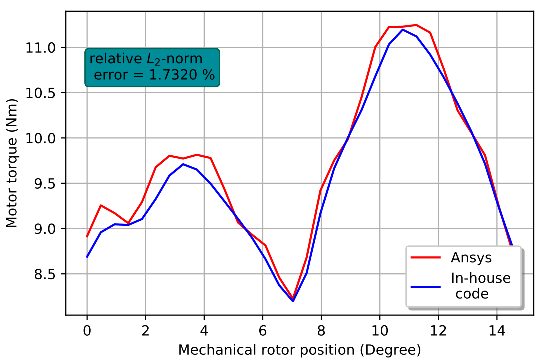

(c)

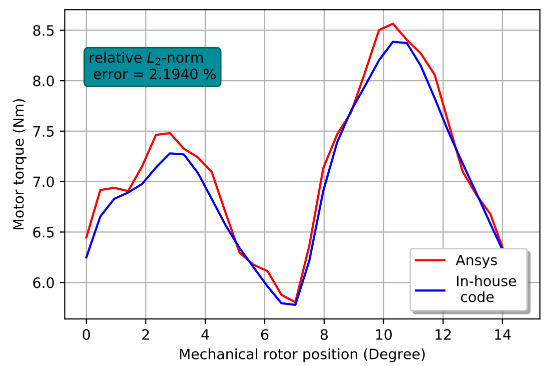

(d)

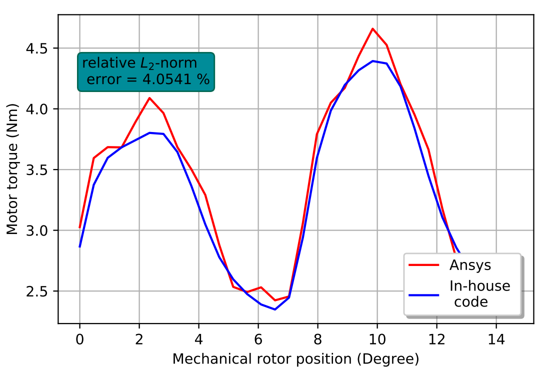

(e)

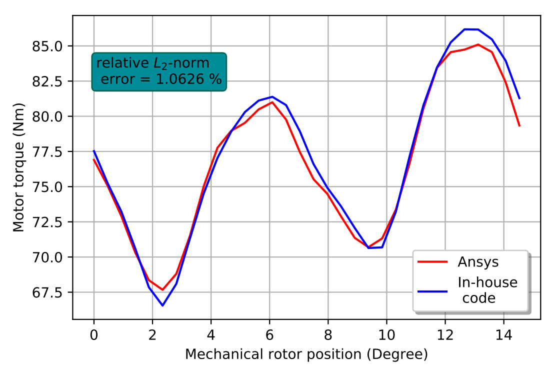

(f)

Fig. 2.13.: Torque waveforms corresponding to operating point (a) 1, (b) 2, (c) 3, (d) 4, (e) 5, (f) 6

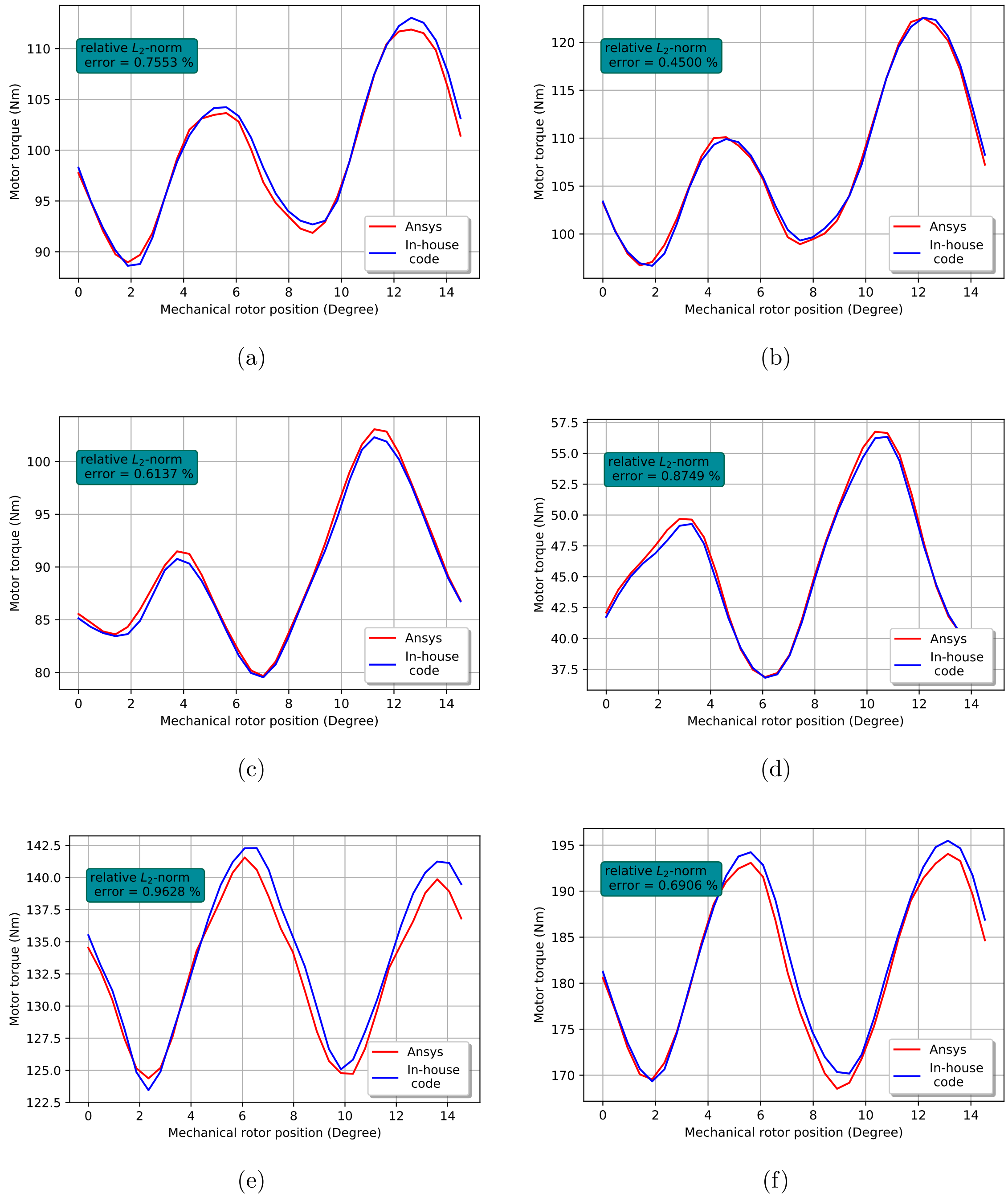

Fig. 2.14.: Torque waveforms corresponding to operating points (a) 7, (b) 8, (c) 9, (d) 10, (e) 11, (f) 12

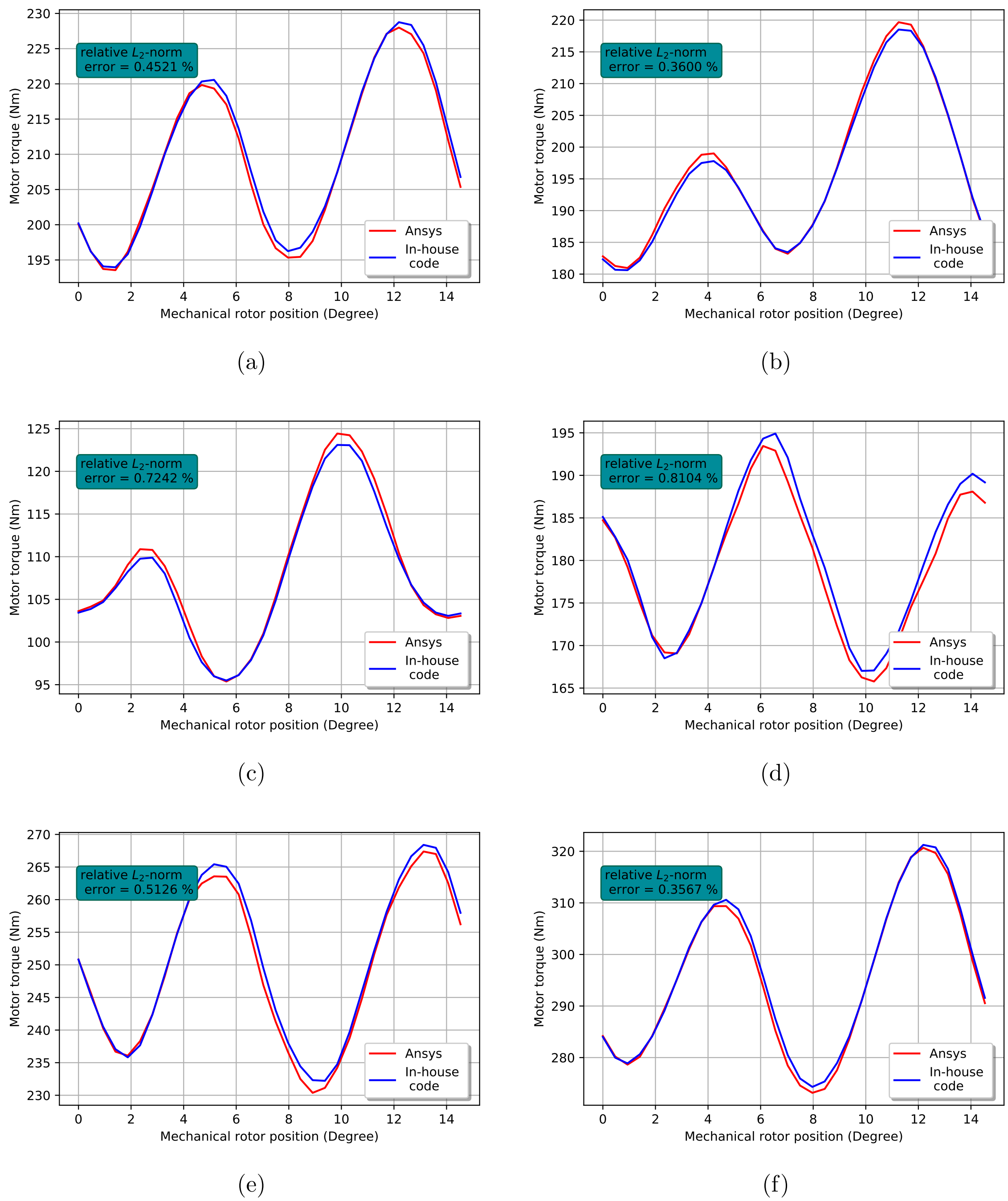

Fig. 2.15.: Torque waveforms corresponding to operating points(a) 13, (b) 14, (c) 15, (d) 16, (e) 17, (f) 18

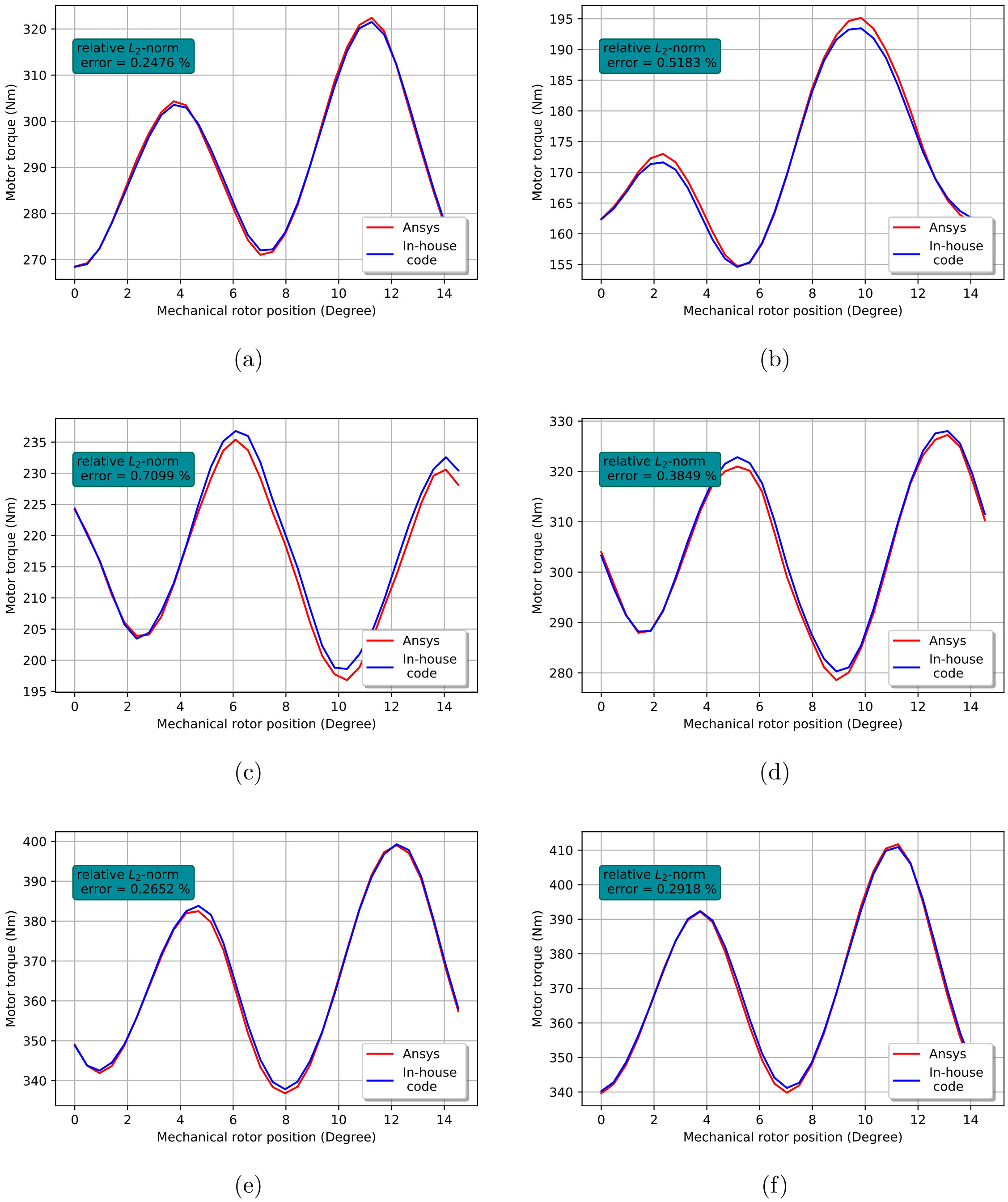

Fig. 2.16.: Torque waveforms corresponding to operating points (a) 19, (b) 20 (c) 21, (d) 22, (e) 23, (f) 24

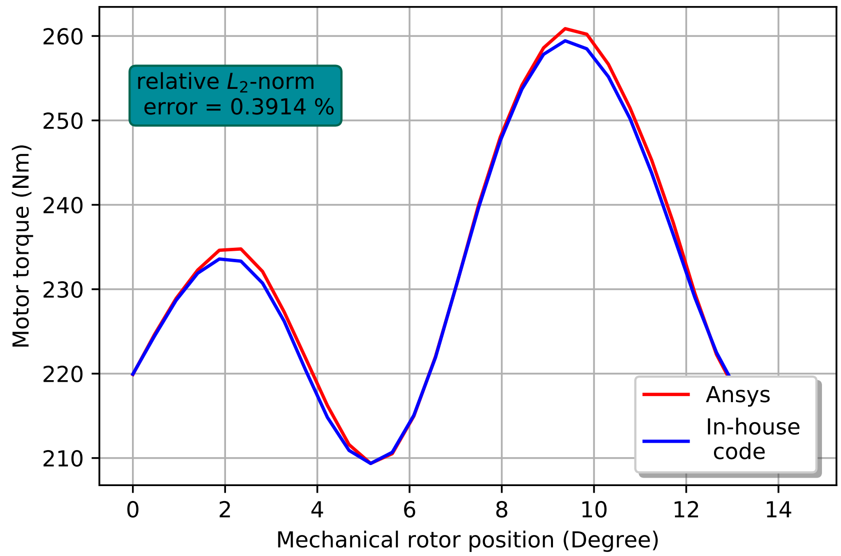

Fig. 2.17.: Torque waveform corresponding to operating point 25

Validation of sensitivity to change in *B*-*H* curve

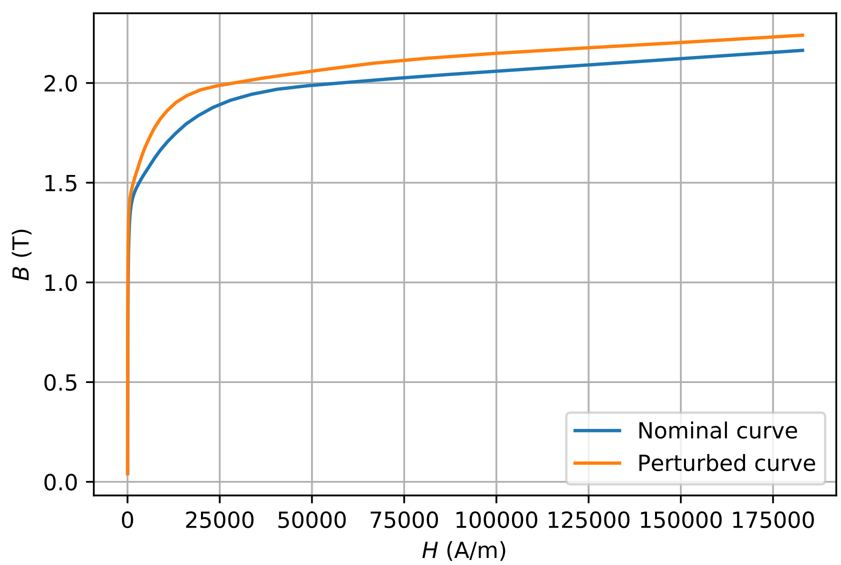

Fig. 2.18.: *B*-*H* curves for comparing the sensitivities of in-house FE code and *ANSYS Maxwell 2D*

Table 2.9.: B-H data points of the perturbed curve

H (A/m)		B (T)	
9.0178	3910.5781	0.0416	1.6364
11.0409	4787.9063	0.0587	1.6792
13.5179	5862.0608	0.0961	1.7227
16.5506	7177.1992	0.1637	1.7707
20.2637	8787.3855	0.2638	1.8176
24.8098	10758.8130	0.3751	1.8617
30.3759	13172.5252	0.4868	1.9031
37.1906	16127.7475	0.5988	1.9371
45.5342	19745.9665	0.7106	1.9655
55.7497	24175.9236	0.8133	1.9852
68.2570	29599.7302	0.9082	2.0025
83.5703	36240.3540	0.9944	2.0233
102.3191	44370.7848	1.0706	2.0449
125.2741	54325.2570	1.1329	2.0700
153.3791	66512.9895	1.1873	2.0989
187.7893	81435.0087	1.2312	2.1245
229.9193	99704.7448	1.2710	2.1486
281.5011	122073.2494	1.3084	2.1737
344.6552	149460.0708	1.3411	2.2024
421.9777	180000	1.3695	2.2399
516.6473		1.3929	
632.5558		1.4136	
774.4681		1.4332	
948.2180		1.4521	
1160.9483		1.4704	
1421.4041		1.4892	
1740.2925		1.5111	
2130.7227		1.5358	
2608.7449		1.5628	
3194.0101		1.5966	

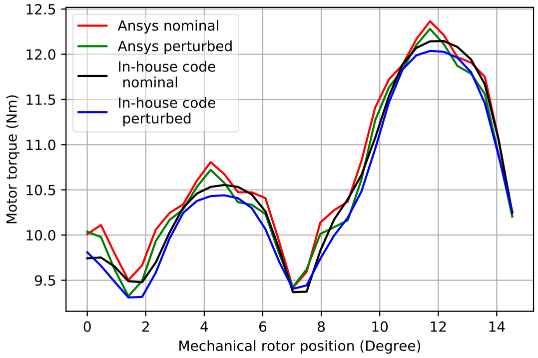

(a)

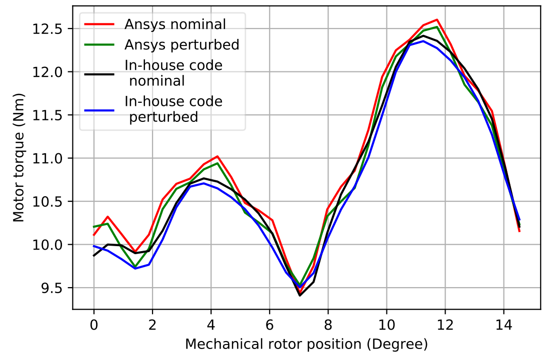

(b)

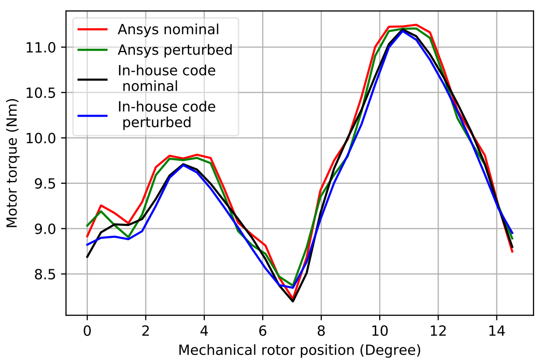

(c)

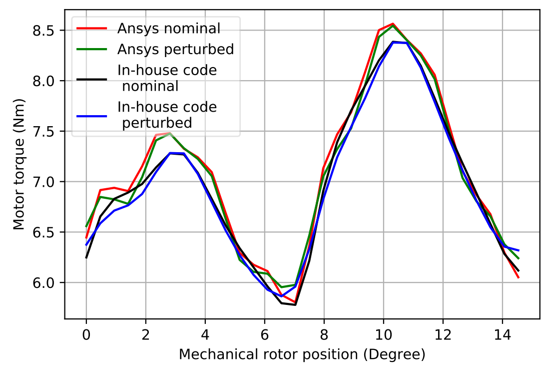

(d)

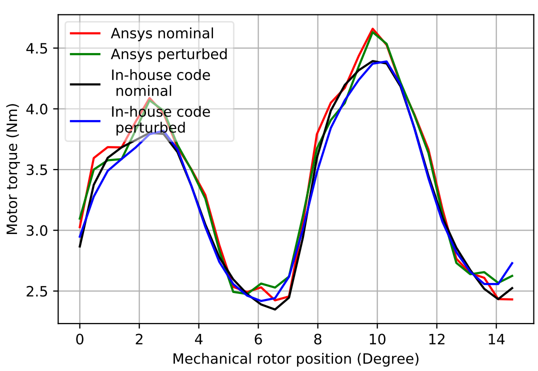

(e)

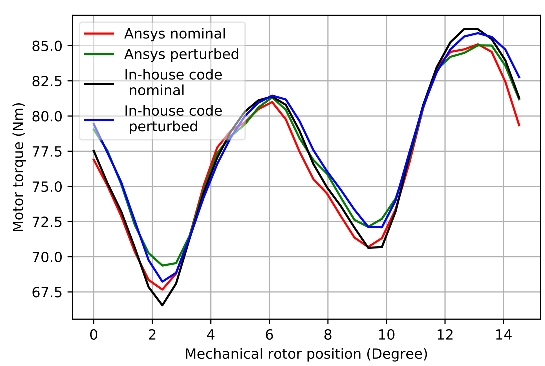

(f)

Fig. 2.19.: Torque waveforms corresponding to operating point (a) 1, (b) 2, (c) 3, (d) 4, (e) 5, (f) 6

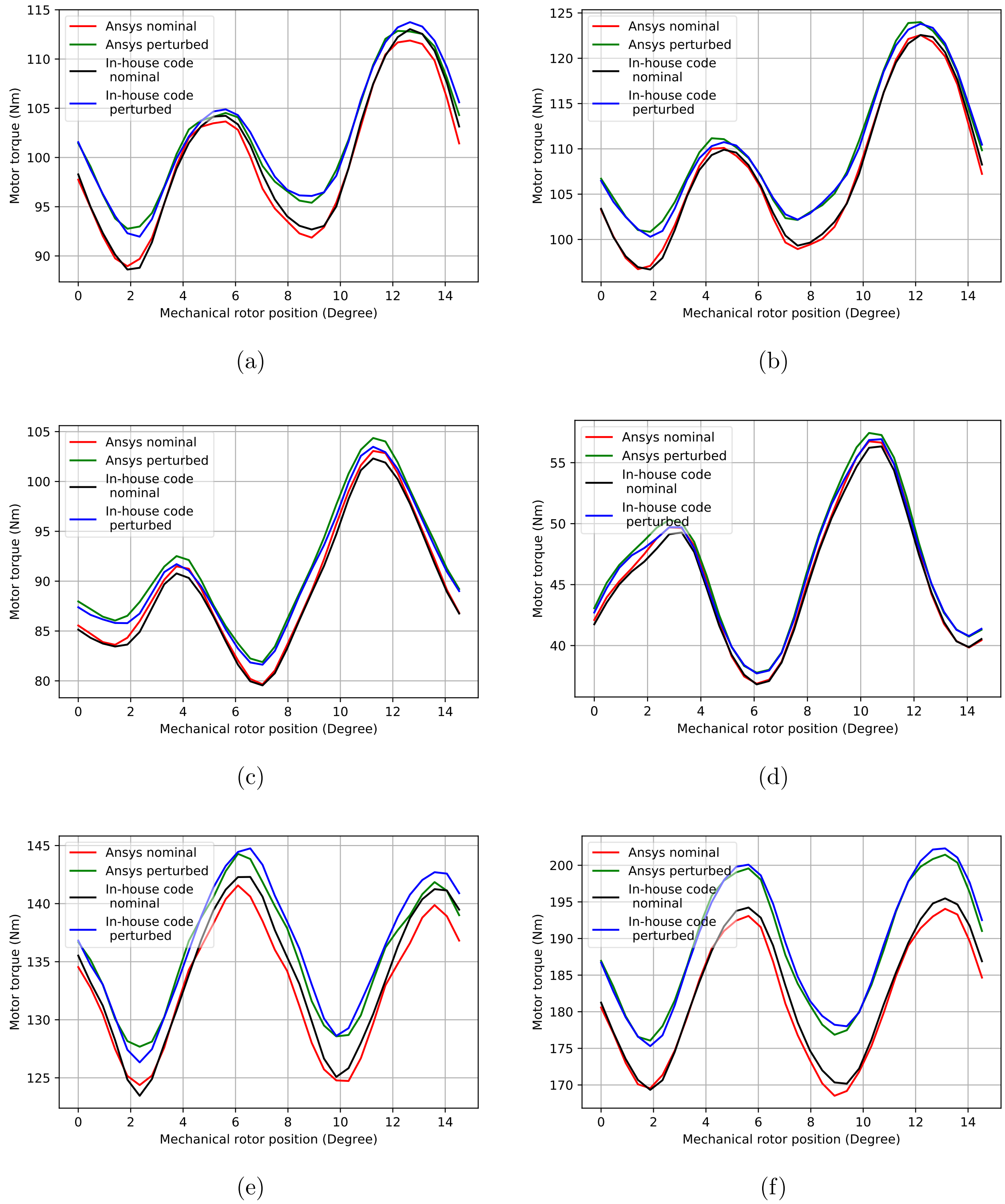

Fig. 2.20.: Torque waveforms corresponding to operating points (a) 7, (b) 8, (c) 9, (d) 10, (e) 11, (f) 12

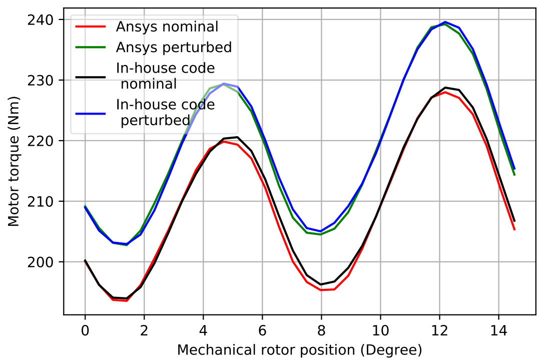

(a)

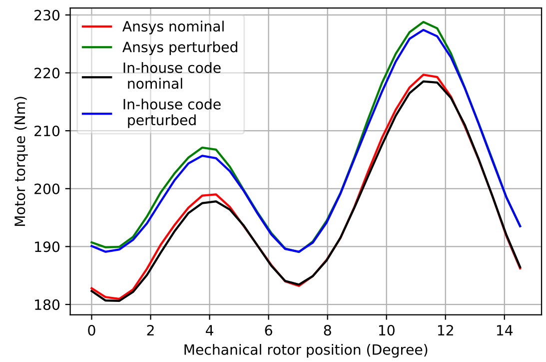

(b)

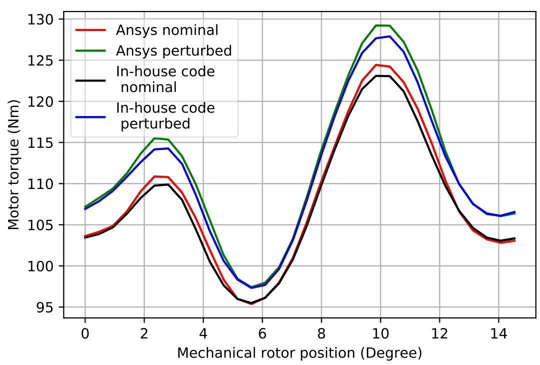

(c)

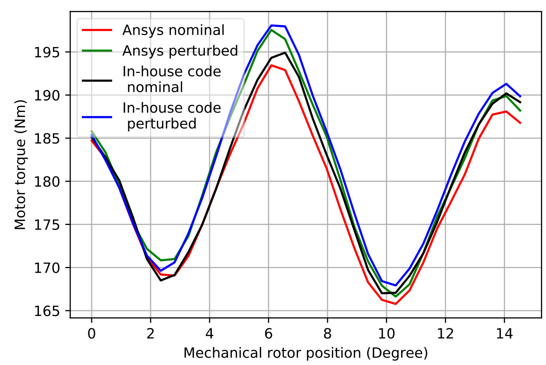

(d)

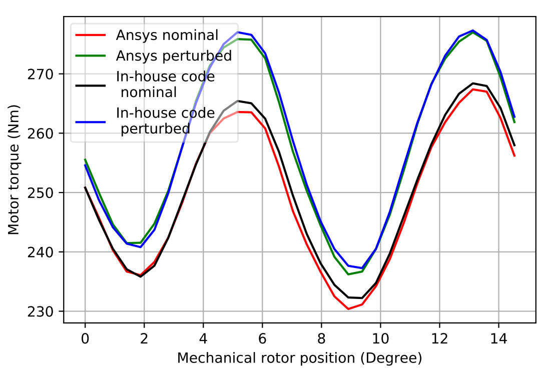

(e)

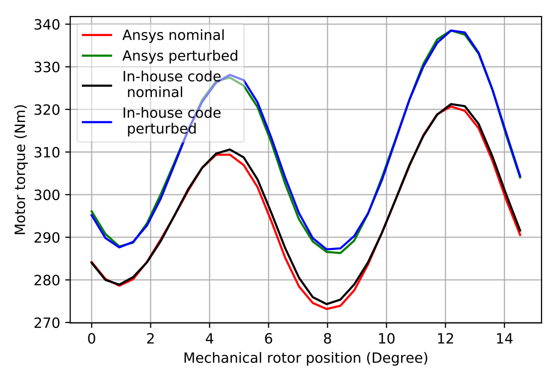

(f)

Fig. 2.21.: Torque waveforms corresponding to operating points(a) 13, (b) 14, (c) 15, (d) 16, (e) 17, (f) 18

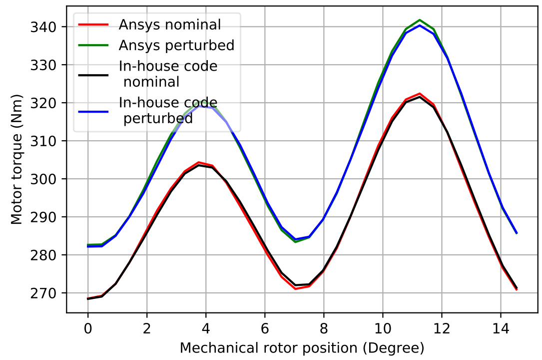

(a)

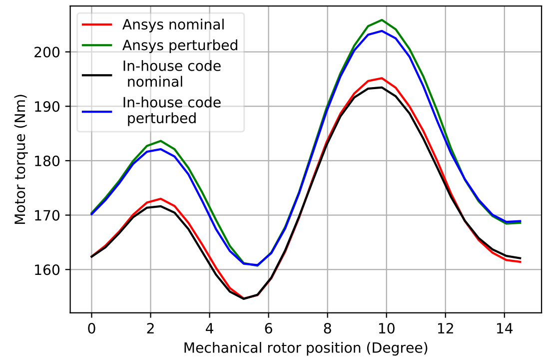

(b)

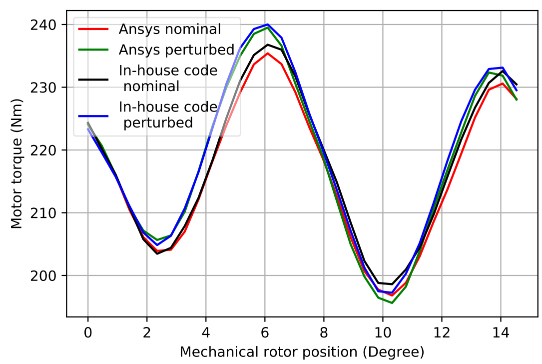

(c)

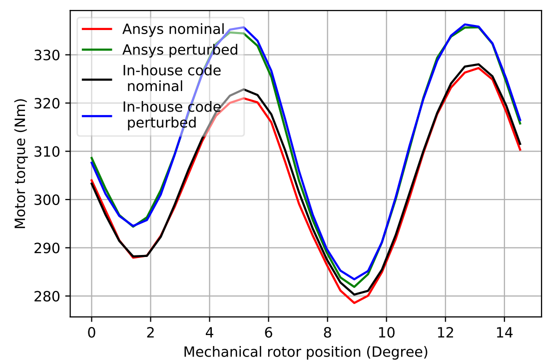

(d)

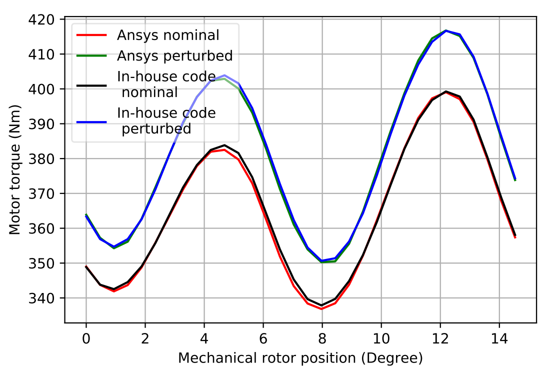

(e)

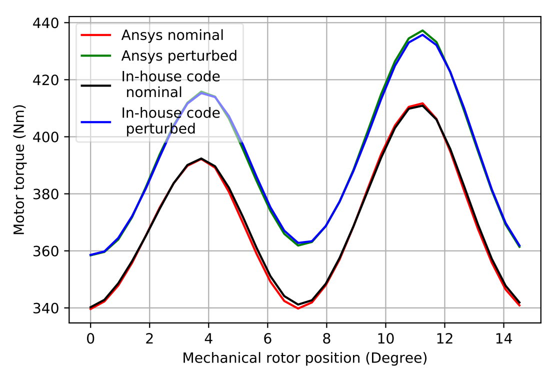

(f)

Fig. 2.22.: Torque waveforms corresponding to operating points (a) 19, (b) 20 (c) 21, (d) 22, (e) 23, (f) 24

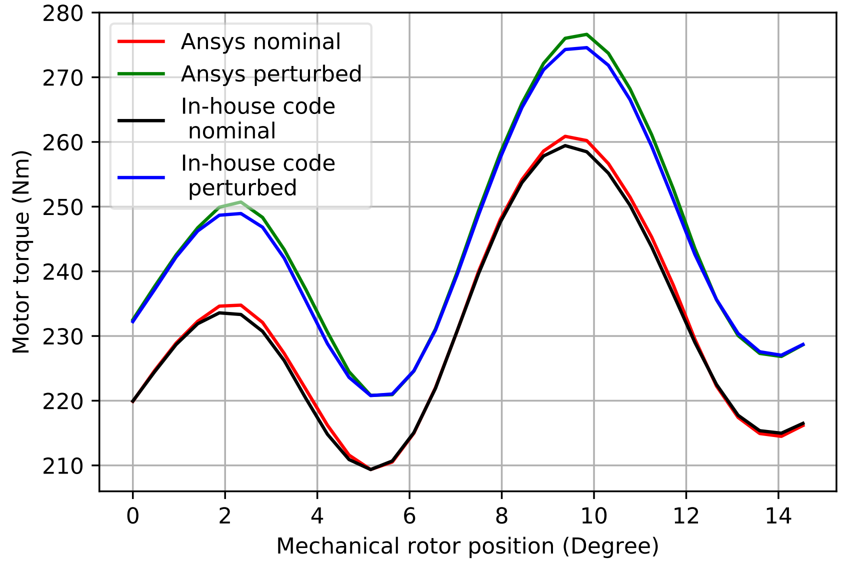

Fig. 2.23.: Torque waveform corresponding to operating point 25

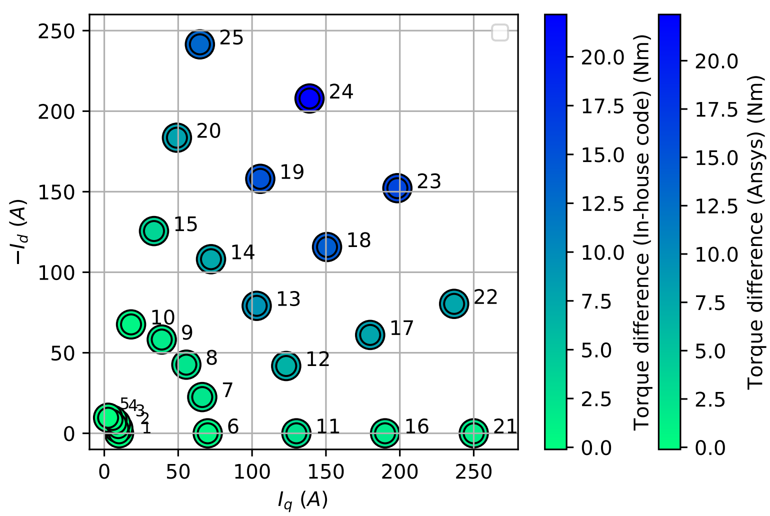

Fig. 2.24.: Difference in the average torque from the in-house FE code and *ANSYS Maxwell 2D* for the nominal and perturbed *B-H* curves

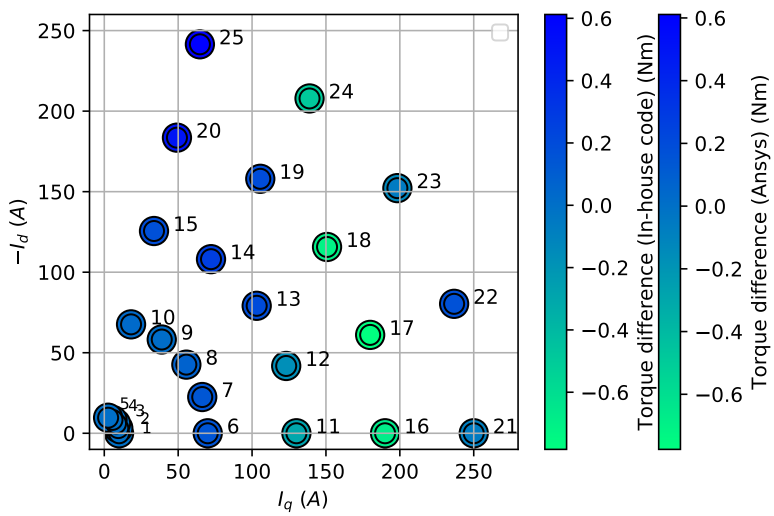

Fig. 2.25.: Difference in the sixth harmonic component of torque from the in-house FE code and *ANSYS Maxwell 2D* for nominal and perturbed *B-H* curves

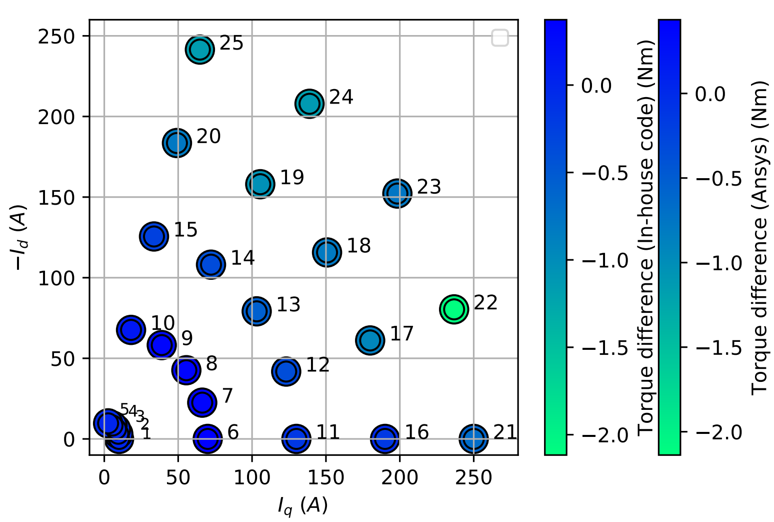

Fig. 2.26.: Difference in the twelfth harmonic component of torque from the in-house FE code and *ANSYS Maxwell 2D* for nominal and perturbed *B-H* curves

Table 2.7.: Difference in the twelfth harmonic component of torque obtained using *ANSYS Maxwell 2D* and in-house FE code

Operating point	**Difference (Nm)**
1	-0.0228
2	0.0030
3	0.0194
4	0.0294
5	0.0306
6	-0.2868
7	-0.1326
8	0.0463
9	0.1284
10	0.1572
11	-0.3355
12	-0.1877
13	0.0088
14	0.2197
15	0.3069
16	-0.3142
17	-0.2274
18	-0.0071
19	0.2958
20	0.3855
21	-0.2592
22	-0.2002
23	0.0448
24	0.3240
25	0.3343

Table 2.8.: *B*-*H* data points of the nominal curve

H (A/m)		B (T)	
26.2817	7455.7184	0.0889	1.6266
31.7260	9000.1696	0.1475	1.6658
38.2980	10864.5537	0.2327	1.7063
46.2314	13115.1448	0.3375	1.7487
55.8082	15831.9456	0.4409	1.7939
67.3689	19111.5313	0.5438	1.8358
81.3244	23070.4828	0.6471	1.8765
98.1707	27849.5307	0.7507	1.9131
118.5068	33618.5579	0.8424	1.9434
143.0554	40582.6384	0.9294	1.9687
172.6893	48989.3273	1.0073	1.9866
208.4619	59137.4609	1.0770	2.0024
251.6448	71387.7793	1.1341	2.0212
303.7730	86175.7497	1.1849	2.0417
366.6995	104027.0465	1.2265	2.0642
442.6613	125576.2374	1.2634	2.0914
534.3585	151589.3408	1.2992	2.1242
645.0508	180000	1.3309	2.1638
778.6730		1.3588	
939.9750		1.3824	
1134.6908		1.4026	
1369.7418		1.4215	
1653.4837		1.4393	
1996.0026		1.4568	
2409.4743		1.4738	
2908.5967		1.4916	
3511.1122		1.5121	
4238.4386		1.5351	
5116.4307		1.5600	
6176.2988		1.5904	

Table 2.10.: Difference in the average torque from in-house FE code and *ANSYS Maxwell 2D* for the nominal and perturbed *B-H* curves

Operating point	**Difference (Nm) (In-house code)**	**Difference (Nm) (*Ansys*)**
1	−0.1095	−0.1069
2	−0.0858	−0.0842
3	−0.0559	−0.0539
4	−0.0279	−0.0256
5	−0.0087	−0.0060
6	0.8089	0.6579
7	2.3365	2.0966
8	2.4744	2.2281
9	1.8028	1.6992
10	0.8332	0.8083
11	2.9282	2.4309
12	7.2609	6.6760
13	9.5509	9.2058
14	7.7270	7.5216
15	3.7278	3.6306
16	2.2545	1.7449
17	8.3806	7.7624
18	14.5674	14.0029
19	15.3174	14.9812
20	8.1948	7.9872
21	1.7610	1.2760
22	8.2175	7.7189
23	16.5483	16.1229
24	22.3896	22.1657
25	13.3731	13.1337

Table 2.11.: Difference in the sixth harmonic component of torque from in-house FE code and *ANSYS Maxwell 2D* for the nominal and perturbed *B-H* curves

Operating point	**Difference (Nm) (In-house code)**	**Difference (Nm) (*Ansys*)**
1	−0.0005	0.0007
2	0.0006	0.0005
3	0.0024	0.0023
4	0.0043	0.0045
5	0.0059	0.0060
6	0.1464	0.1552
7	0.1431	0.1491
8	0.0779	0.0789
9	0.0169	0.0165
10	0.0316	0.0323
11	−0.2990	−0.2767
12	−0.1675	−0.1607
13	0.1988	0.1889
14	0.2692	0.2673
15	0.1757	0.1936
16	−0.6822	−0.6630
17	−0.7834	−0.7757
18	−0.7195	−0.6943
19	0.1960	0.1961
20	0.4989	0.5030
21	−0.0622	−0.0776
22	0.1659	0.1723
23	−0.0595	−0.1294
24	−0.4862	−0.4911
25	0.6123	0.6110

Table 2.12.: Difference in the twelfth harmonic component of torque from in-house FE code and *ANSYS Maxwell 2D* for the nominal and perturbed *B-H* curves

Operating point	**Difference (Nm) (In-house code)**	**Difference (Nm) (*Ansys*)**
1	0.0048	−0.0036
2	0.0097	0.0105
3	0.0145	0.0155
4	0.0151	0.0162
5	0.0090	0.0100
6	0.3737	0.4358
7	0.3255	0.3849
8	0.3412	0.3846
9	0.3181	0.3276
10	0.1490	0.1318
11	−0.1659	−0.0465
12	−0.3839	−0.2938
13	−0.5679	−0.5365
14	−0.3651	−0.3881
15	−0.2571	−0.2356
16	−0.1804	0.0219
17	−0.9327	−0.8285
18	−0.8139	−0.7731
19	−1.0324	−1.0695
20	−0.7989	−0.8047
21	−0.6880	−0.5728
22	−2.1165	−2.1379
23	−0.7811	−0.7772
24	−1.1333	−1.1792
25	−1.1529	−1.1670

3. DIMENSIONALITY REDUCTION

In the first section of this chapter, various dimensionality reduction techniques are reviewed. Thereafter, in Section 3.2, the methodology to reduce the dimensionality of a dataset using principal component analysis is provided. This section illustrates the procedure to project a dataset into a low-dimensional space and its reconstruction into the original high-dimensional space.

3.1 A brief review

Data analysis of a high dimensional dataset has been a difficult problem in the field of statistics and machine learning as it is difficult to visualize and extract variables of interest in a high-dimensional space. Additionally, predictive modeling in a high-dimensional space is computationally expensive and is encountered by the problem of curse of dimensionality. Thus, it is desirable to reduce the dimensionality of the dataset before performing analysis or constructing a predictive model.

Dimensionality reduction can be achieved in two different ways. One of the ways is retaining the most important variables of the dataset and ignoring the rest. The short-coming of this method is that there is no universal technique to distinguish the important variables from the unimportant ones. Additionally, depending on the quantity of interest, the important variables change. The second way is to identify and project the data set into the underlying low-dimensional space by exploiting the correlation between the elements of the high-dimensional dataset. The later technique referred to as the projection technique maintains the original structure of the data set removing the existing redundancy. Thus, it is a popular technique for dimensionality reduction. However, it must be noted that this technique fails to achieve its objective when the correlation between the elements of the high-dimensional dataset is minimal.

Consider a data set, $\mathbf{D}$ with dimensionality M. Projection techniques project $\mathbf{D}$ to a M' ($M \gg M'$) dimensional space while retaining the geometry of the original dataset to the possible extent. Traditional linear projection techniques like Principal component analysis (PCA) and factor analysis are used to project the dataset into a low-dimensional sub-space using linear a projection matrix. In both the methods, the variables in the low-dimensional space are a linear combination of the high-dimensional variables. PCA is the more elegant technique of the two because it is simple to implement.

In the recent decade, a number of non-linear dimensionality reduction techniques have been developed to tackle non-linear datasets with high dimension. [38] performs a comparative study of the newly developed non-linear dimensionality reduction techniques and traditional PCA. It shows that although non-linear techniques have shown promise in identifying complex manifolds in artificial non-linear datasets, they have failed to show appreciable performance while dealing with real world datasets. At the same time, PCA has been successful in dealing with real world datasets for a long time now. Considering the success of PCA and the simplicity in its implementation, PCA has been used for dimensionality reduction in this study.

3.2 Dimensionality reduction using principal component analysis

Principal component analysis (PCA) is a method of projection of a dataset comprising of a large number of correlated elements into a lower dimensional space, resulting in uncorrelated elements such that the variance of the projected data is maximized. Any observation of any variable in a dataset is referred to as an element of the dataset.

In the low-dimensional space, the variables are called Principal components (PCs) and the elements are called PC scores. PCA follows the mapping of the elements in the high dimensional space to the PC scores using a linear transformation matrix, $\boldsymbol{\phi}$. $\boldsymbol{\phi}$ is such that its rows are orthogonal to each other [39] which facilitates the removal of correlation between the PCs in the low-dimensional space. Also, the variance in the low-dimensional space is distributed in such a way that it is concentrated mostly in first few PCs [39]. Hence, keeping these few PCs and ignoring the rest, it is possible to reconstruct the original data set with appreciable accuracy. This phenomena is called dimensionality reduction and has been used extensively in this study. A brief discussion on the methodology of projection and reconstruction using PCA is provided below.

Consider a data set $\mathbf{D} \in \mathbb{R}^{VXN}$ with V variables and N observations. Let the centered matrix, $\mathbf{C}$, be obtained by after subtracting the mean of each row of $\mathbf{D}$ from the element of its corresponding row. The row-wise mean of $\mathbf{D}$ is given by $\boldsymbol{\mu}$.

3.2.1 Projection

The idea behind PCA is to project the variables of high-dimensional space on such basis vectors such that the variance of the projected variables is maximized. Let $\boldsymbol{\phi}_1$ be such a row vector that projects $\mathbf{C}$ into a space such that the variance of $\boldsymbol{\phi}_1\mathbf{C}$ is maximized, where $\boldsymbol{\phi}_1\mathbf{C}$ represents the projected variable or PC. The variance of $\boldsymbol{\phi}_1\mathbf{C}$ is given by,

$$\begin{aligned} var(\boldsymbol{\phi}_1\mathbf{C}) &= \mathbb{E}[\boldsymbol{\phi}_1\mathbf{C}\mathbf{C}^T\boldsymbol{\phi}_1^T] \\ &= \boldsymbol{\phi}_1\mathbb{E}[\mathbf{C}\mathbf{C}^T]\boldsymbol{\phi}_1^T \\ &= \boldsymbol{\phi}_1\mathbf{Q}\boldsymbol{\phi}_1^T \end{aligned} \tag{3.1}$$

where $\mathbf{Q}$ is the covariance of $\mathbf{C}$. The maximization of Eq. (3.4) needs to be done to obtain $\boldsymbol{\phi}_1$. However, the maximization would not be finite for unconstrained $\boldsymbol{\phi}_1$. Thus, a normalization constraint must be used to overcome this issue. By the geometric definition of PCA, $\boldsymbol{\phi}_1$ corresponds to a basis axis in low-dimensional space. Therefore, it is assumed that $\boldsymbol{\phi}_1$ is a unit vector, as a result, satisfying the constraint $\boldsymbol{\phi}_1\boldsymbol{\phi}_1^T = 1$. It should be noted that this normalization constraint is applied by the definition of PCA. Other kind of constraint leads to more difficult optimization problem and the resultant projected variables are not PCs.

To maximize $\boldsymbol{\phi}_1 \mathbf{Q} \boldsymbol{\phi}_1^T$ subjected to $\boldsymbol{\phi}_1 \boldsymbol{\phi}_1^T = 1$, we use a Lagrange multiplier technique to formulate the objective function. The equation to be maximized is given by

$$\boldsymbol{\phi}_1 \mathbf{Q} \boldsymbol{\phi}_1^T - \lambda_1 (\boldsymbol{\phi}_1 \boldsymbol{\phi}_1^T - 1) \tag{3.2}$$

where λ_1 is the Lagrange multiplier. Differentiating Eq. (3.2) with respect to $\boldsymbol{\phi}_1$, we get

$$\mathbf{Q} \boldsymbol{\phi}_1^T = \lambda_1 \boldsymbol{\phi}_1^T \tag{3.3}$$

Eq. (3.3) represents an eigen value problem where λ_1 is the eigen value of $\mathbf{Q}$ and $\boldsymbol{\phi}_1^T$ is its corresponding eigen vector. From Eqs. (3.1) and (3.3), we get

$$\mathrm{var}(\boldsymbol{\phi}_1 \mathbf{C}) = \boldsymbol{\phi}_1 \mathbf{Q} \boldsymbol{\phi}_1^T = \lambda_1. \tag{3.4}$$

λ_1 has to be the largest eigen value of $\mathbf{Q}$ to maximize Eq. (3.4). Since, $\mathbf{Q}$, the covariance matrix, is positive semi-definite or positive-definite, λ_1 is unique. Similarly, the second basis vector $\boldsymbol{\phi}_2$ is obtained by constrained maximization of $\boldsymbol{\phi}_2 \mathbf{Q} \boldsymbol{\phi}_2^T$ by enforcing an additional constraint of orthogonality between the two basis vectors. This constraint is given by

$$\boldsymbol{\phi}_2 \boldsymbol{\phi}_1^T = 0. \tag{3.5}$$

The equation to be maximized is formulated as

$$\boldsymbol{\phi}_2 \mathbf{Q} \boldsymbol{\phi}_2^T - \lambda_2 (\boldsymbol{\phi}_2 \boldsymbol{\phi}_2^T - 1) - \sigma \boldsymbol{\phi}_2 \boldsymbol{\phi}_1^T. \tag{3.6}$$

Differentiating Eq. (3.6) with respect to $\boldsymbol{\phi}_2$, we get

$$\mathbf{Q} \boldsymbol{\phi}_2^T - \lambda_2 \boldsymbol{\phi}_2^T - \sigma \boldsymbol{\phi}_1^T = 0. \tag{3.7}$$

Premultiplying Eq. (3.7) with $\boldsymbol{\phi}_1$, we obtain

$$\boldsymbol{\phi}_1 \mathbf{Q} \boldsymbol{\phi}_2^T - \boldsymbol{\phi}_1 \lambda_2 \boldsymbol{\phi}_2^T - \boldsymbol{\phi}_1 \sigma \boldsymbol{\phi}_1^T = 0. \tag{3.8}$$

Since the first and second terms on the left hand-side are zero, using Eq. (3.5), we get

$$\sigma = 0. \tag{3.9}$$

Substituting Eq. (3.9) in Eq. (3.8) a similar eigen value problem is reached which is given by

$$\mathbf{Q}\boldsymbol{\phi}_2^T = \lambda_2 \boldsymbol{\phi}_2^T. \tag{3.10}$$

Here λ_2 corresponds to the second largest eigen value of $\mathbf{Q}$. By induction, it can be shown that the the variance of following PCs and their respective PC bases correspond to the remaining eigen values and their corresponding eigen vectors. Thus, the linear transformation matrix $\boldsymbol{\phi}$ corresponds to the transpose of the matrix containing the eigen vectors of $\mathbf{Q}$.

Considering there exists an intrinsic low-dimensional space, most of the variance of the original dataset is concentrated on the first few PCs. Thus, the dimensionality can be reduced by keeping these few PCs which capture the amount of variance that meets an intended criteria, for instance to retain 98% of variance of the total data. In general, more is the retained variance through the PCs, less is the projection error [39].

3.2.2 Reconstruction

Let the retained PC bases be $\boldsymbol{\phi}' \in \mathbb{R}^{V'XV}$ with the corresponding PC scores, $\mathbf{Z}'$ $\in \mathbb{R}^{V'XN}$. The reconstruction of each column of the reduced order matrix, $\mathbf{D}'$, in the high dimensional space is given by

$$\mathbf{D}'^{(i)} = \boldsymbol{\mu} + \sum_{k=1}^{V'} \sqrt{\lambda_k} z_k^{(i)} \boldsymbol{\phi}_k. \tag{3.11}$$

where $z_k^{(i)}$ is the scaled projection of $\mathbf{D}^{(i)} - \boldsymbol{\mu}$ on the eigen vector $\boldsymbol{\phi}_k$.

Dimensionality reduction is a crucial part of this study. We have implemented PCA's capacity of dimensionality reduction in two different applications. Firstly, to construct a reduced order stochastic model of *B*-*H* curves. Here, the reduced variables in the low-dimensional space are used as random variables to sample points which are subsequently used to obtain *B*-*H* curves in the high-dimensional space. Secondly, PCA is used to reduce the output dimensionality of the torque profile so that few variables have to be learned by the surrogate. Furthermore, by just predicting these few variables, torque can be predicted by the surrogate with appreciable accuracy.

4. MODELING OF UNCERTAINTY IN B-H CURVES AND REMANENT FLUX DENSITY OF PERMANENT MAGNETS

The first section of this chapter describes in detail the methodology used to build a reduced-order stochastic model of a dataset of B-H curves that quantifies its uncertainty due to punching. Principal component analysis (PCA) is used to accomplish this objective. In the subsequent section, a modeling technique is proposed to incorporate the uncertainty in B-H curves due to the unknown state of the material composition of steel. In the third section, we model the epistemic uncertainty due to unavailability of accurate B-H data in deep saturation region. The final section of this chapter discusses extended work where we model the uncertainty in the remanent flux density of the permanent magnets of the permanent magnet synchronous machine (PMSM).

4.1 Data-driven modeling of uncertainty due to punching in *B*-*H* curves

In this section, we propose a data-driven approach to model the effect of punching uncertainty on B-H curves. The data collection procedure plays a consequential role in ensuring the accuracy of the proposed model. For appreciable accuracy, each B-H curve must reflect a unique state of the punching tool. The idea is to collect samples such that the distribution of the B-H curves in the dataset reflects the distribution of the underlying uncertainty in the state of the punching tool. Thus, the curves must be obtained by measuring steel samples cut by such punching tools that represent unique states with respect to each other.

Consider a dataset of N B-H curve samples collected by employing the above procedure. Let the dataset be given by $\mathcal{D} = \left\{ \left(\mathbf{b}^{(i)}, \mathbf{h}^{(i)} \right) \right\}_{i=1}^{N}$ where each curve consists of V data points. The B-values are fixed for all samples, i.e., $\mathbf{b}^{(i)} = \mathbf{b}$. Our goal is to construct a reduced-order stochastic model of the processes that generated the B-H curves in $\mathcal{D}$.

We start by populating a $V \times N$ matrix $\mathbf{H} = \left(\mathbf{h}^{(1)}, \dots, \mathbf{h}^{(N)}\right)$ using these samples. The columns of $\mathbf{H}$ are correlated, so we expect $\mathbf{H}$ to be well-described by a low-dimensional manifold embedded in a V-dimensional space [40]. Principal component analysis (PCA) finds the best, in the sense of minimizing the squared reconstruction error, affine linear approximation of this low-dimensional manifold [41].

PCA is based on decomposition of the symmetric, positive-definite covariance matrix given by

$$\mathbf{C}_h = \frac{1}{N-1} \sum_{i=1}^{N} \left(\mathbf{h}^{(i)} - \boldsymbol{\mu}_h\right) \left(\mathbf{h}^{(i)} - \boldsymbol{\mu}_h\right)^T , \tag{4.1}$$

where $\boldsymbol{\mu}_h \in \mathbb{R}^V$ is the row-wise mean of $\mathbf{H}$. Each sample $\mathbf{h}^{(i)}$ can be expressed as

$$\mathbf{h}^{(i)} = \boldsymbol{\mu}_h + \sum_{k=1}^{V} \sqrt{\lambda_{h,k}}\, z_{h,k}^{(i)}\, \boldsymbol{\phi}_{h,k} , \tag{4.2}$$

where $\lambda_{h,k}$ is the k-th largest eigenvalue of $\mathbf{C}_h$, and $\boldsymbol{\phi}_{h,k}$, the corresponding eigenvector. The scalar $z_{h,k}^{(i)}$ is known as the i-th principal component (PC) score of the k-th PC, $\mathbf{z}_{h,k} = \left(z_{h,k}^{(1)}, \dots, z_{h,k}^{(N)}\right)$. The eigenvalue, $\lambda_{h,k}$, also represents the amount of variance of the original dataset captured by the k-th PC. Dimensionality reduction is achieved by keeping the first few PCs that capture sufficient variance and ignoring the rest [41]. These few PCs form the foundation of our reduced order stochastic model.

We demonstrate our methodology using a synthetic dataset. As shown in [10], the B-H curve is most affected near the "knee-point" due to punching, extent of which depends on the state of punching tool. Sharp, high-speed punch with low cutting clearance causes the least degradation of the B-H curve where as a blunt, low-speed punch with high-clearance causes the most degradation. Thus, we design a function that incorporates such degradation. We call it the *degradation function.* The synthetic dataset of degraded curves is generated by perturbing the H-values of a nominal B-H curve, $\{\mathbf{h}_n, \mathbf{b}_n\}$ using the *degradation function*. This function is inspired by the probability density function of a log-normal distribution and is given by,

$$d(h_{\text{dg}}, B) = \frac{h_{\text{dg}}}{(B_{\max} - B + \epsilon_m)\rho_{\text{dg}}\sqrt{2\pi}} \exp\left(-\frac{(\ln(B_{\max} - B + \epsilon_m) - \mu_{\text{dg}})^2}{2\rho_{\text{dg}}^2}\right) + \epsilon_B. \tag{4.3}$$

where $\epsilon_B = 0.04$, $\epsilon_m = 1e-7$, $\rho_{\text{dg}} = 0.8$, $\mu_{\text{dg}} = 0$. $B_{\max}$ corresponds to the maximum B-value in the dataset of the nominal B-H curve. h_{dg} is a sample from $\mathbf{H}_{\text{dg}}$, where $\mathbf{H}_{\text{dg}}$ is given by

$$\mathbf{H}_{\text{dg}} \sim \mathcal{U}(0.3, 3) \tag{4.4}$$

The degradation function can be visualized in Fig. 4.1 for $h_{\text{dg}} = 1$. To confer with the used practice of B-H curve plotting, the y-axis corresponds to the independent variable, B, in this case. The constants in the functions are manually calibrated for the data available to the author. However, the behavior of the function itself is independent of the dataset. Thus, depending on the availability of the data to any other user, the function can be calibrated to obtain the synthetic dataset.

The procedure to generate a degraded curve is as follows. First, we obtain a sample from $\mathbf{H}_{\text{dg}}$ (Eq. (4.4)), h_{dg}. Second, at $\mathbf{b}_n$, we substitute h_{dg} in Eq. (4.3) to obtain a vector, $\mathbf{d}(h_{\text{dg}}, \mathbf{b}_n)$. Third, the degraded curve, $\mathbf{h}_g$, is obtained by plugging $\mathbf{d}(h_{\text{dg}}, \mathbf{b}_n)$ in the formula,

$$\mathbf{h}_g = \mathbf{h}_n + \mathbf{d}(h_{\text{dg}}, \mathbf{b}_n)\dot{\mathbf{h}}_n. \tag{4.5}$$

In this study we use the nominal B-H curve corresponding to *36F155* (*M-19*) where the number of data points, $V = 41$. By sampling $N = 50$ values from $\mathbf{H}_{\text{dg}}$ and following the procedure stated earlier, we obtain 50 synthetic curves as shown in Fig. 4.2. Depending on the uncertain state of the punching tool, the B-H curves in Fig. 4.2 exhibit different characteristics. The values corresponding to these B-H curves can be found in the Appendix A.

We assemble the H-values corresponding to these 50 samples to form $\mathbf{H} \in \mathbb{R}^{41\times50}$. Thereafter, we perform PCA of $\mathbf{H}$. The variance represented by the first three PCs

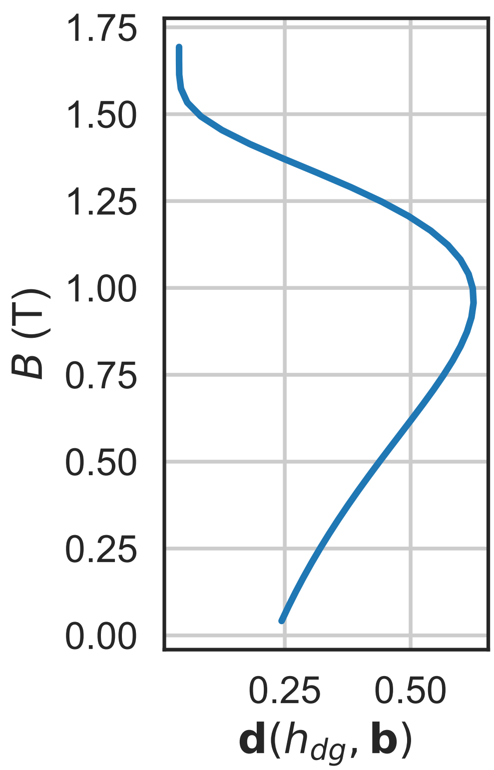

Fig. 4.1.: Illustration of the *degradation function* for $h_{\mathrm{dg}} = 1$

can be observed in Fig. 4.3, and their corresponding eigenvectors can be observed in Fig. 4.4. In our case, the first PC, $\mathbf{z}_{h,1}$, captures more than 99.9% of the variance from the original dataset (see Fig. 4.3). Thus, we retain the first PC and ignore the rest. In an experimental dataset, it is likely that two or more PCs may be necessary.

The PC scores, $z_{h,1}^{(i)}$'s, can be interpreted as samples from a distribution $\mathbf{Z}_h$. Thus, B-H curves reflecting punching uncertainty can be reconstructed by drawing samples from $\mathbf{Z}_h$, and mapping them to the high-dimensional space. Here one must say, how can we sample from $\mathbf{Z}_h$ if the distribution of $\mathbf{Z}_h$ is unknown. We use kernel density estimation with Gaussian kernels to estimate the density of $\mathbf{Z}_h$ (see Fig. 4.5). Thus, our model for the B-H curve for any sample, z_h from $\mathbf{Z}_h$, is:

$$\mathbf{h}_r(z_h) = \boldsymbol{\mu}_h + \sqrt{\lambda_{h,1}} z_h \boldsymbol{\phi}_{h,1}. \tag{4.6}$$

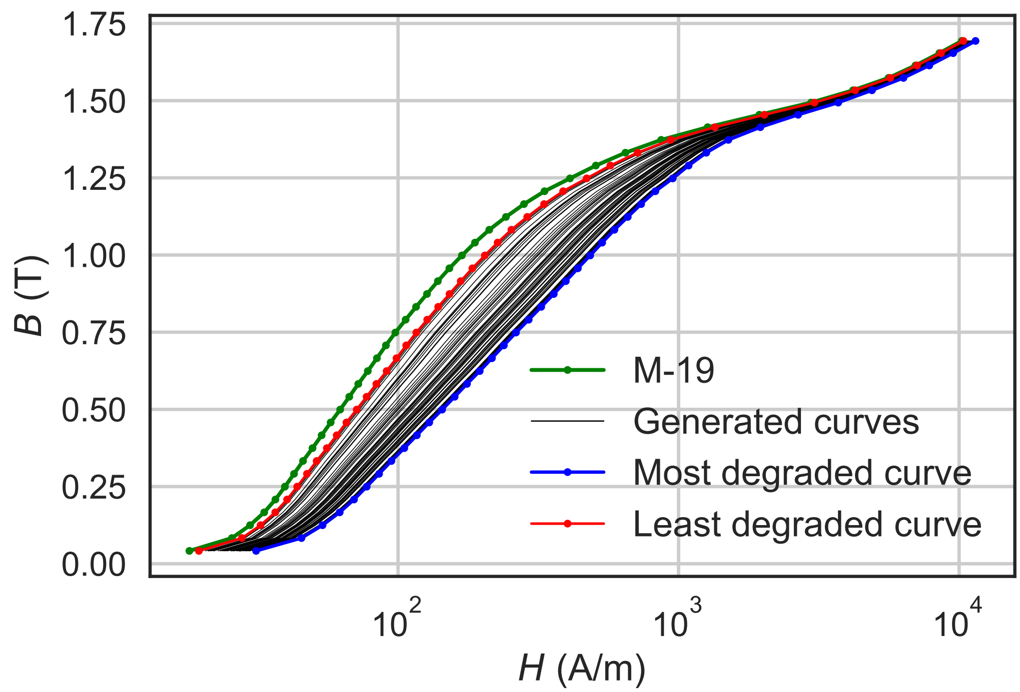

Fig. 4.2.: Synthetically generated B-H curves.

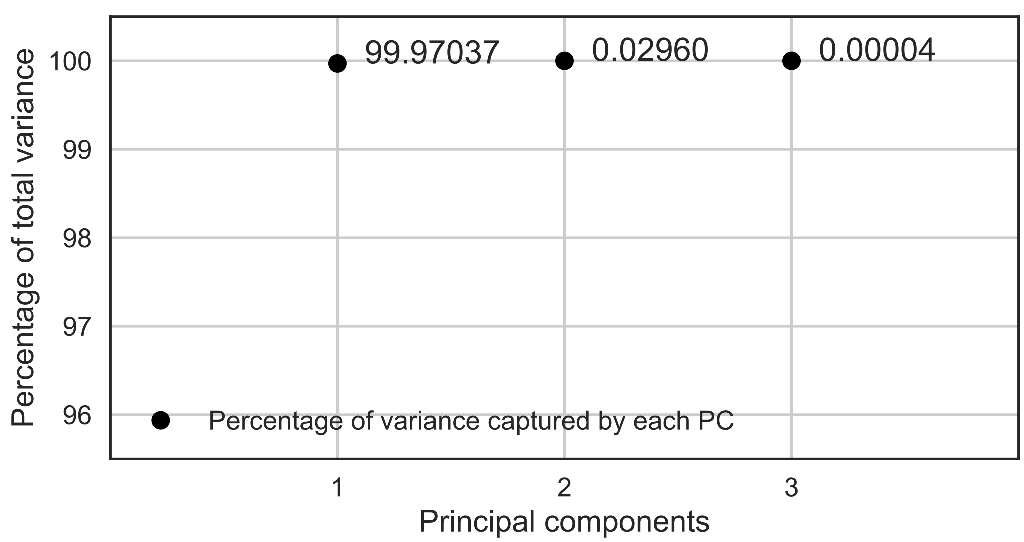

Fig. 4.3.: Percentage of total variance captured by PCs for the reduced-order stochastic model.

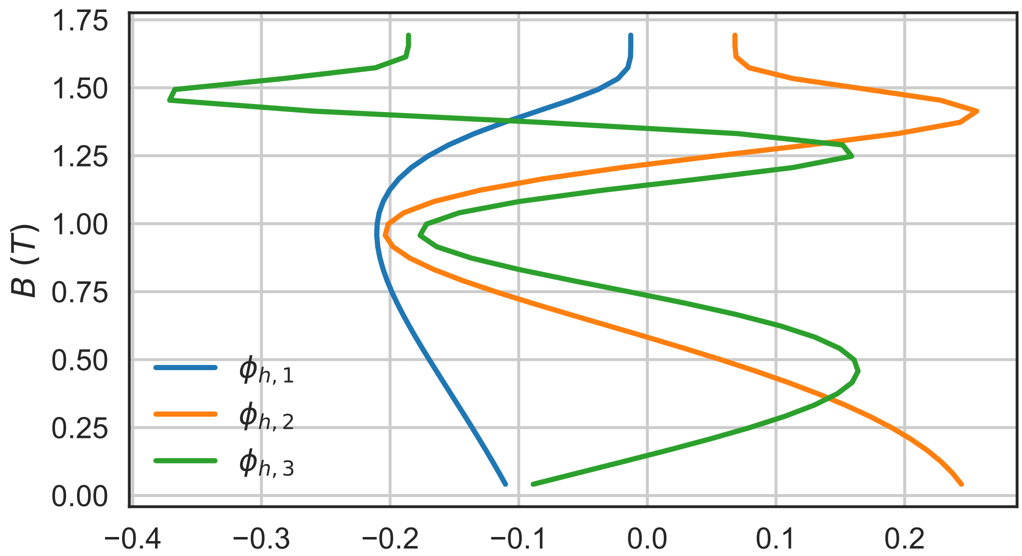

Fig. 4.4.: Eigenvectors of the covariance matrix of $\mathbf{H}$.

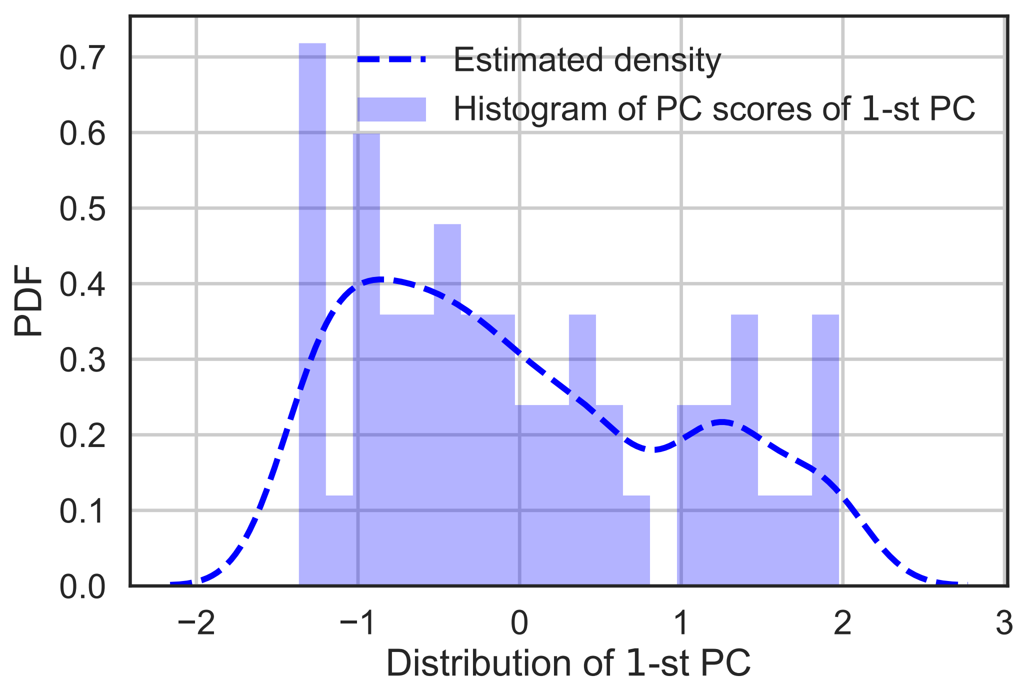

Fig. 4.5.: Density estimation of 1-st PC

Table 4.1.: Random variables defining uncertainty in the state of the punching tool of different degraded zones

Variable	**Degraded zone**
$\mathbf{Z}_{\text{hst}}$	Stator teeth and slots
$\mathbf{Z}_{\text{hso}}$	Outer edge of the stator
$\mathbf{Z}_{\text{hro}}$	Outer edge of the rotor
$\mathbf{Z}_{\text{hri}}$	Inner edge of the rotor
$\mathbf{Z}_{\text{hrm}}$	Rotor magnet pockets

We now come to the problem of defining the uncertain state of the 5 punching tools described in Section 2.2. The states of these tools are defined by five different variables listed in Table 4.1. Since we have established that $\mathbf{Z}_h$ represents the uncertain state of a punching tool, these variables follow the characteristic of $\mathbf{Z}_h$. Here, it is imperative to state that these variables are independent of each other. Thus, although the B-H curve uncertainty reflected by their corresponding reconstructed samples would be similar, the individual samples would not be the same.

4.2 Modeling of uncertainty in *B-H* curves due to unknown material composition

The uncertainty in the B-H curve characteristics of steel due to the unknown state of its material composition (material uncertainty) is reflected through a model in this section. This uncertainty is expected to be small since the material composition of a commercially manufactured non-oriented silicon steel is tightly regulated [3]. Our approach for modeling the material uncertainty is as follows. First, we obtain the data of the nominal B-H curve, $\{\mathbf{h}_n, \mathbf{b}_n\}$, corresponding to the steel lamination which has not undergone the process of punching. The nominal data, in our study, corresponds to the B-H curve of *36F155* (*M-19*). We model material uncertainty considering a uniform distribution about the B-values of the nominal curve such that the maximum deviation about these B-values is defined as a function of $\mathbf{h}_n$, given by

$$\mathbf{b}_{\mathrm{dv}} = \frac{1}{\sqrt{\mathbf{h}_n}} + b_o \mathbf{i}_n \tag{4.7}$$

where $b_o = 0.01$ T and $\mathbf{i}_n \in \mathbb{R}^{N\times 1}$ is a vector whose each element is equal to unity. The first term on the right hand side represents an element-wise operation. The offset b_o is used to account for the fact that the uncertainty at high flux region is not negligible [3]. Second, we define a uniform random variable, $\mathbf{U}$, where $\mathbf{U}$ is given by

$$\mathbf{U} \sim \mathcal{U}(-1, 1). \tag{4.8}$$

Third, for any sample, u, drawn from $\mathbf{U}$, the B-H curve representing material uncertainty is given by

$$\mathbf{b}_m(u) = \mathbf{b}_n + u\mathbf{b}_{\mathrm{dv}}. \tag{4.9}$$

As each curve obtained using Eq. (4.9) has equal probability of reflecting the actual B-H characteristics of the material, uniform distribution can satisfactorily model the effect of material uncertainty in B-H curves. Thus, our model reflects the unknown state of the material composition and its effect on the B-H characteristics. Fig. 4.9 shows 20 curves reflecting material uncertainty.

4.3 Modeling of the epistemic uncertainty in the saturation value of magnetic flux density

In this section, we model the uncertainty associated with B-H curves in deep saturation region. For the purpose of modeling, instead of working with B-H curves we work with M-H curves, where M is given by

$$M = B - \mu_0 H. \tag{4.10}$$

The slope of the M-H curves in deep saturation region is close to zero. This property is used later in this section.

We incorporate the uncertainty in saturation flux density on all the *B*-*H* curves reflecting punching and material uncertainty. To do so, for each *B*-*H* curve, we obtain the corresponding *M*-*H* curve using Eq. (4.10). We assume that the curve saturates at $H_{\text{sat}} = 1e5$ A/m because the corresponding *M*-value, M_{sat}, for *36F155* (*M19*) is within 1% of the actual value of saturation magnetization at H_{sat} [42]. To account for the epistemic uncertainty in M_{sat}, we define a random variable, $\mathbf{S}$, given by

$$\mathbf{S} \sim \mathcal{N}\left(\mu_{\text{sat}}, \sigma_{\text{sat}}^2\right), \tag{4.11}$$

where we assume that $\mu_{\text{sat}} = 2$ T and $\sigma_{\text{sat}} = 0.02$ T. The distribution can be observed in Fig. 4.6. Our methodology is independent of these assumptions. Thus, given the actual measurements are available, the proposed methodology can be applied without reservation. The use of normal distribution to model the uncertainty is based on our assumption that the value of M_{sat} is likely to be near the mean value, μ_{sat}.

We extrapolate each *M*-*H* curve till saturation implementing the following procedure. First, we obtain a sample, s, from $\mathbf{S}$ for each *M*-*H* curve. The sample, s, represents the value of M_{sat} for the corresponding curve. Second, we append $\{H_{\text{sat}}, s\}$ to the existing values of H and M of the *M*-*H* curve. Third, we interpolate the H, M data points using a shape preserving piecewise cubic Hermite polynomial (PCHIP) function, given by $M(H)$, such that the slope at the last data point is zero. Fourth, we sample 50 discrete equally spaced values of H, $\mathbf{h}_e$, extending till H_{sat}. Fifth, at $\mathbf{h}_e$, we obtain the corresponding M values, $M(\mathbf{h}_e)$ to obtain *M*-*H* data points till saturation. Finally, we transform the *M*-*H* data points to obtain the *B*-*H* curve till saturation using Eq. (4.10).

At the conclusion of this section, we can completely define the uncertainty in *B*-*H* curves using 7 random variables, namely, $\mathbf{Z}_{\text{hst}}$, $\mathbf{Z}_{\text{hso}}$, $\mathbf{Z}_{\text{hro}}$, $\mathbf{Z}_{\text{hrm}}$, $\mathbf{Z}_{\text{hri}}$, $\mathbf{U}$ and $\mathbf{S}$.

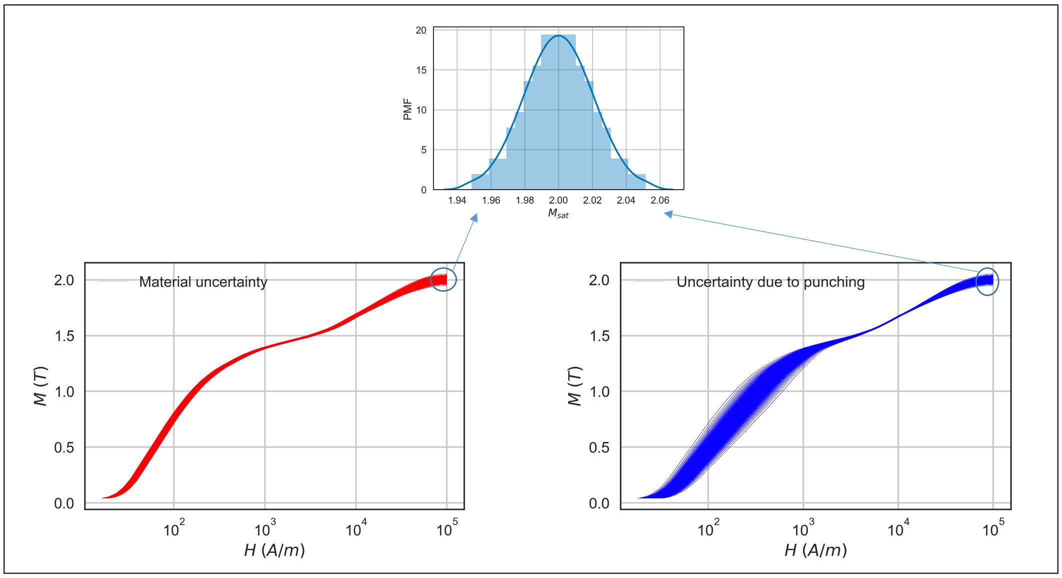

Fig. 4.6.: Illustration of epistemic uncertainty in saturation flux density

4.4 Modeling of uncertainty in remanent flux density of permanent magnets (Extended work)

The modeling of uncertainty in remanent flux density (B_r) of the permanent magnets is an extended work of this thesis. The variability in B_r can be local or global. The local variation corresponds to the condition where the variation of B_r of one magnet of the PMSM is different from the other where as the global variation corresponds to the condition where the variation of B_r of all the magnets is the same. In this study, we consider the global variation of B_r and model it with a normal distribution such that the nominal value of B_r is equal to the mean value of the distribution and its standard deviation is equal to 1% of the mean value [26]. Thus, the random variable reflecting uncertainty in B_r is given by,

$$\mathbf{B}_r \sim \mathcal{N}(\mu_{\mathrm{Br}}, \sigma_{\mathrm{Br}}^2) \tag{4.12}$$

where $\mu_{\mathrm{Br}} = 1.23$ T, the nominal value of B_r of the magnet used in 2004 model of Toyota Prius traction motor [43] and $\sigma_{\mathrm{Br}} = 0.0123$ T.

5. CONSTRUCTION OF SURROGATE MODELS

This chapter provides the methodology used for constructing surrogate models using Gaussian process (GP) regression). Section 5.1 gives a concise description of the principles of GP regression. Subsequently, in Section 5.2, the methodology of constructing a surrogate model using GP regression that learns the principal components of the output torque from a permanent magnet synchronous machine (PMSM) spanning the entire operating range is given as well as a detailed procedure for validation of the proposed surrogate model that predicts the torque waveform is illustrated. The last section gives a detailed overview of the development of surrogate models for predicting average torque and average flux linkages of the PMSM which is part of the extended work.

5.1 Overview of Gaussian process regression

Gaussian process (GP) is a stochastic process defined as a collection of random variables any finite number of which has a multivariate normal distribution. It can be referred to as an extension of multivariate random Gaussian variables into infinite dimensions. Using Bayes rule, GP combines the prior knowledge about a model/system with the observations that results in an updated state of knowledge about the system known as the posterior GP. The posterior GP complies with the prior information and the observations simultaneously. This phenomena is used in regression to build an inexpensive surrogate model of a detailed expensive model.

Let us consider a data set, $\mathcal{D} = \{\mathbf{Y}, \mathbf{X}\}$, where $\mathbf{Y}$ is the output, potentially noisy, observation,

$$\mathbf{Y} = \{y^{(1)}, ..., y^{(N)}\}, \tag{5.1}$$

at inputs $\mathbf{X}$ given by

$$\mathbf{X} = \{\mathbf{x}^{(1)}, ..., \mathbf{x}^{(N)}\}. \tag{5.2}$$

A GP describes a probability measure on a space of functions. This measure encodes our prior beliefs regarding the output of a computationally expensive model whose surrogate is being built. Using Bayes rule, GP regression combines this prior beliefs with the input-output observations (evaluated using the expensive model) to obtain the posterior GP. The posterior GP is referred to as a Bayesian surrogate. For making point wise prediction on any input, the median of the posterior GP is used. One can also derive predictive error bars about the output that corresponds to the epistemic uncertainty (induced by the limited availability of the input-output observations) with the help of the variance predicted by the posterior GP. For learning a response surface and making prediction using GP, a three step procedure is followed:

1. Modeling the prior state of knowledge about the response surface.
2. A model describing the measurement process
3. A depiction of the posterior state of knowledge

5.1.1 Prior state of knowledge

The prior state of knowledge is modeled by taking into account the trends of the response of the computationally expensive numerical model whose surrogate is being constructed. The trends of the output observation such as continuity, differentiability, etc. correspond to the prior state of knowledge. Such prior state of knowledge about the function of interest, $f(\cdot)$, is described by assigning a GP prior. Formally, $f(\cdot)$ is said to be a GP with mean function $\mu(\cdot;\boldsymbol{\theta})$ and covariance function $k(\cdot,\cdot;\boldsymbol{\theta})$. Thus, $f(\cdot)$ is defined as

$$f(\cdot)|\boldsymbol{\theta} \sim \mathcal{GP}(f(\cdot)|\mu(\cdot;\boldsymbol{\theta}), k(\cdot;\boldsymbol{\theta})), \tag{5.3}$$

where $\boldsymbol{\theta}$ represents the hyper-parameters of the model. The mean and covariance functions along with their hyper-parameters reflect our prior knowledge and beliefs about the response. Thus, we also define a prior over the hyper-parameters given by

$$\boldsymbol{\theta} \sim p(\boldsymbol{\theta}). \tag{5.4}$$

Without any prior knowledge about the behavior of the response/output, the mean function is assumed to be zero [30]. The covariance function, also called the covariance kernel, is the most crucial part of GP. It measures the similarity between two input points in the parameter space. Throughout the present study, the squared exponential (SE) kernel (with automatic relevance determination (ARD)) is used, which is given by

$$k_k(x, \mathbf{x}') = \sigma_{f,n}^2 exp(-\frac{1}{2}(\mathbf{x} - \mathbf{x}')^T \mathbf{L}^{-1}(\mathbf{x} - \mathbf{x}')). \tag{5.5}$$

For any input set $\mathbf{X}$, using Eq. (5.3), the prior is defined for the GP model on the output observations, $\mathbf{Y}$,

$$\mathbf{f} = \{f(\mathbf{x}^{(1)}), ..., f(\mathbf{x}^{(N)})\}. \tag{5.6}$$

The prior distribution of $\mathbf{f}$ is given by

$$\mathbf{f}|\boldsymbol{\theta} \sim \mathcal{N}(\mathbf{f}|\boldsymbol{\mu}, \mathbf{K}), \tag{5.7}$$

where $\mathcal{N}(\cdot|\boldsymbol{\mu}, \mathbf{K})$ is the PDF of a multivariate normal random variable with mean vector, $\boldsymbol{\mu}$ and covariance matrix $\mathbf{K}$. $\boldsymbol{\mu}$ is given by

$$\boldsymbol{\mu} = \mu(\mathbf{X}; \boldsymbol{\theta}) = \begin{pmatrix} \mu(\mathbf{x}^{(1)}; \boldsymbol{\theta}) \\ \vdots \\ \mu(\mathbf{x}^{(N)}; \boldsymbol{\theta}) \end{pmatrix} \tag{5.8}$$

and $\mathbf{K} \in \mathbb{R}^{NXN}$ is the covariance matrix given by

$$\mathbf{K}(\mathbf{X}, \mathbf{X}; \boldsymbol{\theta}) = \begin{pmatrix} k(\mathbf{x}^{(1)}, \mathbf{x}^{(1)}; \boldsymbol{\theta}) & \dots & k(\mathbf{x}^{(1)}, \mathbf{x}^{(N)}; \boldsymbol{\theta}) \\ \vdots & \ddots & \vdots \\ k(\mathbf{x}^{(N)}, \mathbf{x}^{(1)}; \boldsymbol{\theta}) & \dots & k(\mathbf{x}^{(N)}, \mathbf{x}^{(N)}; \boldsymbol{\theta})) \end{pmatrix}. \tag{5.9}$$

5.1.2 Measurement process

The measurement process is required to quantify and model any measurement error associated with the observations, $\mathbf{Y}$. The simplest way to model this measurement error is to consider identical independently distributed gaussian noise about each observation. For simplicity we assume that the gaussian noise has zero mean and variance of σ^2. That is given by

$$y^{(i)}|f(\mathbf{x}^{(i)}), \sigma \sim \mathcal{N}(y^{(i)}|f(\mathbf{x}^{(i)}), \sigma^2), \tag{5.10}$$

where σ is another hyper-parameter on which a prior is defined as

$$\sigma \sim p(\sigma). \tag{5.11}$$

Assuming independence of the outputs, we can obtain the likelihood by applying the sum rule of probability and some standard integrals which is given by

$$\mathbf{Y}|\mathbf{X}, \boldsymbol{\theta}, \sigma \sim \mathcal{N}(\mathbf{Y}|\boldsymbol{\mu}, \mathbf{K} + \sigma^2\mathbf{I}_N). \tag{5.12}$$

5.1.3 Posterior of the Gaussian Process

With the help of Bayes rule the prior state of knowledge (Eq. (5.3)) is combined with the likelihood of the observations (Eq. (5.12)), to give the posterior distribution/posterior GP,

$$\mathbf{f}(\cdot)|\mathbf{X}, \mathbf{f}(\mathbf{X}), \boldsymbol{\theta}, \sigma \sim \mathcal{GP}(f(\cdot)|\tilde{\mu}(\cdot), \tilde{k}(\cdot, \cdot)), \tag{5.13}$$

where $\tilde{\mu}(\cdot)$ is the posterior mean given by

$$\begin{aligned} \tilde{\mu}(\mathbf{x}^{(*)}) &= \tilde{\mu}(\mathbf{x}^{(*)}; \boldsymbol{\theta}) \\ &= \mathbf{K}(\mathbf{x}^{(*)}, \mathbf{X})(\mathbf{K}(\mathbf{X}, \mathbf{X}) + \sigma^2\mathbf{I}_T)^{-1}\mathbf{f}(\mathbf{X}), \end{aligned} \tag{5.14}$$

and the posterior covariance, $\tilde{k}(\mathbf{x}^{(*)}, \mathbf{x}^{(*)\prime})$, is given by

$$\begin{aligned} &\tilde{k}(\mathbf{x}^{(*)}, \mathbf{x}^{(*)\prime}) = \tilde{k}(\mathbf{x}^{(*)}, \mathbf{x}^{(*)\prime}; \boldsymbol{\theta}, \sigma) \\ &= \mathbf{K}(\mathbf{x}^{(*)}, \mathbf{x}^{(*)\prime}) \\ &- \mathbf{K}(\mathbf{X}, \mathbf{X})(\mathbf{K}(\mathbf{x}^{(*)}, \mathbf{X}) + \sigma^2\mathbf{I}_T)^{-1}\mathbf{K}(\mathbf{X}, \mathbf{x}^{(*)}). \end{aligned} \tag{5.15}$$

For obtaining the distribution of the best hyper-parameters, the posterior distribution of the hyper-parameters is obtained by combining Eq. (5.4) and Eq. (5.11) with the likelihood. The posterior distribution of the hyper-parameters is given by

$$p(\boldsymbol{\theta}, \sigma|\mathbf{X}, \mathbf{Y}) \propto p(\mathbf{Y}|\mathbf{X}, \boldsymbol{\theta}, \sigma)p(\boldsymbol{\theta})p(\sigma). \tag{5.16}$$

5.1.4 Obtaining the hyper-parameters

In general, the analytic solution to Eq. (5.16) is intractable. Thus, ideally applying sampling techniques like Markov chain Monte Carlo (MCMC), the range of best fit hyper-parameters is obtained. However, this method is computationally intensive. Instead, we obtain a single best fit hyper-parameter that maximizes the likelihood of the observations. To avoid numerical issues, the logarithm of the likelihood (Eq. (5.12)) is used.

$$\begin{aligned} log(p(\mathbf{Y}|\mathbf{X}, \boldsymbol{\theta}, \sigma)) = &-\frac{1}{2}(\mathbf{Y} - \boldsymbol{\mu})^T(\mathbf{K} + \sigma^2\mathbf{I}_N)^{-1}(\mathbf{Y} - \boldsymbol{\mu}) \\ &- \frac{1}{2}log|\mathbf{K} + \sigma^2\mathbf{I}_N| - \frac{N}{2}log2\pi \end{aligned} \tag{5.17}$$

Differentiating Eq. (5.17) partially w.r.t. any parameter ϕ, where $\phi = \sigma$ or θ_i, we get

$$\begin{aligned} \frac{\partial}{\partial \phi}(log(p(\mathbf{Y}|\mathbf{X}, \boldsymbol{\theta}, \sigma))) = &\frac{1}{2}tr[\{(\mathbf{K} + \sigma^2\mathbf{I}_N)^{-1}(\mathbf{Y} - \boldsymbol{\mu}) \\ &((\mathbf{K} + \sigma^2\mathbf{I}_N)^{-1}(\mathbf{Y} - \boldsymbol{\mu}))^T \\ &- (\mathbf{K} + \sigma^2 I_N)^{-1}\}\frac{\partial(\mathbf{K} + \sigma^2 I_N)}{\partial \phi}. \end{aligned} \tag{5.18}$$

The point estimate of the hyper-parameters is called the maximum likelihood estimate (MLE). MLE is a simpler approach to obtain the best hyper-parameters with significant accuracy. Thus, we use MLE to estimate the hyper-parameters in this study. We solve Eq. (5.18) using the BFGS optimization algorithm.

5.2 Development of the surrogate model for predicting the torque waveform of PMSM

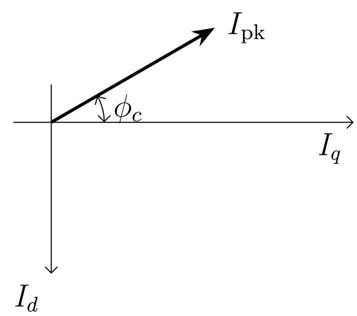

Fig. 5.1.: Diagram showing I_{pk} and ϕ_c in rotor reference frame

Table 5.1.: Distribution of input parameters

Parameter	**Type of distribution**	**Range**	**Statistics**
$\mathbf{I}_{\mathrm{pk}}$ (A)	Uniform	[0, 250]	Mean = 125
$\mathbf{\Phi}_c$ (deg)	Uniform	[0, 90]	Mean = 45
$\mathbf{Z}_{\mathrm{hst}}$	Uniform	[−1.368, 1.971]	Mean = 0.3015
$\mathbf{Z}_{\mathrm{hso}}$	Uniform	[−1.368, 1.971]	Mean = 0.3015
$\mathbf{Z}_{\mathrm{hro}}$	Uniform	[−1.368, 1.971]	Mean = 0.3015
$\mathbf{Z}_{\mathrm{hri}}$	Uniform	[−1.368, 1.971]	Mean = 0.3015
$\mathbf{Z}_{\mathrm{hrm}}$	Uniform	[−1.368, 1.971]	Mean = 0.3015
U	Uniform	[−0.1, 0.1]	Mean = 0
S	Gaussian	[−∞, ∞]	Mean = 2, Var = 0.02

Given a nominal geometry of a PMSM, our goal is to study the effect of B-H uncertainties on its torque profile in the entire operating range of the machine. To this end, the FE simulator is parameterized by the operating points and the uncertain B-H curves. Furthermore, the operating points in the entire range can be obtained by varying $\mathbf{I}_{\text{pk}}$, the amplitude of the current and $\mathbf{\Phi}_c$, the current angle (see Fig. 5.1) uniformly whereas in Section 4.1, we have shown that the B-H uncertainties can be completely defined by 7 different parameters. Thus, these parameters constitute a 9-D parameter space shown in Table 5.1.

To overcome the computational cost of the evaluations from the FE simulator, we develop an inexpensive surrogate model with the parameters of the FE simulator as input. We train the surrogate with input-output observations such that the inputs correspond to the samples from a normalized input space and the outputs correspond to the torque waveforms evaluated using the FE simulator at the mapped values of these normalized input samples. Using Latin hypercube sampling algorithm (LHS), we draw normalized input samples from a 9-D space, $\Omega \in [0,1]^9$ for training the surrogate. Let $\mathbf{x}^{(n)} \in \mathbb{R}^9$ be one of the input samples. To obtain the mapped inputs, the values in $\mathbf{x}^{(n)}$ are mapped to the distributions stated in Table 5.1. The mapping of any value, x, from a normalized input sample, $\mathbf{x}^{(n)}$, to an uniform distribution is given by

$$x_m = l_b + (u_b - l_b) * x, \tag{5.19}$$

where x_m is the mapped input, l_b and u_b are the lower and upper bounds of the concerned uniform distribution respectively. Thus, using Eq. (5.19), we map the first 8 values of $\mathbf{x}^{(n)}$ to the distributions in the first 8 rows of Table 5.1 to obtain the samples i_{pk}, ϕ_c, z_{hst}, z_{hso}, z_{hro}, z_{hri}, z_{hrm} and u. Using Eq. (4.6), we obtain the B-H curves corresponding to the degraded zones in Table 4.1 from z_{hst}, z_{hso}, z_{hro}, z_{hri} and z_{hrm} respectively. The sample, u, is used to obtain the B-H curve reflecting material uncertainty using Eq. (4.9). The final value in $\mathbf{x}^{(n)}$ is mapped to s by taking its inverse transformation with respect to $\mathbf{S}$. Thereafter, the obtained B-H curves are extrapolated till saturation using the sample, $\{H_{\text{sat}}, s\}$ and following the procedure stated in Section 4.3. These extrapolated B-H curves along with the samples, i_{pk} and

ϕ_c are used to run the FE simulator to obtain the torque waveform corresponding to the input $\mathbf{x}^{(n)}$.

Given a total of N training samples are obtained, the entire training input data set is given by $\mathbf{X} = \left(\mathbf{x}^{(1)}, \ldots, \mathbf{x}^{(N)}\right) \in \mathbb{R}^{9 \times N}$. In practice, for a separate validation set, we predict the torque waveform using the trained surrogate and compare the prediction against the actual torque waveform from the FE simulator. N is iteratively increased till the decided error criteria between the predicted torque waveform and the actual torque waveform is within a satisfactory tolerance. The methodology to train the surrogate is described in detail in the following sections.

5.2.1 Dimensionality reduction of the torque waveform

The output torque waveform, $\mathbf{t}^{(n)} \in \mathbb{R}^M$, at any input point, is a function of rotor positions. The output dimension, M, depends on the resolution of the discretization of air gap in the FE simulator. In practice, the resolution is kept high to reduce numerical errors, resulting in high output dimensionality. Taking advantage of PCA, we seek to reduce this dimensionality. Let the total output torque matrix obtained at the training input set be $\mathbf{T} = \left(\mathbf{t}^{(1)}, \ldots, \mathbf{t}^{(N)}\right) \in \mathbb{R}^{M \times N}$. Performing PCA on the covariance matrix of $\mathbf{T}$, $\mathbf{Q}_t$, we can decompose each column of $\mathbf{T}$, $\mathbf{t}^{(i)}$, as:

$$\mathbf{t}^{(i)} = \boldsymbol{\mu}_t + \sum_{m=1}^{M} \sqrt{\lambda_{t,m}} z_{t,m}^{(i)} \boldsymbol{\phi}_{t,m}, \tag{5.20}$$

where $\lambda_{t,m}$ is the m-th largest eigenvalue of $\mathbf{Q}_t$, $\boldsymbol{\phi}_{t,m}$ the corresponding eigenvector, $z_{t,m}^{(i)}$ is the i-th PC score of the m-th PC, $\mathbf{z}_{t,m} = \left(z_{t,m}^{(1)}, \ldots, z_{t,m}^{(N)}\right)$ and $\boldsymbol{\mu}_t$ is the row-wise mean of $\mathbf{T}$.

We keep the first $L = M'$ ($M \gg M'$) significant PCs and ignore the rest. These L PCs are learned by scalar Gaussian process (GP) functions to build the surrogate that predicts the torque waveform. We shall show the methodology to chose the number of significant PCs in the subsequent section.

5.2.2 Multi-output Gaussian process regression

For constructing the surrogate, each PC, $\mathbf{z}_{t,m}$, is learned by a scalar GP function, f_m. The PC score of $\mathbf{z}_{t,m}$ is defined as

$$z_{t,m}^{(n)} = f_m(\mathbf{x}^{(n)}) + \epsilon^{(n)}. \tag{5.21}$$

where $\epsilon^{(n)}$ is a standard Gaussian distributed noise used to capture the numerical error in the FE simulator. For notational simplicity, we drop the implicit m subscript from all the following derivations. The prior assumption for f is modeled by a GP prior given by

$$f\left(\cdot\right)|\boldsymbol{\theta} \sim \mathcal{GP}\left(f\left(\cdot\right)|0, k\left(\cdot,\cdot;\boldsymbol{\theta}\right)\right), \tag{5.22}$$

where $k(\cdot,\cdot;\boldsymbol{\theta})$ is the covariance function and $\boldsymbol{\theta}$ represents all the hyper-parameters of the model. We use the squared exponential function as the covariance function of the GP which is defined as

$$k\left(\mathbf{x},\mathbf{x}';\boldsymbol{\theta}\right) = \sigma_f^2 exp\left(-\frac{1}{2}\sum_{i=1}^{9}\left(\frac{x_i - x_i'}{d_i}\right)^2\right), \tag{5.23}$$

where d_i's, the length scales corresponding to each input dimension and σ_f^2, the signal variance of the covariance function constitute the hyper-parameters, $\boldsymbol{\theta}$.

The GP prior is modeled as a multivariate normal distribution of $f(\cdot)$ at $\mathbf{X}$, given by

$$\mathbf{f}\left(\mathbf{X}\right)|\mathbf{X},\boldsymbol{\theta} \sim \mathcal{N}\left(\mathbf{0},\mathbf{K}\right), \tag{5.24}$$

where $\mathbf{K} \in \mathbb{R}^{N\times N}$ is the covariance matrix such that each of its element $K_{(i,j)}$ is given by

$$K_{(i,j)} = k\left(\mathbf{x}^{(i)},\mathbf{x}^{(j)};\boldsymbol{\theta}\right). \tag{5.25}$$

We acquire the PC scores, $\mathbf{y}$, at the input data points, $\mathbf{X}$, by performing PCA on the covraiance matrix of the output torque obtained from the FE simulator. Additionally, we model the numerical errors in the FE simulator, $\boldsymbol{\epsilon}$, assuming that it is distributed normally about $\mathbf{y}$ with a variance, σ^2. By using properties of Gaussian integrals and the sum rule of probability theory the Gaussian likelihood on $\mathbf{y}$ at $\mathbf{X}$ is given by

$$\mathbf{y}\left(\mathbf{X}\right)|\mathbf{X},\boldsymbol{\theta},\sigma \sim \mathcal{N}\left(\mathbf{0},\mathbf{K}+\sigma^2\mathbf{I}_N\right), \tag{5.26}$$

where $\mathbf{I}_N \in \mathbb{R}^{N\times N}$ is an identity matrix. Note that σ is one more hyperparameter.

Using Bayes rule, the prior state of knowledge given by Eq. (5.22) is combined with the likelihood given by Eq. (5.26), to yield the posterior GP,

$$f(\cdot)\,|\mathbf{X},\mathbf{y},\boldsymbol{\theta},\sigma \sim \mathcal{GP}\left(f(\cdot)\,|\tilde{\mu}(\cdot;\boldsymbol{\theta}),\tilde{k}(\cdot,\cdot;\boldsymbol{\theta},\sigma)\right), \tag{5.27}$$

where $\tilde{\mu}(\cdot;\boldsymbol{\theta})$ is the posterior mean and $\tilde{k}(\cdot,\cdot;\boldsymbol{\theta},\sigma)$ is the posterior covariance function. In practice, we work with the predictive probability density at a single input point, $\mathbf{x}^{(*)}$, given by,

$$\mathbf{f}\left(\mathbf{x}^{(*)}\right)|\mathbf{x}^{(*)},\boldsymbol{\theta},\sigma \sim \mathcal{N}\left(\tilde{\mu}\left(\mathbf{x}^{(*)};\boldsymbol{\theta}\right),\tilde{k}\left(\mathbf{x}^{(*)},\mathbf{x}^{(*)};\boldsymbol{\theta},\sigma\right)\right), \tag{5.28}$$

where the predictive mean is given by

$$\tilde{\mu}\left(\mathbf{x}^{(*)};\boldsymbol{\theta}\right) = \mathbf{k}^{\mathrm{T}}\left(\mathbf{K}+\sigma^2\mathbf{I}_N\right)^{-1}\mathbf{y} \tag{5.29}$$

and the predictive covariance is given by

$$\begin{aligned}\tilde{k}\left(\mathbf{x}^{(*)},\mathbf{x}^{(*)};\boldsymbol{\theta},\sigma\right) &= k\left(\mathbf{x}^{(*)},\mathbf{x}^{(*)};\boldsymbol{\theta},\sigma\right)\\ &\quad - \mathbf{k}^{\mathrm{T}}\left(\mathbf{K}+\sigma^2\mathbf{I}_N\right)^{-1}\mathbf{k}.\end{aligned} \tag{5.30}$$

The vector $\mathbf{k}$ is obtained by evaluating the covariance function at $\mathbf{x}^{(*)}$ and the input training points $\mathbf{X}$. Thus, $\mathbf{k}$ is given by

$$\mathbf{k} = \left(k\left(\mathbf{x}^{(*)},\mathbf{x}^{(1)};\boldsymbol{\theta}\right),\ldots,k\left(\mathbf{x}^{(*)},\mathbf{x}^{(N)};\boldsymbol{\theta}\right)\right). \tag{5.31}$$

The hyperparameters are obtained by maximizing the likelihood given in Eq. (5.26) following the procedure stated in [30]. Thus, for any input set $\mathbf{x}^{(*)}$, using Eq. (5.27), the surrogate model predicts the PC score of the m-th PC. One of the major advantages of GP based surrogate model is that not only they predict the mean at $\mathbf{x}^{(*)}$, $\tilde{\mu}(\mathbf{x}^{(*)};\boldsymbol{\theta})$, they also predict the predictive error bars which capture the epistemic uncertainty due to limited training data set. Based on the epistemic uncertainty, the training sets can be sampled strategically.

5.2.3 Validation of the surrogate model

The accuracy of the trained surrogate model is tested on a separate set of inputs called the validation set. Let the validation input set be $\mathbf{X}_v = \left(\mathbf{x}_v^{(1)}, \ldots, \mathbf{x}_v^{(P)}\right) \in \mathbb{R}^{9\times P}$ containing P samples from the parameter space obtained using LHS. At these inputs, let $\mathbf{Z}_{\text{tv}} = \left(\mathbf{z}_{\text{tv}}^{(1)}, \ldots, \mathbf{z}_{\text{tv}}^{(P)}\right) \in \mathbb{R}^{L\times P}$ be the predictive mean of the truncated PC scores from the surrogate model, where for each input, $\mathbf{x}^{(p)}$, the corresponding predicted PC scores for L PCs are given by $\mathbf{z}_{\text{tv}}^{(p)} = \left(z_{\text{tv},1}^{(p)}, \ldots, z_{\text{tv},L}^{(p)}\right)$. Performing inverse PCA on $\mathbf{Z}_{\text{tv}}$, the predicted torque matrix, $\mathbf{T}_v \in \mathbb{R}^{M\times P}$ is obtained where each column of $\mathbf{T}_v$, $\mathbf{t}_v^{(i)}$, is given by

$$\mathbf{t}_v^{(i)} = \boldsymbol{\mu}_t + \sum_{m=1}^{L} \sqrt{\lambda_{t,m}}\, z_{\text{tv},m}^{(i)} \boldsymbol{\phi}_{t,m}, \tag{5.32}$$

where $\boldsymbol{\mu}_t$, $\lambda_{t,m}$ and $\phi_{t,m}$ are obtained in Eq. (5.20).

Additionally, the output torque is independently calculated from the FE simulator at these P validation inputs. Let the torque matrix obtained from the FE simulator be called the actual torque matrix, $\mathbf{T}_a \in \mathbb{R}^{M\times P}$. The error criteria used in this study to evaluate the convergence is the relative L_2 norm of the error between the predicted torque matrix and the actual torque matrix, where the relative L_2 norm of the error is given by

$$\text{relative } L_2\text{-norm error} = \frac{||\mathbf{T}_v - \mathbf{T}_a||_2}{||\mathbf{T}_v||_2}. \tag{5.33}$$

The training samples, N, are increased iteratively until the relative L_2-norm of the error is within a desired tolerance.

5.2.4 Assessment of the Surrogate Model

In this section, we define the procedure of conducting the assessment of the surrogate model that is used to carry out the propagation study. The response from the FE simulator used in our study corresponds to a $M = 32$ dimensional vector of torque waveform as a function of rotor position. However, while training the surrogate, we reduce the output dimension from $M = 32$ to $M = 8$ by performing PCA. We train

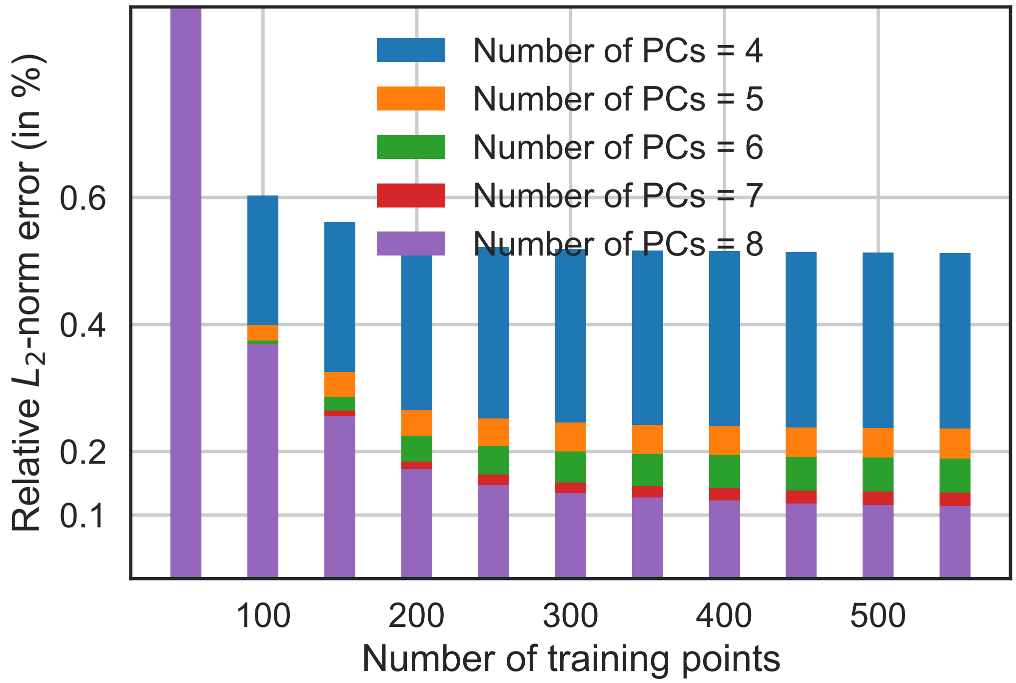

Fig. 5.2.: Illustration of convergence of relative L_2-norm error between $\mathbf{T}_a$ and $\mathbf{T}_v$ with number of training points

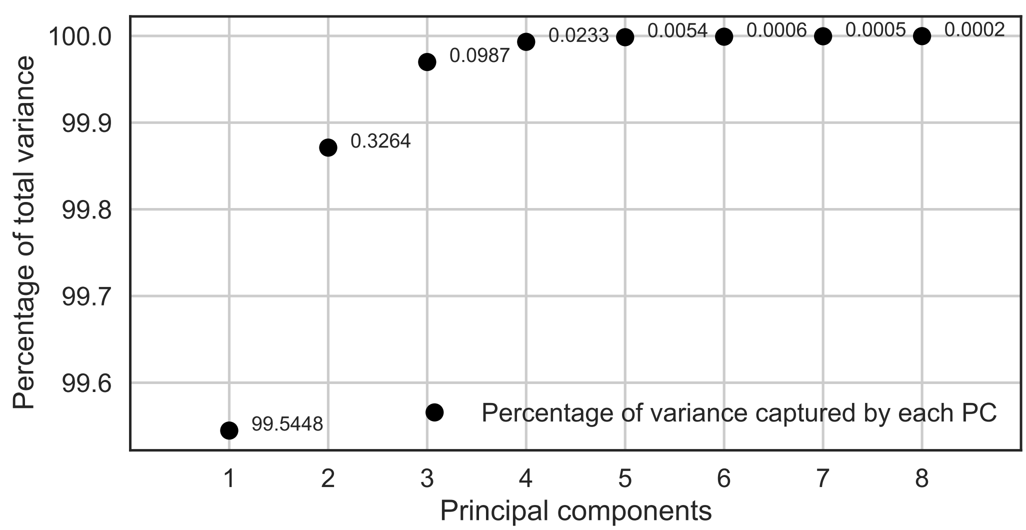

Fig. 5.3.: Percentage of variance captured by 8 PCs of $\mathbf{T}_a$

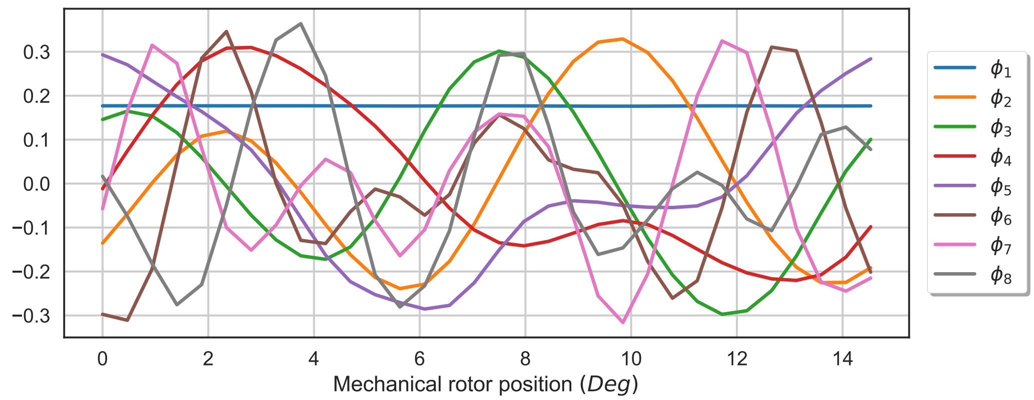

Fig. 5.4.: Eigenvectors corresponding to the retained PCs of $\mathbf{T}_a$

the surrogate with $N = 550$ input points and validate it with an additional $P = 100$ points. The convergence of the relative L_2-norm error (see Eq. (5.33)) for the 8 PCs can be observed in Fig. 5.2. It can be observed that with further increase in number of training points the relative L_2-norm error doesn't go down significantly. Thus, the error is said to have converged. We choose the number of significant PCs based on the amount of variance captured by them. By keeping 8 PCs, we can capture more than 99.9995% variance (see Fig. 5.3) from the original data set. Thus, 8 PCs are kept. We also observe the eigenvectors of the retained PCs in Fig. 5.4.

Additionally, we conduct reconstruction studies with 8 PCs to quantify the error due to the approximation caused by the dimensionality reduction using PCA. The reconstruction study is conducted as follows. First we obtain a test set containing the output torque waveforms from the FE simulator at a test input set. The torque waveforms from the validation set, $\mathbf{T}_v$, is considered as the test set in our study. Thereafter, $\mathbf{T}_v$ is projected into the low-dimensional space by using Eq. (5.20). In this low-dimensional space, first 8 PCs are retained and rest are ignored. Now, the reconstruction is performed by projecting the PCs back into the high-dimensional space using Eq. (5.32). Let this reconstructed matrix be given by $\hat{\mathbf{T}}_v$. The absolute

L_2-norm error between $\mathbf{T}_v$ and $\hat{\mathbf{T}}_v$ is computed where the absolute L_2-norm error is given by

$$\text{absolute } L_2\text{-norm error} = \left\| \mathbf{T}_v - \hat{\mathbf{T}}_v \right\|_2 . \tag{5.34}$$

Fig. 5.5a shows the histogram of the absolute L_2-norm error. It can be observed that the maximum error is approximately close to 3 N-m and from the Fig. 5.5b we can infer that it occurs near the high torque region and doesn't introduce significant inaccuracy in the surrogate model.

Sensitivity study corresponding to punching uncertainty

Next, we perform a validation study of the trained surrogate model to analyze its sensitivity towards *B*-*H* curves in the degraded zones of the PMSM. Here, the idea is to observe how the QoIs change when *B*-*H* curves in the degraded regions change using both the FE simulator and the surrogate model (a study similar to the one performed in Chapter 2). This study is performed at the 25 operating points reported in Table 2.2. Two *B*-*H* curves, the least degraded one and the most degraded one, are selected for all the regions affected by punching (see Fig. 5.6). Additionally, all the degraded zones are assumed to follow a single *B*-*H* characteristic. For the region reflecting material uncertainty, the *B*-*H* curve corresponding to the mean value of $\mathbf{U}$ (variable reflecting material uncertainty) from Table 5.1 is selected. All the *B*-*H* curves are extrapolated to the saturation value that corresponds to the mean value of $\mathbf{S}$ (variable reflecting uncertainty in saturation flux density).

The *B*-*H* curves and the operating points act as inputs to the FE simulator for obtaining 50 torque waveforms; 1 waveform corresponding to each degraded *B*-*H* curve at each operating point. Similarly, the predicted torque waveforms from the surrogate model are also evaluated at the normalized inputs corresponding to the *B*-*H*curves and the operating points. The percentage change in the QoIs at all of these 25 operating points for both the degraded *B*-*H* curves is separately visualized

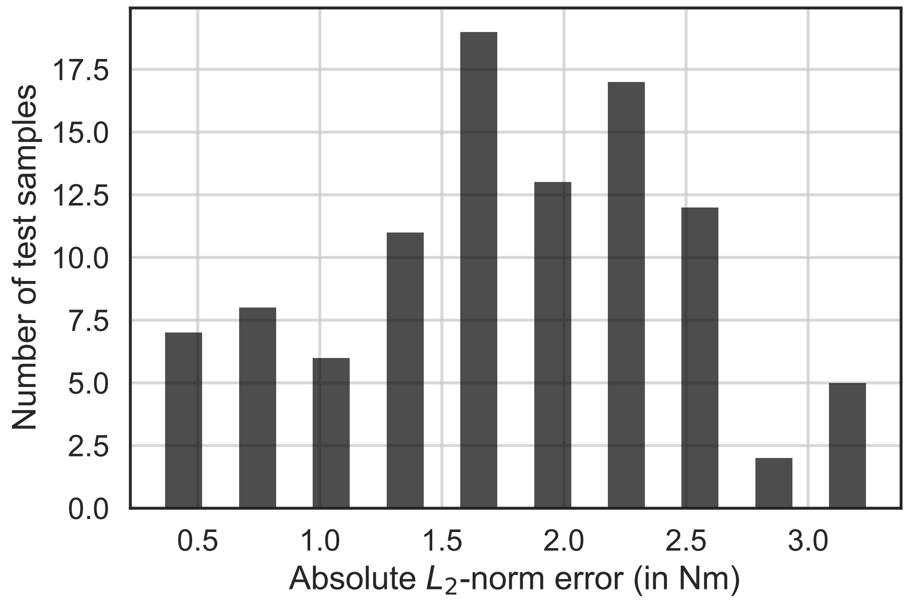

(a)

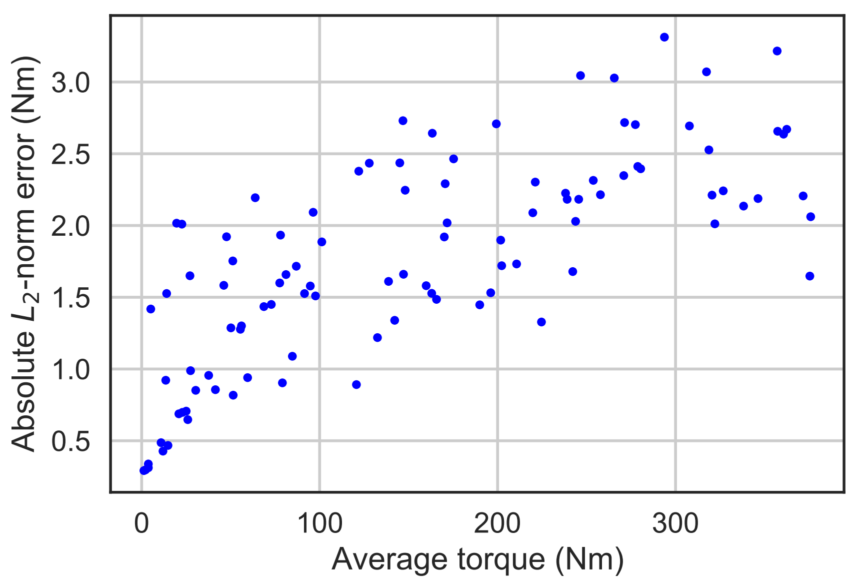

(b)

Fig. 5.5.: Study to analyse the reconstruction error from the surrogate. (a) Histogram of absolute L_2-norm error of reconstruction using the 8 PCs by the surrogate model, (b) absolute L_2-norm error vs Average torque

for the FE simulator and the surrogate model where the percentage change is given by

$$Q_c = \frac{Q_m - Q_l}{Q_m}100, \tag{5.35}$$

where Q_c is the change of QoI in percentage, Q_m is the QoI corresponding to the most degraded curve and Q_l is the QoI corresponding to the least degraded curve.

Thereafter, we compare the change of QoIs obtained from the FE simulator and the surrogate model. Figs. 5.7, 5.8, 5.9, 5.10 show the torque waveforms corresponding to this study. Fig. 5.12 shows the scatter plot representing the change in average torque and its corresponding values are reported in Table 5.2. There is an appreciable match between the differences computed using the FE simulator and the surrogate model. Fig. 5.13 and the values from the Table 2.7 show that the change in the sixth harmonic component of torque from the FE simulator and the surrogate model do not show significant agreement. A similar phenomena is observed in the difference of twelfth harmonic component of torque as well (see Fig. 5.14 and the values reported in Table 5.4). Thus, although the surrogate predicts the sensitivity of average torque due to the uncertainty in punching accurately, it fails to predict the sensitivity of sixth and twelfth harmonic components of torque. The failure of the surrogate model in predicting the sixth and twelfth harmonic components of torque can be because of the approximation of the model by dimensionality reduction using PCA. If the change in any QoI is smaller than the approximation error, the surrogate won't be able to predict the change with adequate accuracy.

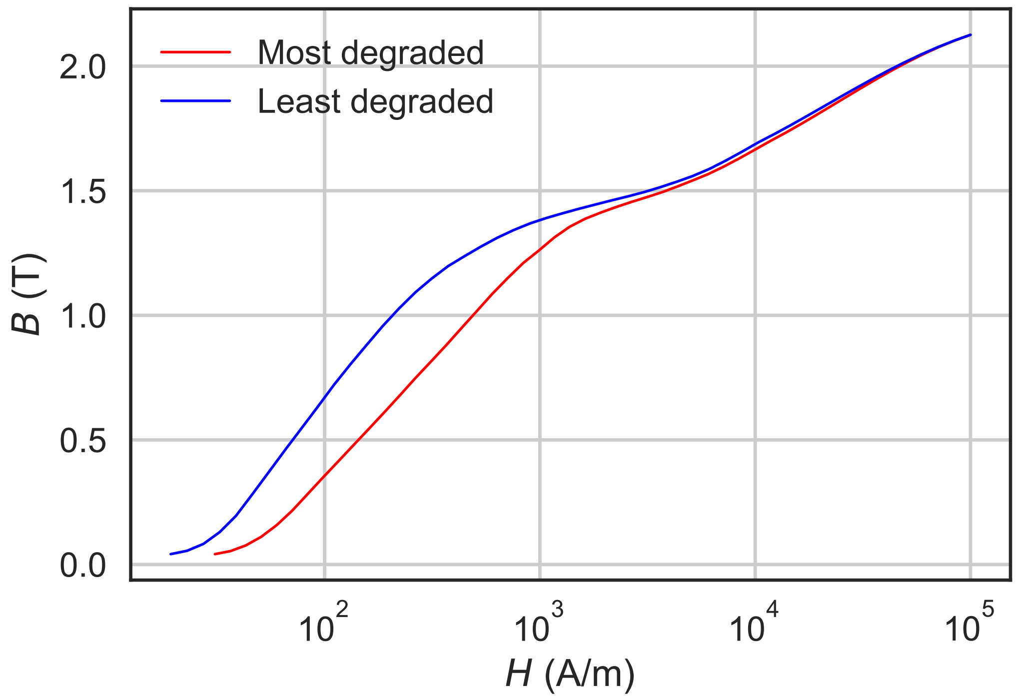

Fig. 5.6.: *B*-*H* curve showing most degraded and least degraded curve that reflect the magnetic characteristics of the degraded zones

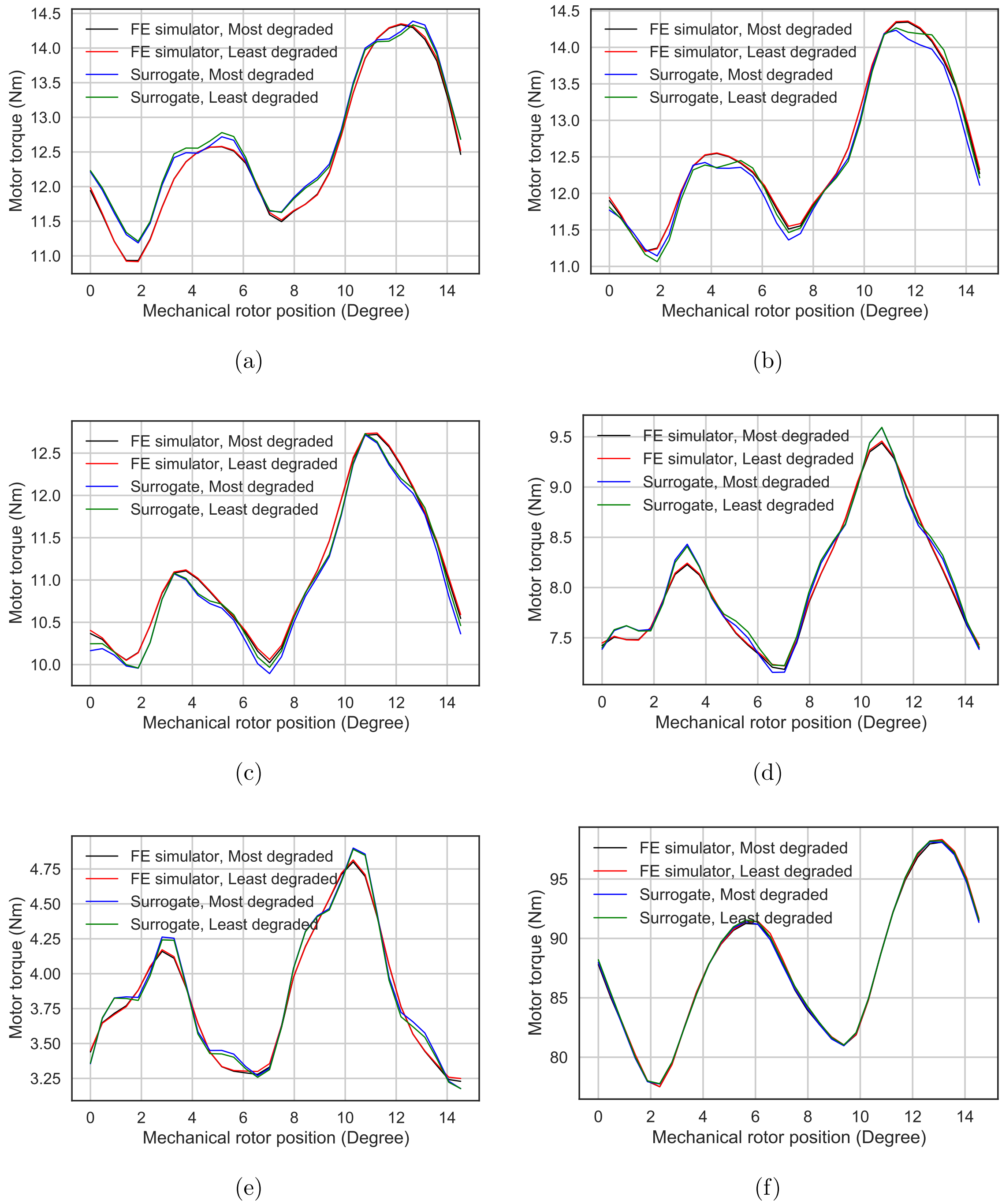

Fig. 5.7.: Torque waveforms corresponding to operating point (a) 1, (b) 2, (c) 3, (d) 4, (e) 5, (f) 6

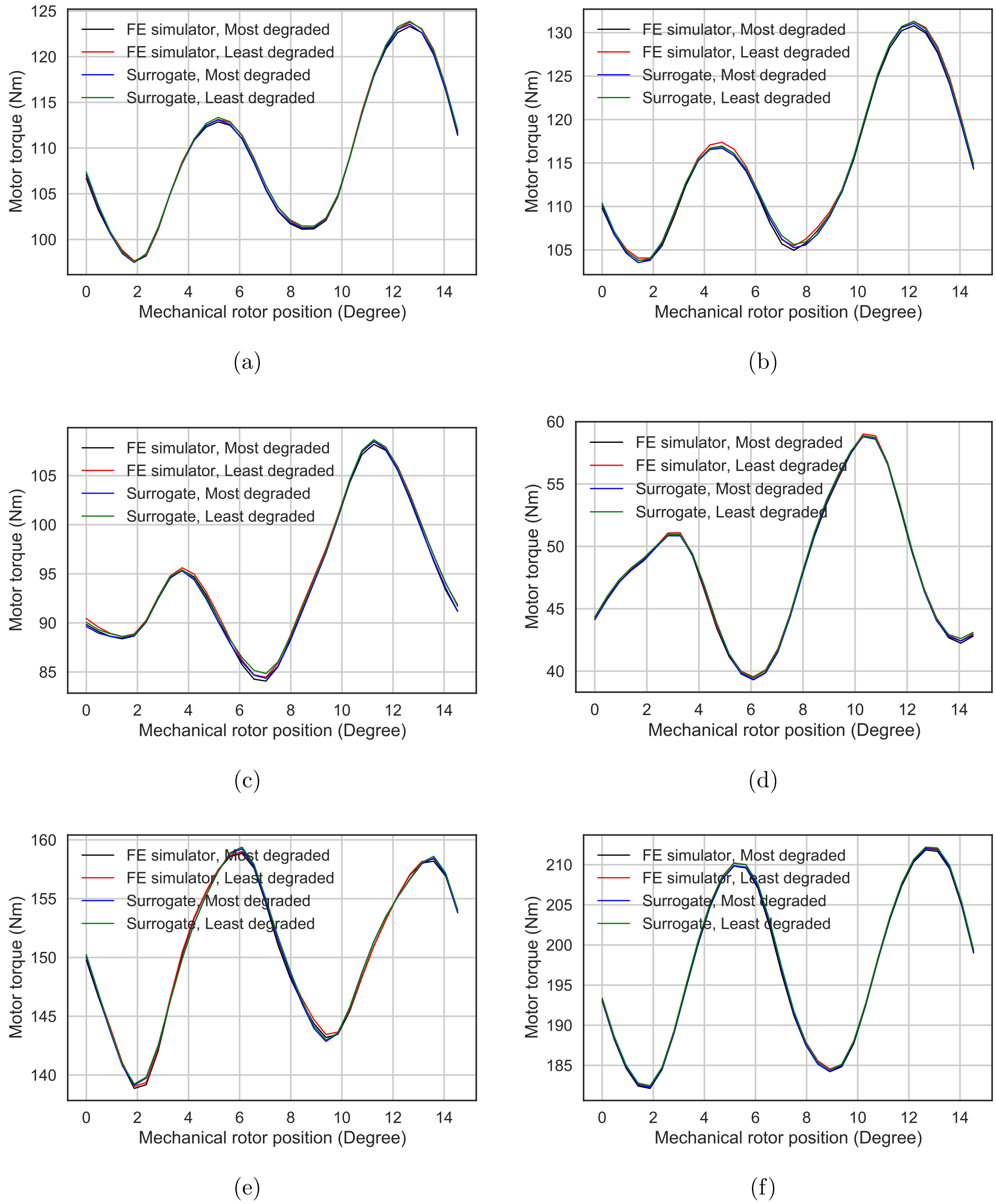

Fig. 5.8.: Torque waveforms corresponding to operating points (a) 7, (b) 8, (c) 9, (d) 10, (e) 11, (f) 12

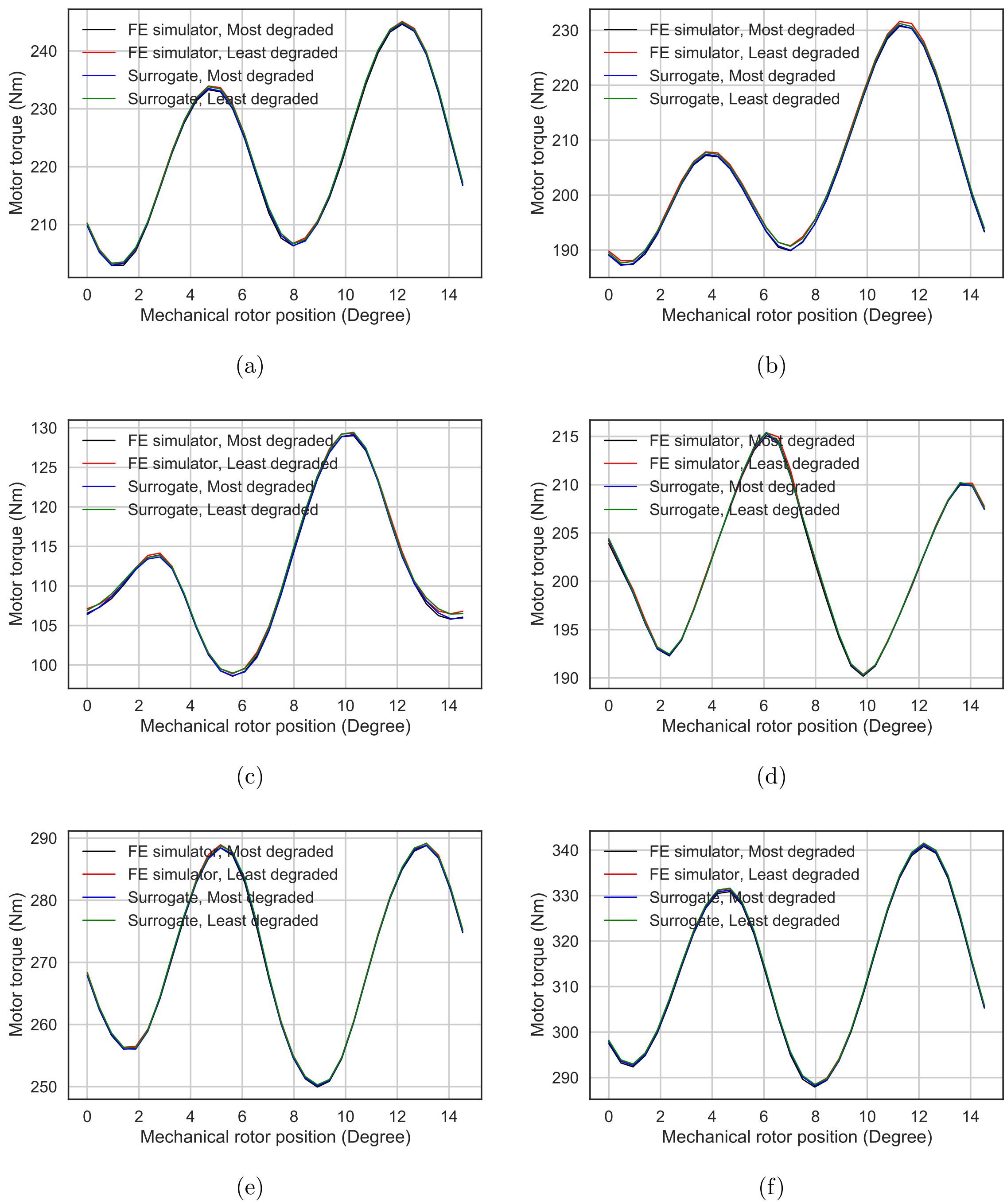

Fig. 5.9.: Torque waveforms corresponding to operating points(a) 13, (b) 14, (c) 15, (d) 16, (e) 17, (f) 18

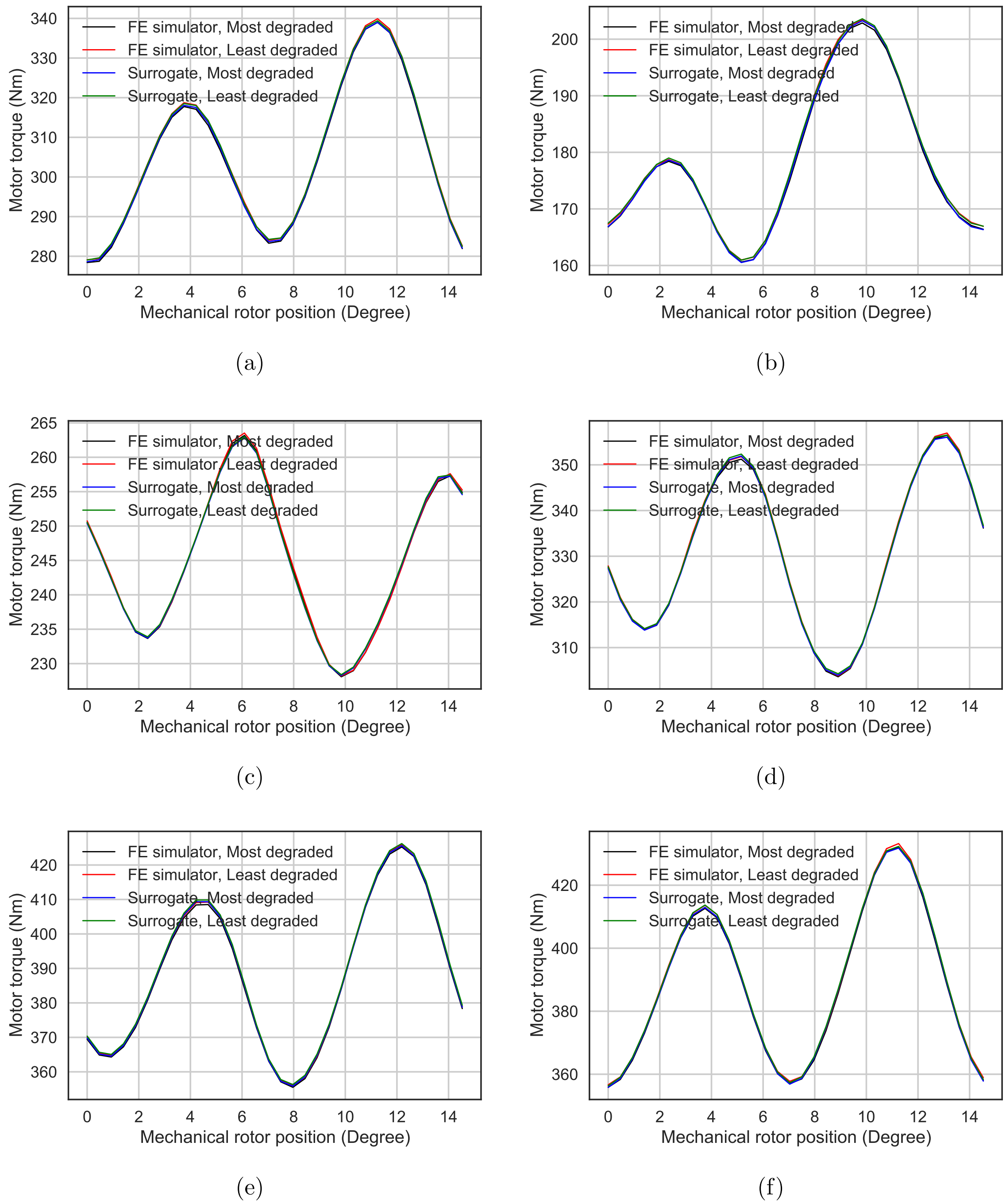

Fig. 5.10.: Torque waveforms corresponding to operating points (a) 19, (b) 20 (c) 21, (d) 22, (e) 23, (f) 24

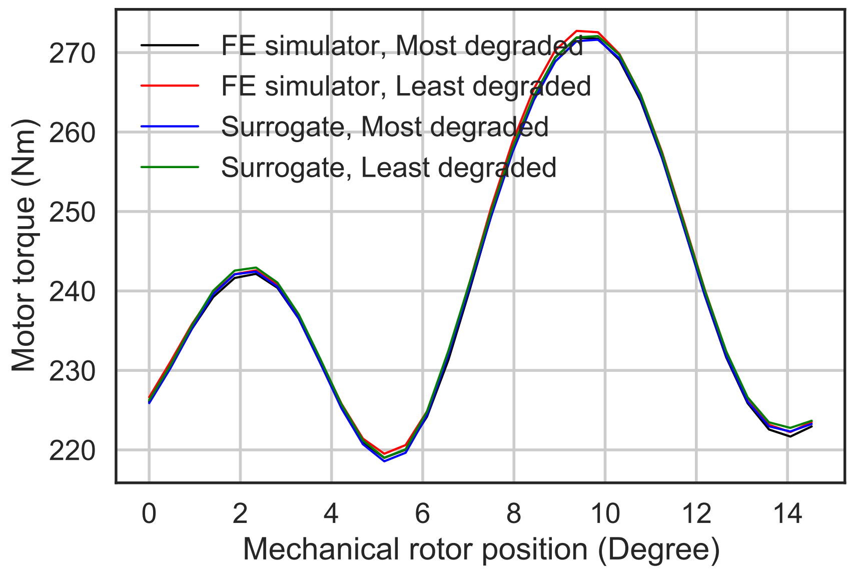

Fig. 5.11.: Torque waveform corresponding to operating point 25

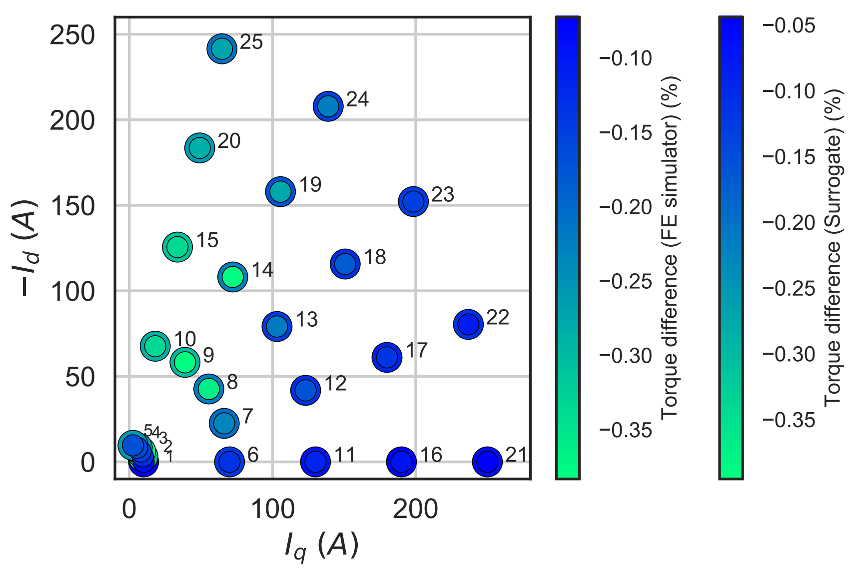

Fig. 5.12.: Difference between the average torque corresponding to the most degraded curve and least degraded curve obtained from (i) FE simulator (ii) surrogate model

Table 5.2.: Difference between the average torque corresponding to the most degraded curve and the least degraded curve

Operating point	**Difference (%) (FE simulator)**	**Difference (%) (Surrogate)**
1	−0.0063	−0.0206
2	−0.0090	−0.0505
3	−0.0096	−0.0798
4	−0.0079	−0.0515
5	−0.0041	−0.0311
6	−0.2722	−0.2766
7	−0.4267	−0.4649
8	−0.3855	−0.4070
9	−0.2489	−0.2443
10	−0.1159	−0.1239
11	−0.6863	−0.6755
12	−1.1569	−1.1707
13	−1.3265	−1.3645
14	−0.8506	−0.9292
15	−0.3327	−0.3085
16	−0.8139	−0.8041
17	−1.4815	−1.5519
18	−2.0381	−2.1226
19	−1.6888	−1.7310
20	−0.6485	−0.5556
21	−0.7586	−0.6403
22	−1.4525	−1.4200
23	−2.3088	−2.2841
24	−2.5067	−2.5381
25	−1.0255	−1.0898

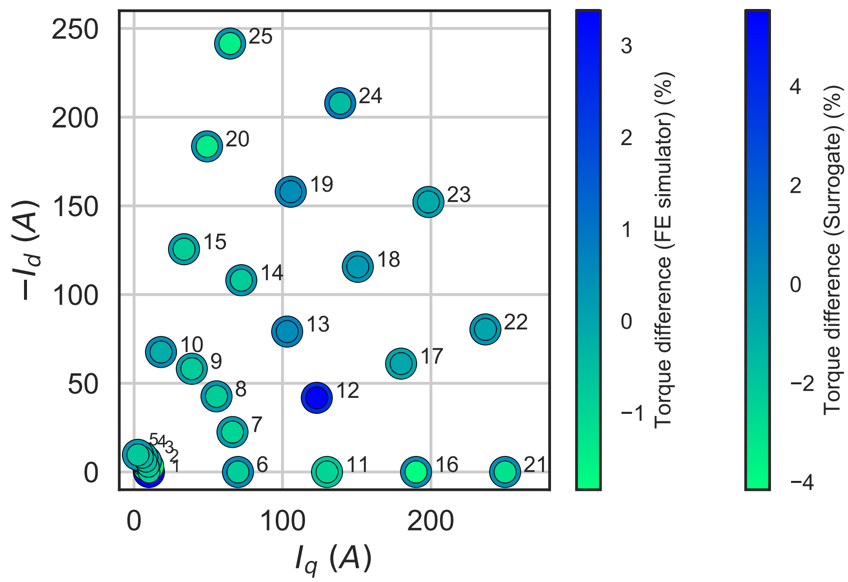

Fig. 5.13.: Difference between the sixth harmonic component of torque corresponding to the most degraded curve and least degraded curve obtained from (i) FE simulator (ii) surrogate model

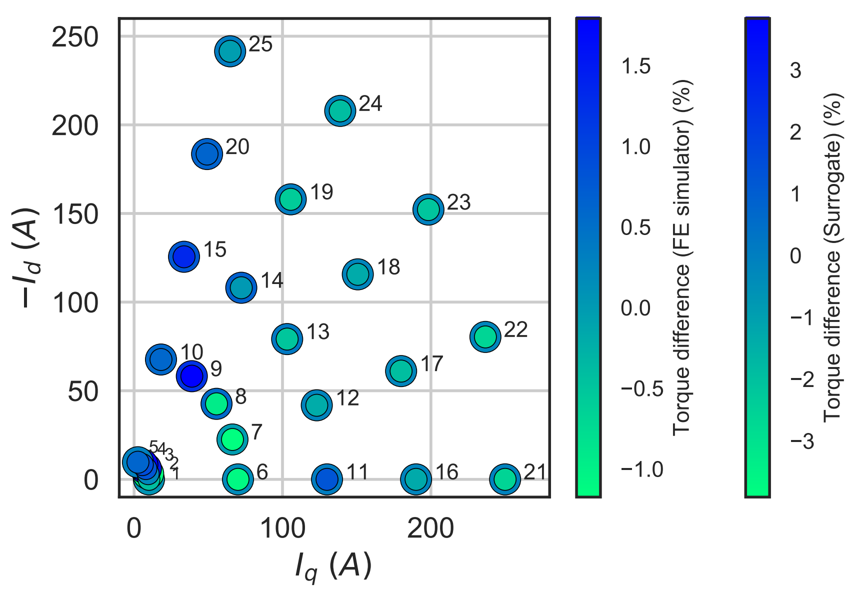

Fig. 5.14.: Difference between the twelfth harmonic component of torque corresponding to the most degraded curve and least degraded curve obtained from (i) FE simulator (ii) surrogate model

Table 5.3.: Difference between the sixth harmonic component of torque corresponding to the most degraded curve and the least degraded curve

Operating point	**Difference (%) (FE simulator)**	**Difference (%) (Surrogate)**
1	0.0028	0.0410
2	0.0023	0.0233
3	0.0017	0.0004
4	0.0012	0.0202
5	0.0013	0.0019
6	−0.0001	−0.0192
7	0.0011	0.0080
8	0.0009	−0.0151
9	−0.0176	−0.0372
10	0.0043	0.0073
11	0.0831	0.0717
12	0.0140	0.0229
13	0.0745	0.1004
14	0.0093	0.0076
15	−0.0098	−0.0175
16	0.1304	0.0931
17	−0.1635	−0.1724
18	−0.1446	−0.1591
19	0.1544	0.2062
20	−0.0182	−0.0309
21	0.1460	0.0442
22	−0.0885	−0.1040
23	−0.2198	−0.2469
24	−0.0088	0.0442
25	0.0434	0.0332

Table 5.4.: Difference between the twelfth harmonic component of torque corresponding to the most degraded curve and least degraded curve

Operating point	**Difference (%) (FE simulator)**	**Difference (%) (Surrogate)**
1	−0.3749	−0.6691
2	0.2087	−3.9079
3	0.7303	3.2374
4	0.8154	3.8314
5	0.5645	−0.0961
6	−0.9966	−0.3923
7	−1.0678	−0.9392
8	−0.8578	0.5685
9	1.6287	2.3091
10	0.5424	0.6741
11	0.7308	0.0407
12	−0.1889	−0.1778
13	−0.4590	0.1680
14	0.0075	0.8853
15	1.2114	1.1353
16	−0.1624	−0.1763
17	−0.3749	−0.2447
18	−0.1777	−0.2095
19	−0.5304	0.0746
20	0.5698	0.8148
21	−0.6137	−0.1168
22	−0.6197	−0.2337
23	−0.4515	−0.0923
24	−0.3718	−0.2088
25	−0.0369	0.0665

Sensitivity study corresponding to the material uncertainty

We also perform a similar sensitivity study as in the previous section considering only the variation of the B-H curves reflecting material uncertainty. We prepare the study by obtaining two B-H curves by sampling two values from $\mathbf{U}$, B-H_1 and B-H_2. For the regions reflecting punching uncertainty, the B-H curve corresponding to the mean value of the variables in Table 4.1 is selected. All the B-H curves are extrapolated to the saturation value that corresponds to the mean value of $\mathbf{S}$ (variable reflecting uncertainty in saturation flux density). Using these two B-H curves, we observe the percentage difference of QoIs obtained separately from the FE simulator and the surrogate model. The waveforms corresponding to this study are shown in Figs. 5.15, 5.16, 5.17 and 5.18. The corresponding differences of QoIs can be observed in Figs. 5.20, 5.21 and 5.22. The values of these differences are reported in Tables 5.5, 5.6 and 5.7. Since the values in the tables show a significant agreement, it can be claimed that the surrogate is able to predict the changes of QoIs with sufficient accuracy.

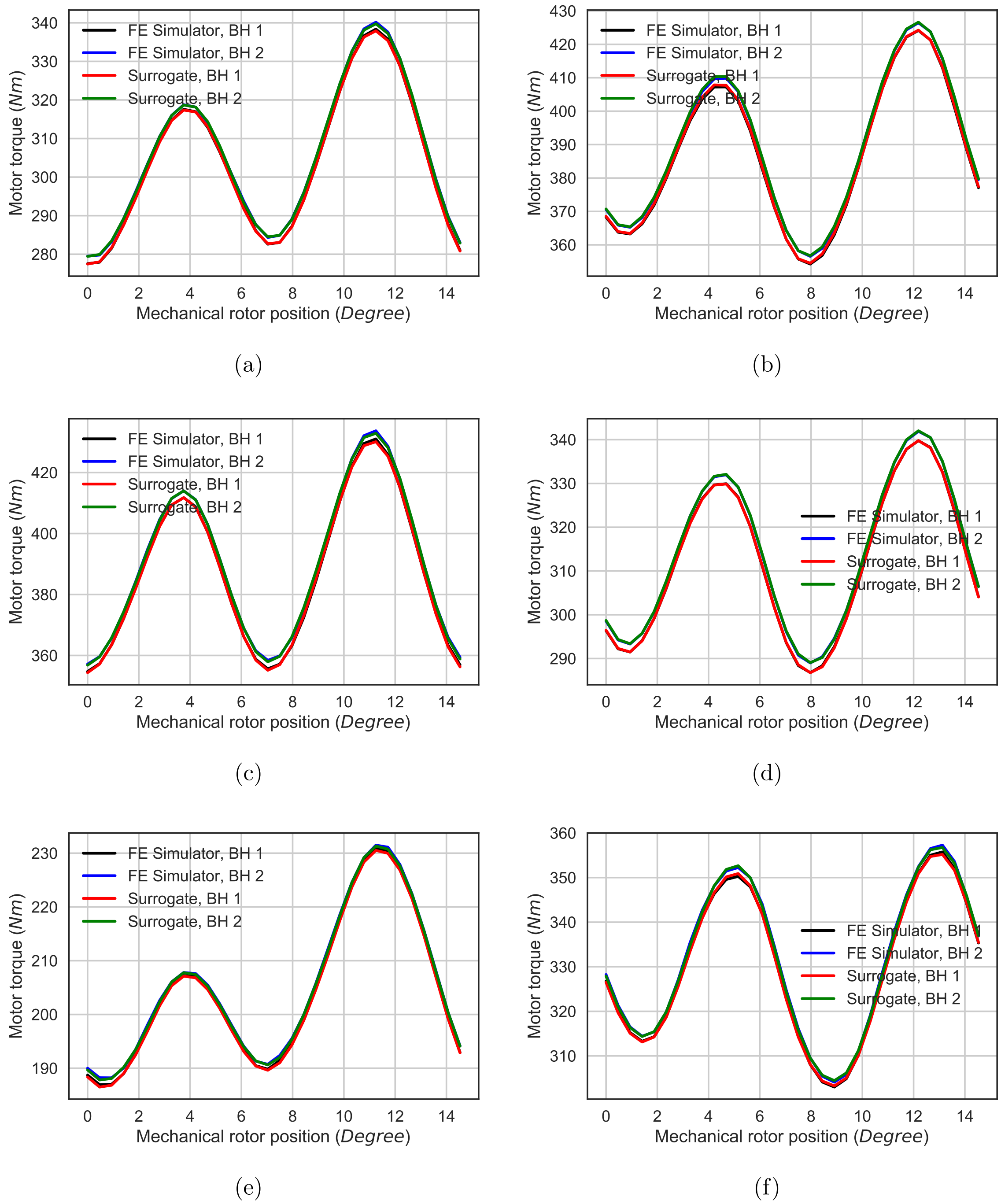

Fig. 5.15.: Torque waveforms corresponding to operating point (a) 1, (b) 2, (c) 3, (d) 4, (e) 5, (f) 6

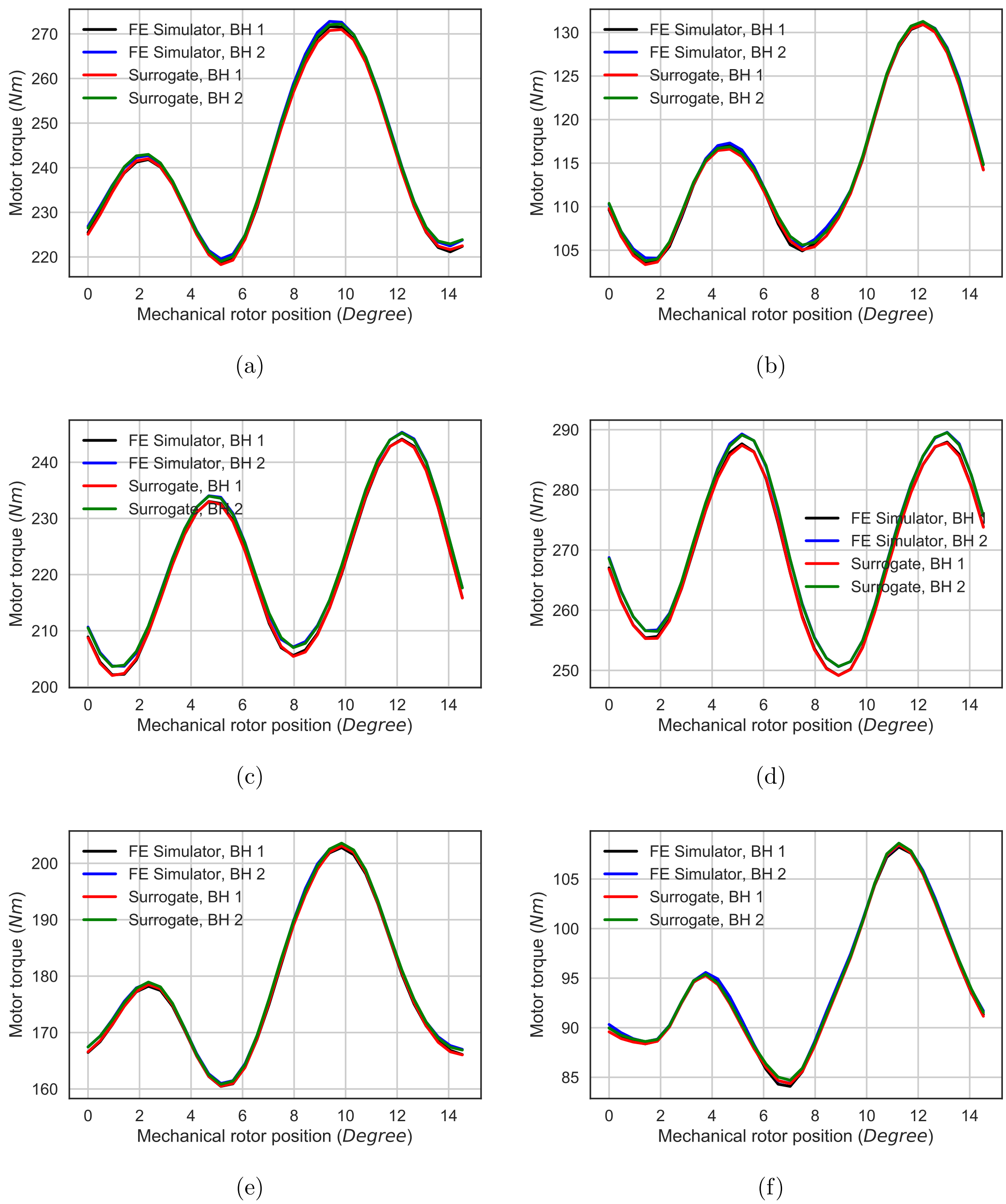

Fig. 5.16.: Torque waveforms corresponding to operating points (a) 7, (b) 8, (c) 9, (d) 10, (e) 11, (f) 12

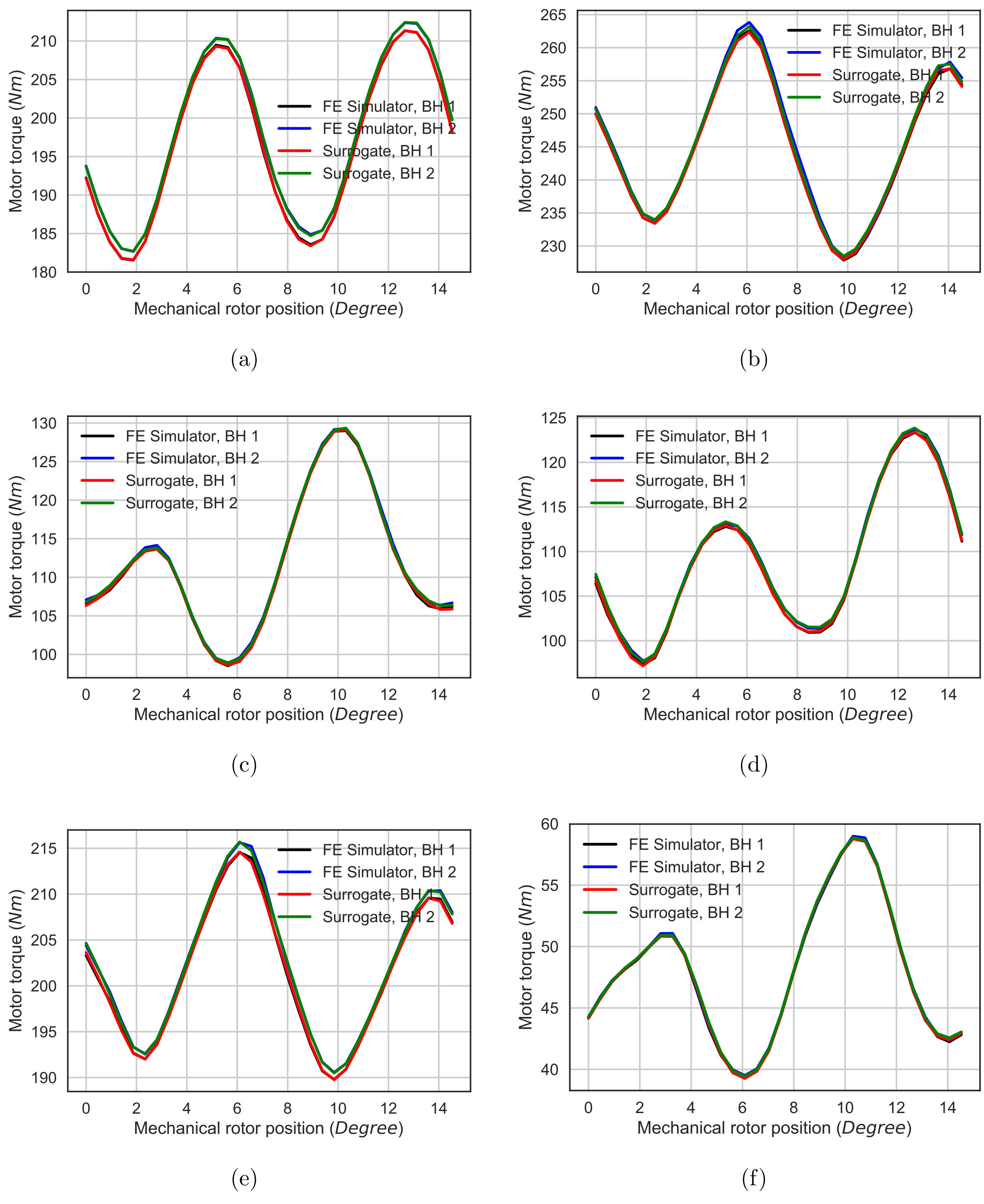

Fig. 5.17.: Torque waveforms corresponding to operating points(a) 13, (b) 14, (c) 15, (d) 16, (e) 17, (f) 18

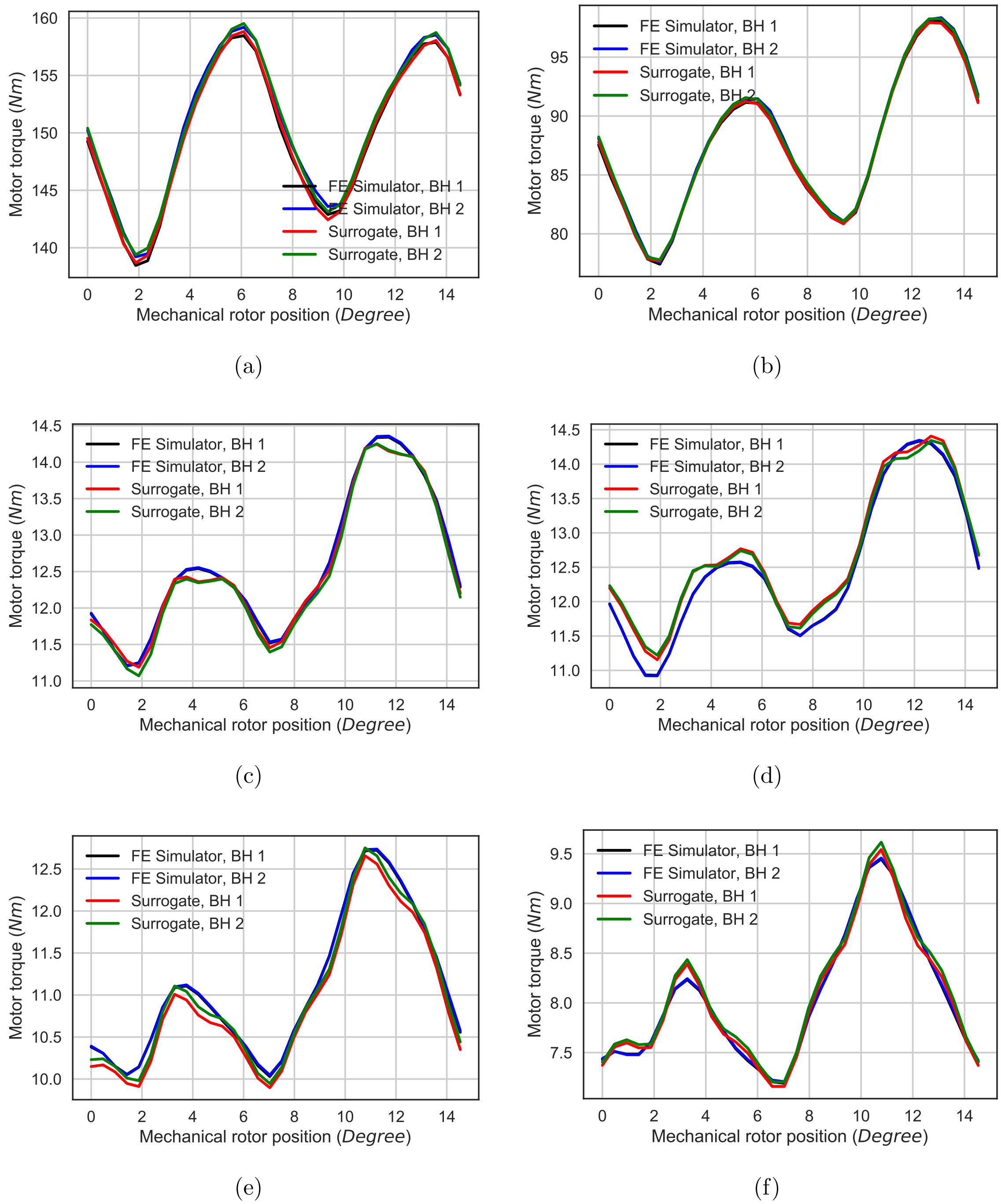

Fig. 5.18.: Torque waveforms corresponding to operating points (a) 19, (b) 20 (c) 21, (d) 22, (e) 23, (f) 24

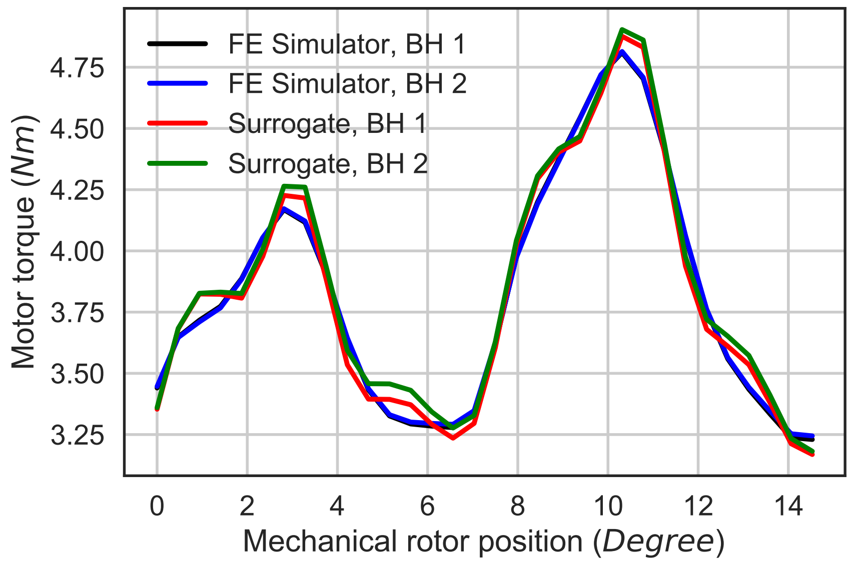

Fig. 5.19.: Torque waveform corresponding to operating point 25

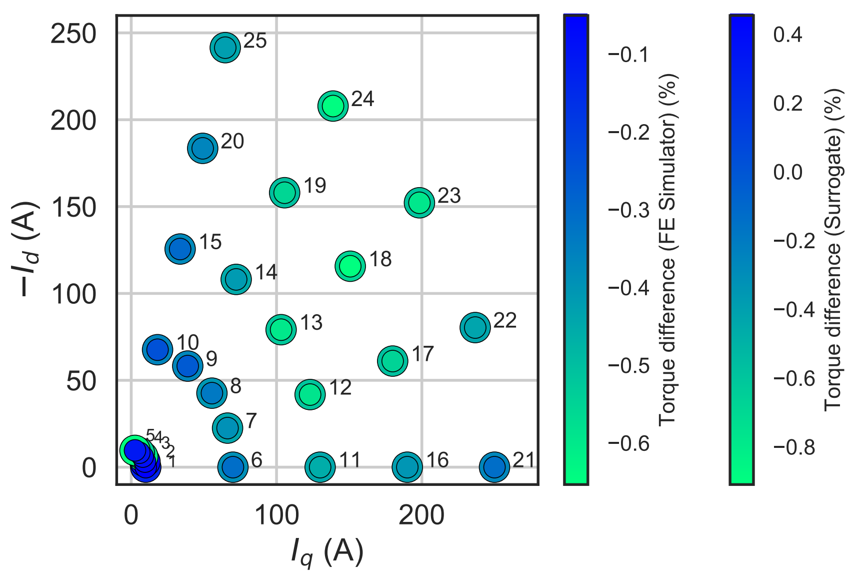

Fig. 5.20.: Difference between the average torque corresponding to B-H_1 and B-H_2 obtained from (i) FE simulator (ii) surrogate model

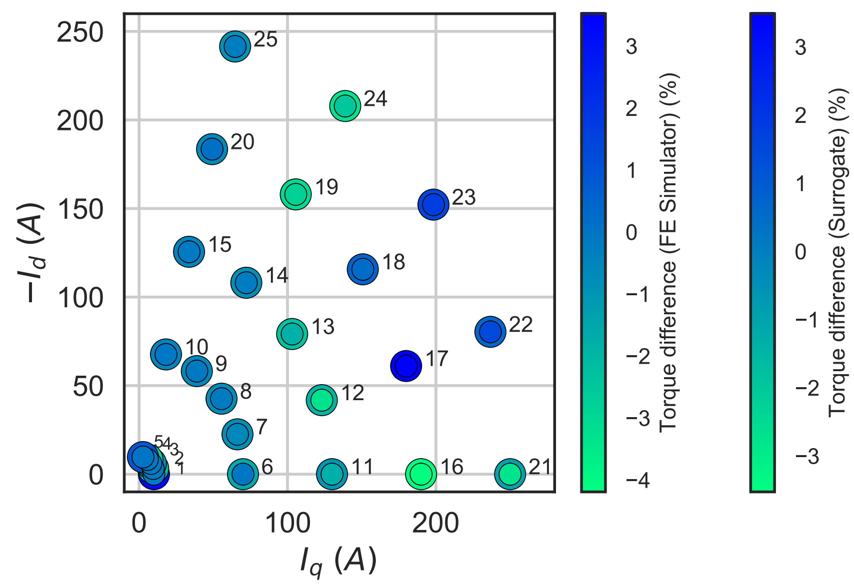

Fig. 5.21.: Difference between the sixth harmonic component of torque corresponding to B-H_1 and B-H_2 obtained from (i) FE simulator (ii) surrogate model

Sensitivity study corresponding to the uncertainty in saturation flux density

We conduct a sensitivity study considering the variation of saturation flux density of the B-H curves as well (as in the previous section). We prepare the study by obtaining two B-H curves for all the regions of the machine (regions reflecting punching uncertainty and material uncertainty) by sampling two values from $\mathbf{S}$, B-H_1 and B-H_2. At these two B-H curves we observe the percentage difference of QoIs obtained separately from the FE simulator and the surrogate model. The waveforms corresponding to this study are shown in Figs. 5.23, 5.24, 5.25 and 5.26. The corresponding differences of QoIs can be observed in Figs. 5.28, 5.29 and 5.30. The values of these differences are reported in Tables 5.8, 5.9 and 5.10. Since the values in the

Table 5.5.: Difference between the average torque corresponding to B-H_1 and B-H_2 obtained from (i) FE simulator (ii) surrogate model

Operating point	**Difference (%) (FE simulator)**	**Difference (%) (Surrogate)**
1	−0.0203	0.427
2	−0.0058	0.0047
3	−0.0281	0.0460
4	−0.0187	0.0396
5	−0.0086	0.0023
6	−0.3973	0.4741
7	−0.2815	0.2905
8	−0.0690	0.1620
9	−0.0942	−0.0840
10	−0.0573	−0.0597
11	−0.4583	0.4409
12	−0.1823	0.2039
13	−0.0313	−0.0104
14	−0.5510	−0.6337
15	−0.4962	−0.4958
16	−0.0723	−0.1533
17	−0.7788	−0.8098
18	−0.8921	−0.8651
19	−1.0609	−1.2376
20	−1.1276	−1.1622
21	−0.8692	−0.6839
22	−2.2383	−2.4845
23	−2.5030	−2.5740
24	−1.9386	−1.8455
25	−1.8239	−1.7101

Table 5.6.: Difference between the sixth harmonic component of torque corresponding to B-H_1 and B-H_2 obtained from (i) FE simulator (ii) surrogate model

Operating point	**Difference (%) (FE simulator)**	**Difference (%) (Surrogate)**
1	0.0128	0.0210
2	−0.0023	−0.0233
3	−0.0017	−0.0004
4	0.0012	0.0202
5	0.0013	0.0019
6	−0.0001	−0.0192
7	−0.0011	−0.0080
8	−0.0009	−0.0151
9	−0.0176	−0.0372
10	−0.0043	−0.0073
11	−1.0831	−1.0717
12	−2.0140	−2.0229
13	−0.0745	−0.1004
14	0.0093	0.0076
15	0.0098	0.0175
16	−4.1304	−3.9321
17	1.1635	1.1724
18	0.1446	0.1591
19	−1.1544	−1.2062
20	−0.0182	−0.0309
21	−1.1460	−1.0442
22	0.0885	0.1040
23	1.198	1.469
24	−2.0088	2.0442
25	−0.0434	−0.0332

Table 5.7.: Difference between the twelfth harmonic component of torque corresponding to B-H_1 and B-H_2 obtained from (i) FE simulator (ii) surrogate model

Operating point	**Difference (%) (FE simulator)**	**Difference (%) (Surrogate)**
1	-0.0049	0.0162
2	-0.0038	-0.0202
3	-4.1015	-4.2093
4	0.0012	-0.0049
5	0.0028	0.0023
6	-0.0138	-0.0321
7	0.0237	0.0202
8	0.0479	0.0467
9	0.0332	0.0528
10	0.0168	0.0236
11	0.0338	0.0219
12	0.0610	0.0442
13	0.1009	0.1115
14	0.1306	0.1210
15	0.0486	0.0495
16	-0.0599	-0.0722
17	-0.0817	-0.0812
18	-0.0112	-0.0243
19	0.0984	0.0956
20	0.0151	0.0292
21	-1.2646	-1.3666
22	-0.3560	-0.3083
23	-0.6520	-0.8486
24	0.0258	0.0268
25	-0.0093	-0.0493

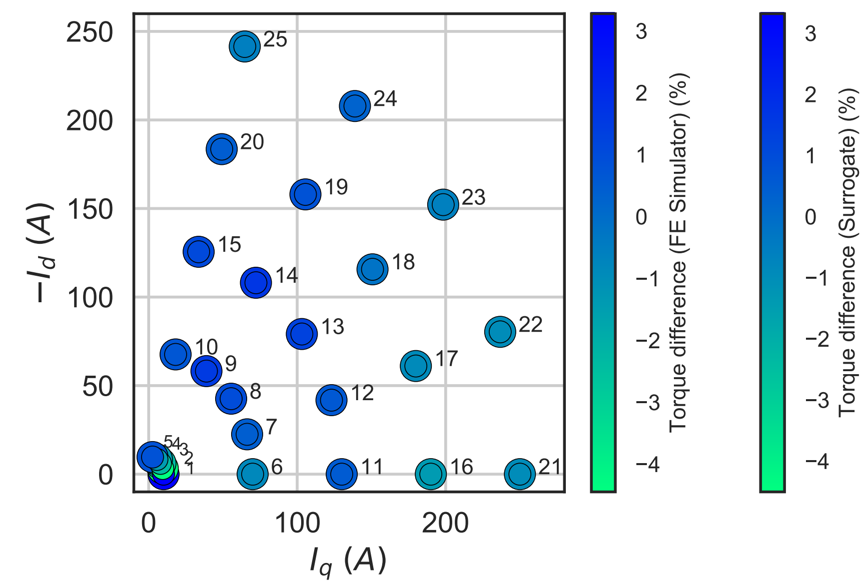

Fig. 5.22.: Difference between the twelfth harmonic component of torque corresponding to B-H_1 and B-H_2 obtained from (i) FE simulator (ii) surrogate model

tables show a significant agreement, it can be claimed that the surrogate is able to predict the changes of QoIs with sufficient accuracy.

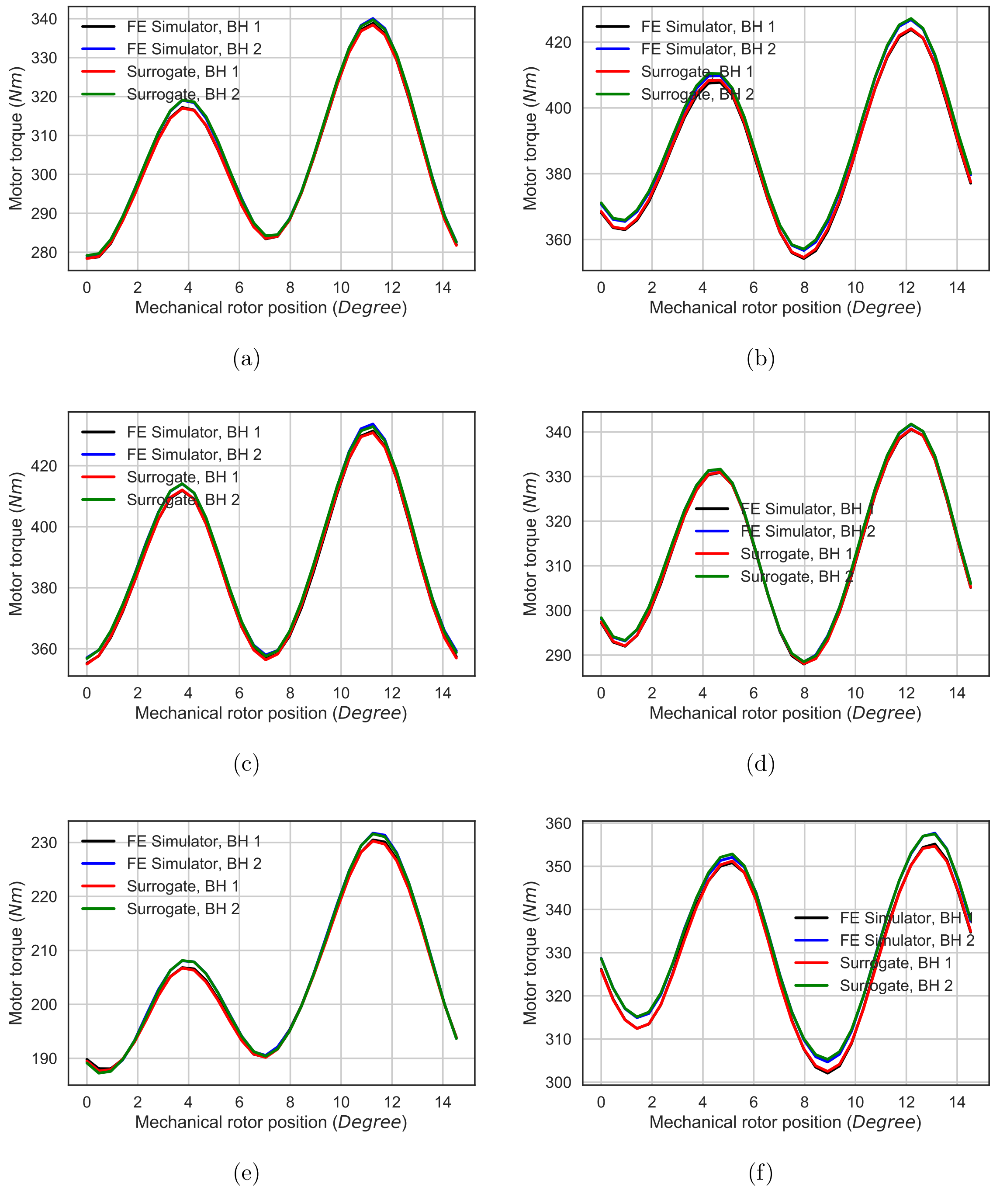

Fig. 5.23.: Torque waveforms corresponding to operating point (a) 1, (b) 2, (c) 3, (d) 4, (e) 5, (f) 6

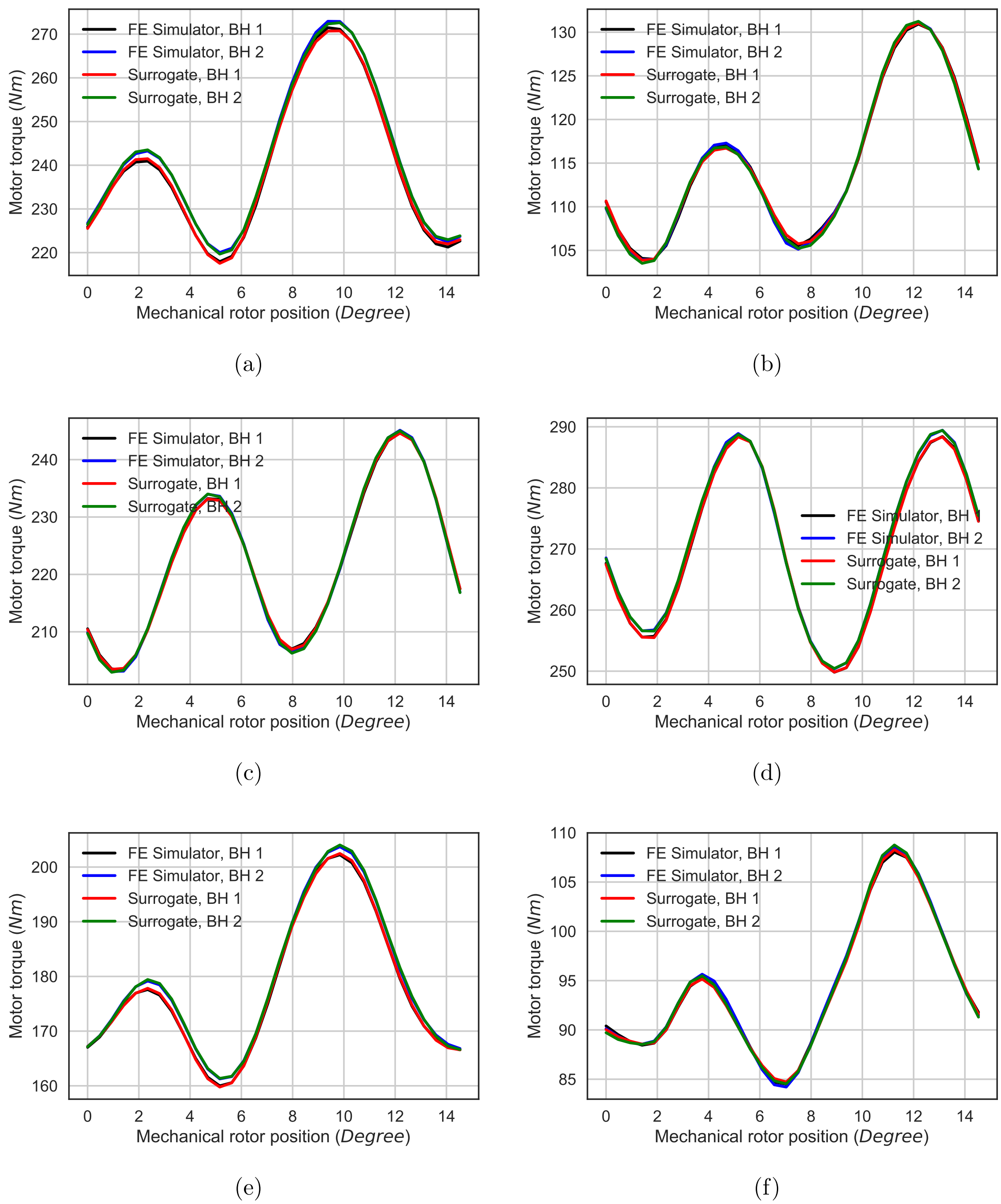

Fig. 5.24.: Torque waveforms corresponding to operating points (a) 7, (b) 8, (c) 9, (d) 10, (e) 11, (f) 12

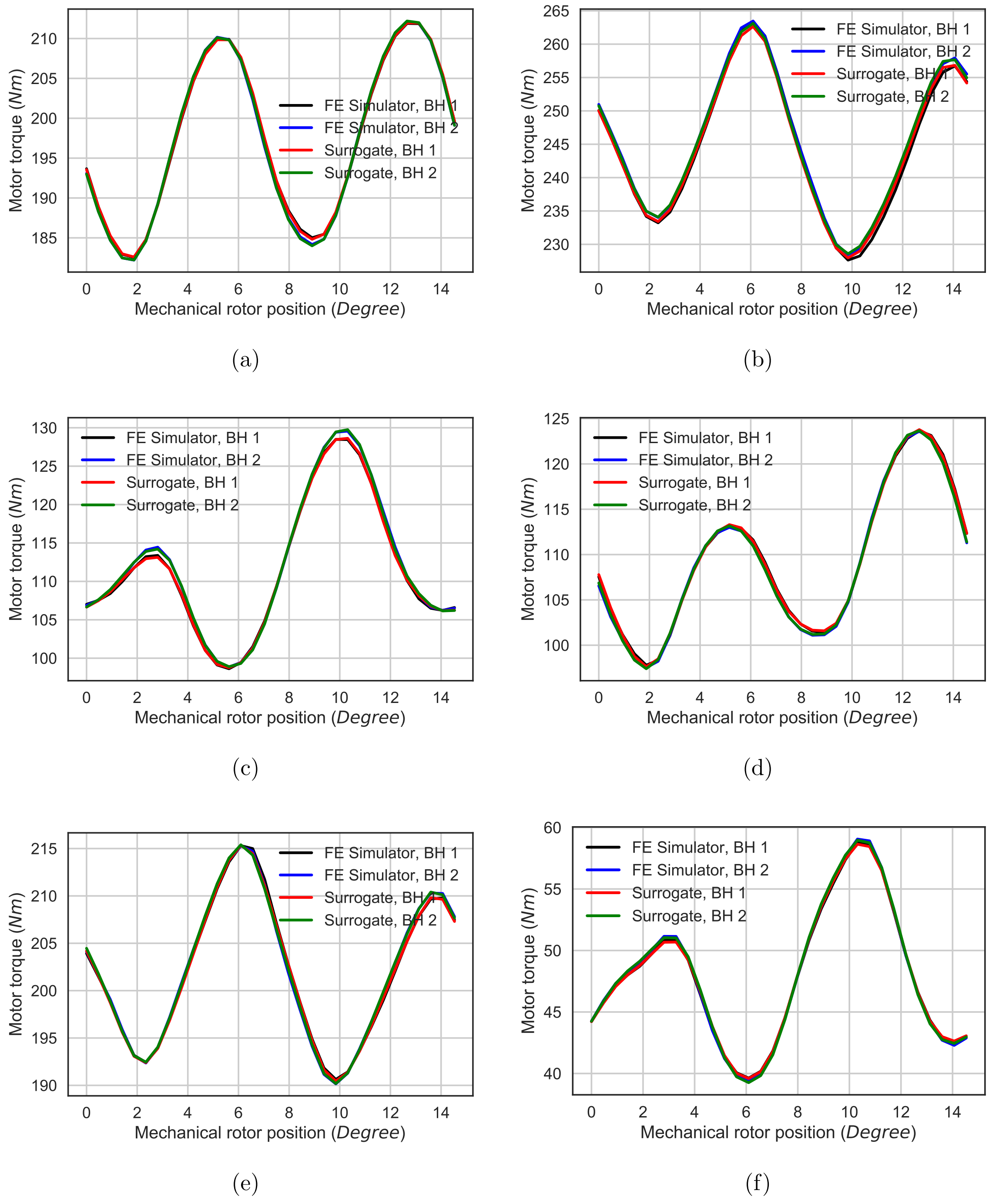

Fig. 5.25.: Torque waveforms corresponding to operating points(a) 13, (b) 14, (c) 15, (d) 16, (e) 17, (f) 18

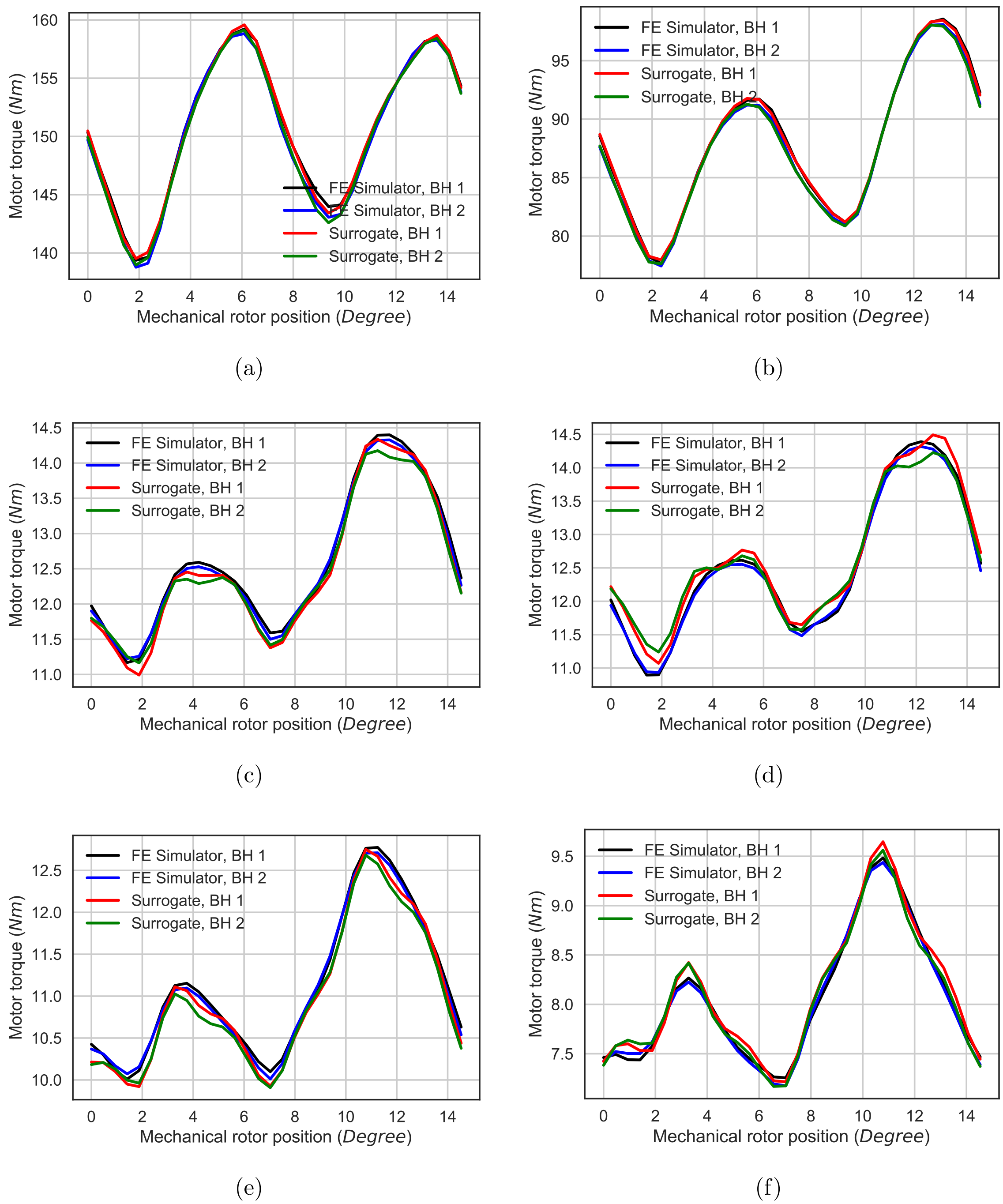

Fig. 5.26.: Torque waveforms corresponding to operating points (a) 19, (b) 20 (c) 21, (d) 22, (e) 23, (f) 24

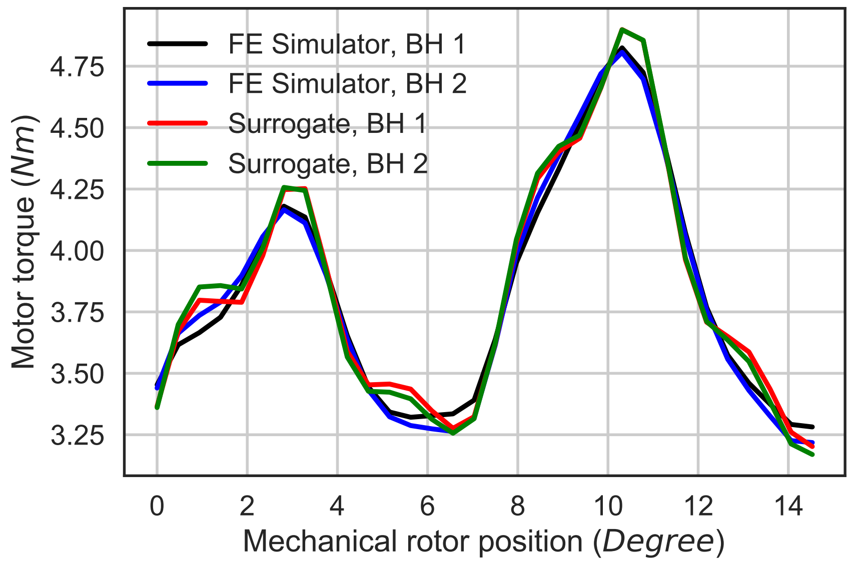

Fig. 5.27.: Torque waveform corresponding to operating point 25

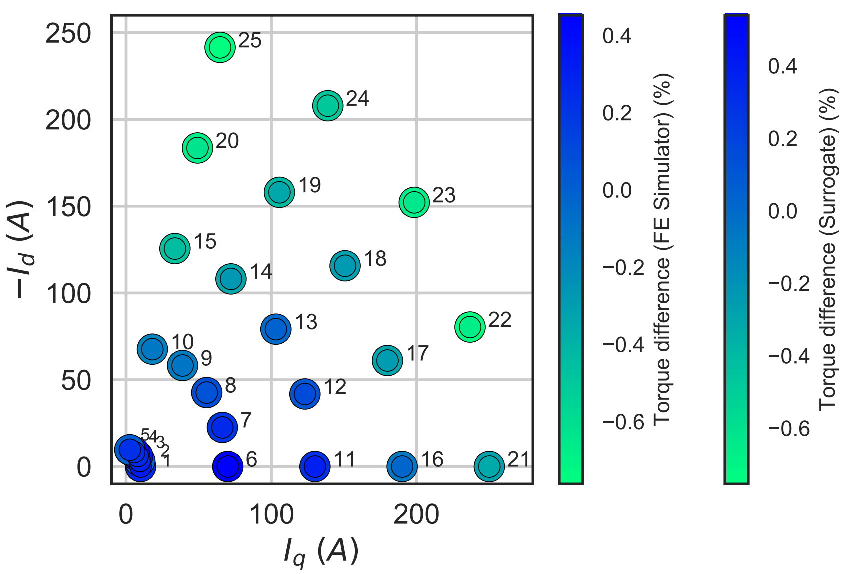

Fig. 5.28.: Difference between the average torque corresponding to B-H_1 and B-H_2 obtained from (i) FE simulator (ii) surrogate model

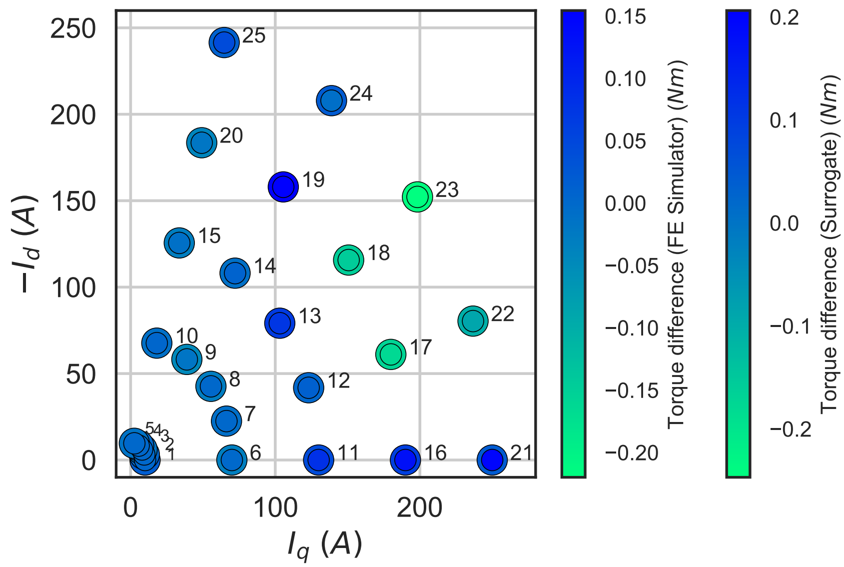

Fig. 5.29.: Difference between the sixth harmonic component of torque corresponding to B-H_1 and B-H_2 obtained from (i) FE simulator (ii) surrogate model

5.3 Development of surrogate models for predicting average torque and average flux linkages of the PMSM

This section is a part of the extended work. Our goal in the extended work is to study the effect of uncertainty in B-H curves and remanent flux density of permanent magnets on performance of the machine/drive system. For performing this study, we assume that all the degraded zones follow the same B-H characteristics dictated by $\mathbf{Z}_h$. Physically, it means that the punching tool corresponding to each cutting edge of the stator and rotor reflects the same state. Thus, we parameterize the FE simulator by the operating points and the uncertain parameters, given by $\mathbf{Z}_h$, $\mathbf{U}$, $\mathbf{S}$ and $\mathbf{B}_r$. The operating points in the defined range can be obtained by varying $\mathbf{I}_{\text{pk}}$, the amplitude of the current and $\mathbf{\Phi}_c$, the current angle (see Fig. 5.1) uniformly. Thus, these parameters constitute a 6-D parameter space reported in Table 5.11.

Table 5.8.: Difference between the average torque corresponding to B-H_1 and B-H_2 obtained from (i) FE simulator (ii) surrogate model

Operating point	**Difference (%) (FE simulator)**	**Difference (%) (Surrogate)**
1	0.0406	0.0427
2	0.0358	0.0047
3	0.0281	0.0460
4	0.0187	0.0396
5	0.0086	0.0023
6	0.3973	0.4741
7	0.2815	0.2905
8	0.0690	0.1620
9	-0.0942	-0.0840
10	-0.0573	-0.0597
11	0.4583	0.4409
12	0.1823	0.2039
13	-0.0313	-0.0104
14	-0.5510	-0.6337
15	-0.4962	-0.4958
16	-0.0723	-0.1533
17	-0.7788	-0.8098
18	-0.8921	-0.8651
19	-1.0609	-1.2376
20	-1.1276	-1.1622
21	-0.8692	-0.6839
22	-2.2383	-2.4845
23	-2.5030	-2.5740
24	-1.9386	-1.8455
25	-1.8239	-1.7101

Table 5.9.: Difference between the sixth harmonic component of torque corresponding to B-H_1 and B-H_2 obtained from (i) FE simulator (ii) surrogate model

Operating point	**Difference (%) (FE simulator)**	**Difference (%) (Surrogate)**
1	0.0028	0.0410
2	0.0023	0.0233
3	0.0017	0.0004
4	0.0012	0.0202
5	0.0013	0.0019
6	−0.0001	−0.0192
7	0.0011	0.0080
8	0.0009	−0.0151
9	−0.0176	−0.0372
10	0.0043	0.0073
11	0.0831	0.0717
12	0.0140	0.0229
13	0.0745	0.1004
14	0.0093	0.0076
15	−0.0098	−0.0175
16	0.1304	0.0931
17	−0.1635	−0.1724
18	−0.1446	−0.1591
19	0.1544	0.2062
20	−0.0182	−0.0309
21	0.1460	0.0442
22	−0.0885	−0.1040
23	−0.2198	−0.2469
24	−0.0088	0.0442
25	0.0434	0.0332

Table 5.10.: Difference between the twelfth harmonic component of torque corresponding to B-H_1 and B-H_2 obtained from (i) FE simulator (ii) surrogate model

Operating point	**Difference (%) (FE simulator)**	**Difference (%) (Surrogate)**
1	-0.0049	0.0162
2	-0.0038	-0.0202
3	-0.0015	-0.0093
4	0.0012	-0.0049
5	0.0028	0.0023
6	-0.0138	-0.0321
7	0.0237	0.0202
8	0.0479	0.0467
9	0.0332	0.0528
10	0.0168	0.0236
11	0.0338	0.0219
12	0.0610	0.0442
13	0.1009	0.1115
14	0.1306	0.1210
15	0.0486	0.0495
16	-0.0599	-0.0722
17	-0.0817	-0.0812
18	-0.0112	-0.0243
19	0.0984	0.0956
20	0.0151	0.0292
21	-0.1646	-0.0666
22	-0.1560	-0.1083
23	-0.0650	-0.0887
24	0.0458	0.0468
25	-0.0093	-0.0493

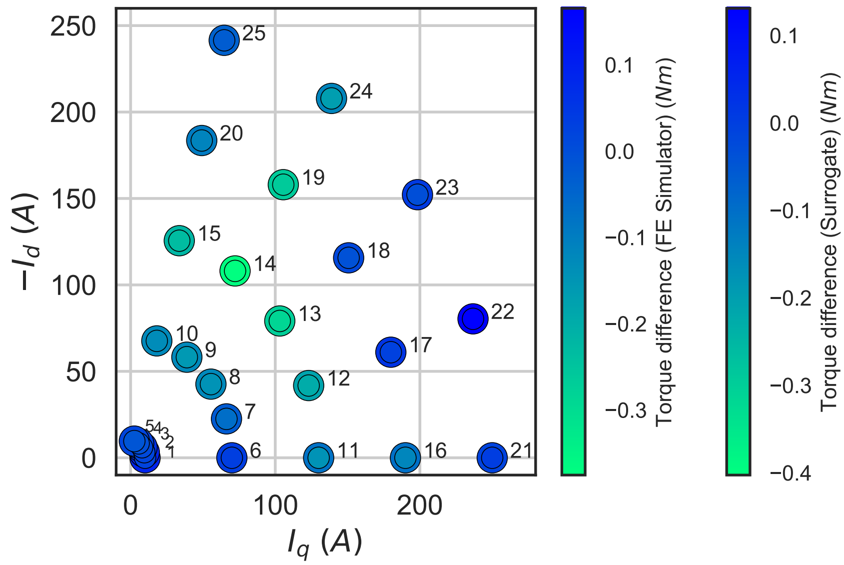

Fig. 5.30.: Difference between the twelfth harmonic component of torque corresponding to B-H_1 and B-H_2 obtained from (i) FE simulator (ii) surrogate model

The study of the performance of the machine/drive system hinges on the evaluation of average torque, $\bar{T}$, and the minimum DC-link voltage, V_{min}, of the inverter required to drive the machine. The minimum DC-link voltage, V_{min}, is given by

$$V_{\mathrm{min}} = \sqrt{V_{\mathrm{qs}}^2 + V_{\mathrm{qs}}^2}\sqrt{3} \tag{5.36}$$

where

$$V_{\mathrm{qs}} = r_s I_{\mathrm{q}} + \omega_r \Lambda_{\mathrm{ds}}, \tag{5.37}$$

$$V_{\mathrm{ds}} = r_s I_{\mathrm{d}} - \omega_r \Lambda_{\mathrm{qs}}, \tag{5.38}$$

where r_s is the resistance of each phase of the stator winding in PMSM, ω_r is the rotor speed, I_{q}, I_{d} are the q- and d- axes stator currents respectively and Λ_{qs}, Λ_{ds} are the q- and d- axes average flux linkages referred to the stator respectively. The evaluation of V_{min} requires the calculation of Λ_{qs} and Λ_{ds} from the FE simulator. Hence, $\bar{T}$, Λ_{qs} and Λ_{ds} of the machine are our quantities of interest (QoIs) that we have to evaluate using the FE simulator under the considered uncertainties. Note that the

QoIs of the extended work is different from the original work. However, evaluations using FE simulator is computationally expensive. Thus, we develop 3 inexpensive surrogate models that evaluate our QoIs, $\bar{T}$, Λ_{qs} and Λ_{ds} with the parameters of the FE simulator as the input. To obtain the average values of torque and flux linkages from their corresponding waveforms, *Simpson's* rule is employed.

The procedure of obtaining input-output observations for constructing the surrogate models for the QoIs is identical to the procedure followed in Section 5. Given a total of N training samples are obtained, the entire training input data set is given by $\mathbf{X} = \left(\mathbf{x}^{(1)}, \ldots, \mathbf{x}^{(N)}\right) \in \mathbb{R}^{6\times N}$. In practice, for a separate validation set, we predict the QoIs using the trained surrogates and compare the prediction against the actual QoIs obtained from the FE simulator. N is iteratively increased till the decided error criteria between the QoIs is within a satisfactory tolerance.

We construct the surrogate models for the QoIs using Gaussian process (GP) regression. Each QoI is learned by a scalar GP function, f. The procedure of construction of the surrogate model for each QoI is the same as that of the procedure used to construct the surrogate model that predicts an individual PC in the previous section. Thus, interested readers are requested to refer to Section 5 for details on the construction of the model.

5.3.1 Validation of the surrogate model

The accuracy of the trained surrogate model is tested on a separate set of inputs called the validation set. Let the validation input set be $\mathbf{X}_v = \left(\mathbf{x}_v^{(1)}, \ldots, \mathbf{x}_v^{(P)}\right) \in \mathbb{R}^{6\times P}$ that contains P samples from the parameter space obtained using LHS. At these inputs points, let $\mathbf{q}_v = \left(q_v^{(1)}, \ldots, q_v^{(P)}\right) \in \mathbb{R}^P$ be the predictive mean of QoIs from the surrogate model at $\mathbf{X}_v$.

Additionally, the QoIs are independently calculated from the FE simulator at these P validation inputs. Let the QoIs obtained from the FE simulator be called the actual QoIs, $\mathbf{q}_a \in \mathbb{R}^P$. The error criteria used in this study to evaluate the convergence of the model is the relative L_2 norm of the error between the actual QoIs and the predicted QoIs, where the relative L_2 norm of the error is given by

$$\text{relative } L_2\text{-norm error} = \frac{||\mathbf{q}_v - \mathbf{q}_a||_2}{||\mathbf{q}_v||_2}. \tag{5.39}$$

The training samples, N, are increased iteratively until the convergence is reached.

Table 5.11.: Input parameters for the surrogate models

Parameter	Lower bound	Upper bound	Mean
$\mathbf{I}_{\text{pk}}$ (A)	0	300	150
$\mathbf{\Phi}_c$ (deg)	0	90	45
$\mathbf{Z}_h$ ()	-2.1624	2.772	0.3052
$\mathbf{U}$()	-1	1	0
$\mathbf{S}$ (T)	1.94	2.06	2
$\mathbf{B}_r$ (T)	1.1931	1.26691	1.23

5.3.2 Assessment of the Surrogate Model

In this section, we assess the 3 surrogate models used to predict $\bar{T}$, Λ_{qs} and Λ_{ds}. Each surrogate is trained with $N = 600$ input points and validated with an additional $P = 150$ points. It should be noted that the training and validation points for all the 3 surrogate models are the same. Initially, we start with $N = 50$ training points and iteratively increase it till the convergence of the relative L_2-norm error is reached. We evaluate the relative L_2-norm error with increasing training points to observe its convergence for each surrogate model. The convergence of the relative L_2-norm error for each surrogate is illustrated in Fig. 5.31. It can be observed that after 450 training points, with further increase in number of training points the relative L_2-norm error doesn't go down significantly i.e. the change in relative L_2-norm is less than 10^{-2}.

Thus, the error is said to have converged. Additionally, we also illustrate the error between the actual QoIs from the FE simulator and predicted QoIs from the 3 trained surrogate models (with 600 training points) at the validation points in Fig. 5.32. It can be observed the error is negligible especially at the operating region of the PMSM i.e. at high torque and current regions.

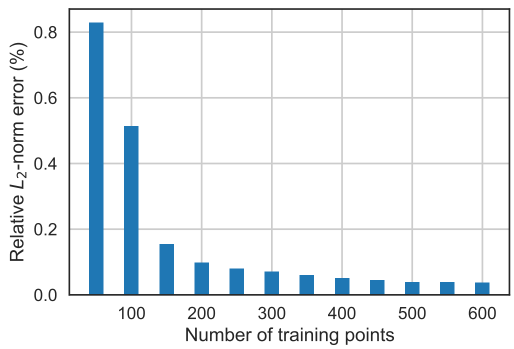

(a)

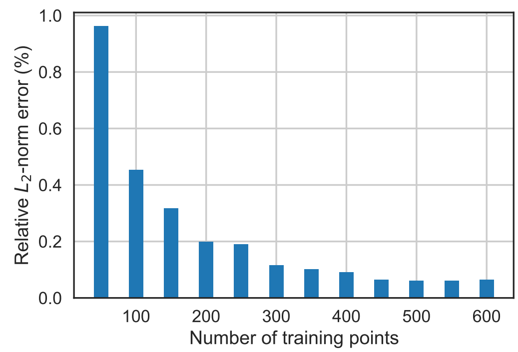

(b)

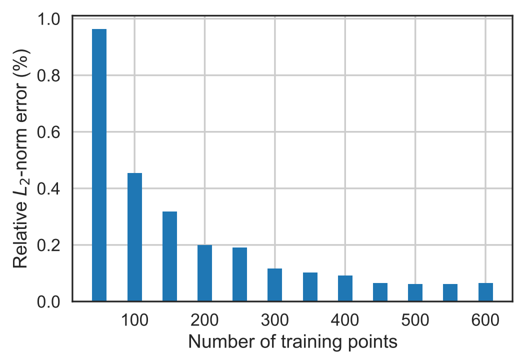

(c)

Fig. 5.31.: Convergence of the relative L_2-norm error of the surrogate models corresponding to (a) $\bar{T}$, (b) Λ_{qs} and (c) Λ_{ds}

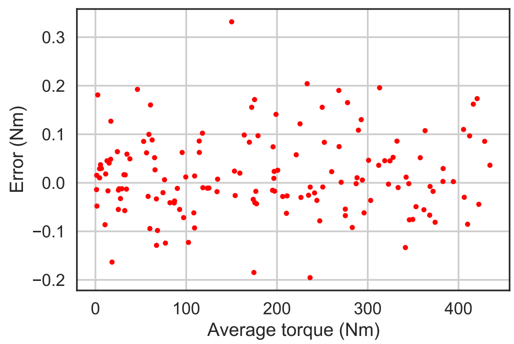

(a)

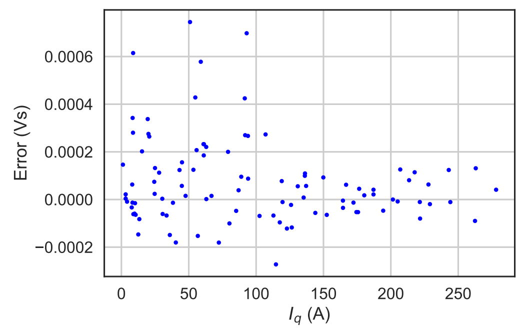

(b)

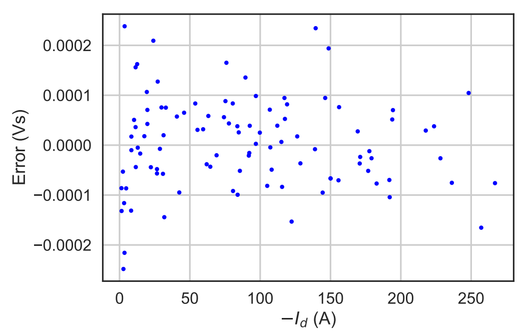

(c)

Fig. 5.32.: Error in prediction by the trained surrogate models corresponding to (a) $\bar{T}$, (b) Λ_{qs} and (c) Λ_{ds} at the validation points

6. PROPAGATION OF UNCERTAINTY IN B-H CURVES TO THE TORQUE PROFILE OF THE PMSM

In this chapter, we consider two case studies where we assess the effect of B-H uncertainties on the average torque and torque ripple profiles (the quantities of interest (QoIs)) of the permanent magnet synchronous machine (PMSM). The first section of this chapter illustrates case study 1 where we consider the effect of variation of all the parameters representing B-H uncertainties on the QoIs and Section 6.2 illustrates case study 2 we consider the effect of wearing of punching tool on the QoIs.

6.1 Case study 1

The evaluation of the trained surrogate is computationally inexpensive. Hence, the torque response can be evaluated at hundreds of random samples from the input space. We consider two operating points; operating point, A, given by $I_{\text{pk}} = 250$ A, $\phi_c = 45$ deg ($I_q = 176.77$ A, $I_d = -176.77$ A) and operating point, B, given by $I_{\text{pk}} = 150$, $\phi_c = 60$ deg ($I_q = 75$ A, $I_d = -129.903$ A). At these points, we want to observe the effect of parametric and epistemic uncertainty on the QoIs. To this end, we consider the B-H uncertainties through 1000 random samples from the 7-D space defined by the distributions in rows $3 - 9$ in Table 5.1. Thereafter, we obtain 1000 evaluations of the torque response from the surrogate at these 1000 input samples for both the operating points. These 1000 evaluations give rise to 1000 probability density functions (PDFs) of the mean torque, sixth and twelfth harmonic components of torque. From these PDFs, we obtain the mean and 95% error bars. These error bars arise due to the limited amount of training data used in training the surrogate. The Figs. 6.1 and 6.4 show the variation of the average torque with the variation of the input parameters. Similarly, the uncertainty in

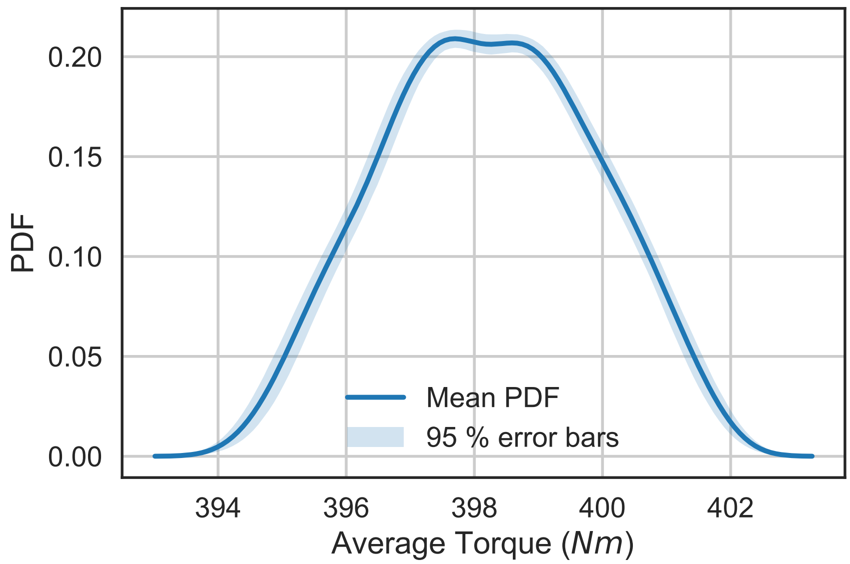

Fig. 6.1.: Illustration of PDF of average torque with variation of input parameters for operating point A

input parameters is also propagated to the sixth and twelfth harmonic components of torque as illustrated in Figs. 6.2, 6.3, 6.5 and 6.6 respectively. The two operating points under consideration belong to two different torque regions, namely, high (>300 Nm) and medium (>150 Nm and <300 Nm) torque regions. The propagation study shows the influence of input parameters at these regions.

6.2 Case Study 2

In another instance, we consider the effect of gradual wearing of the punching tool on the torque profile of the PMSM. Additionally, we also assume that the punching tools responsible for all the degraded zones are in the same state. Thus, all the degraded zones follow the same *B-H* characteristic. To perform the analysis, we consider another operating point, C, with $I_{\text{pk}} = 75$ A and $\phi_c = 60$ deg ($I_q = 37.5$ A, $I_d = -64.951$ A). At this point, we fix the value of the last two rows of distribution in Table 5.1 to their mean value and vary the distribution from rows $3-7$ linearly from

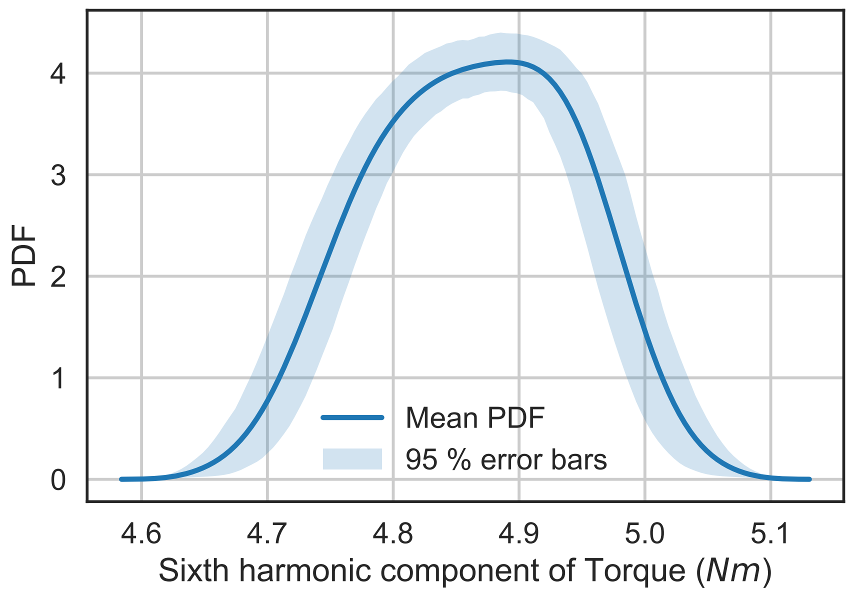

Fig. 6.2.: Illustration of PDF of sixth harmonic component of torque with variation of parameters for operating point A

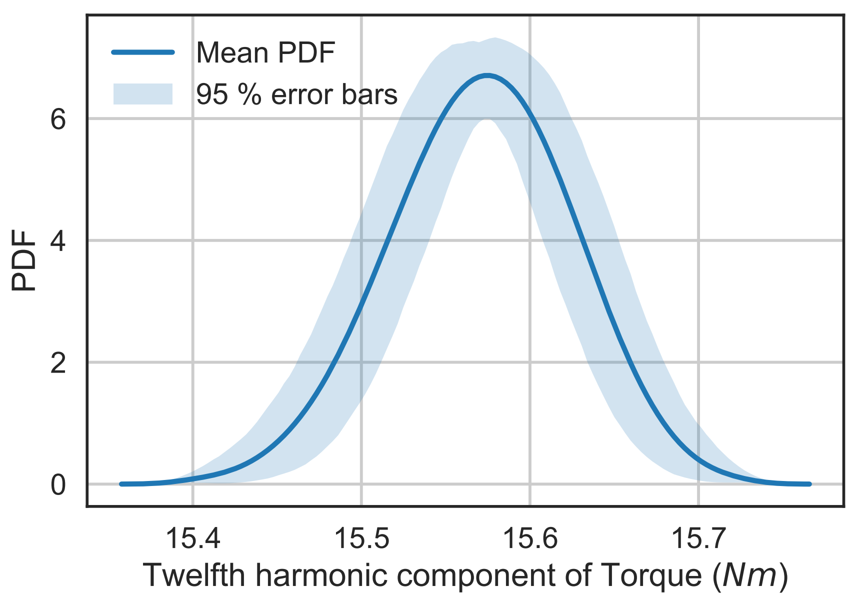

Fig. 6.3.: Illustration of PDF of twelfth harmonic component of torque with variation of input parameters for operating point A

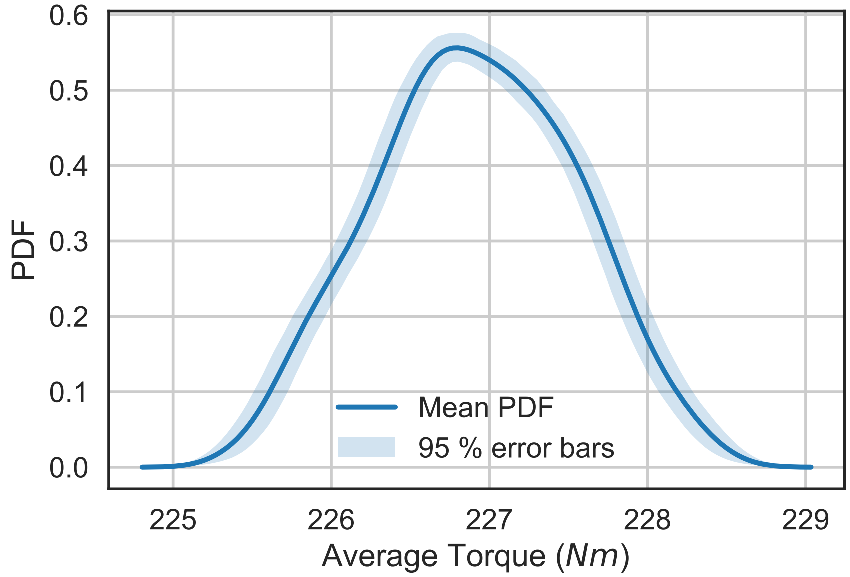

Fig. 6.4.: Illustration of PDF of average torque with variation of input parameters for operating point B

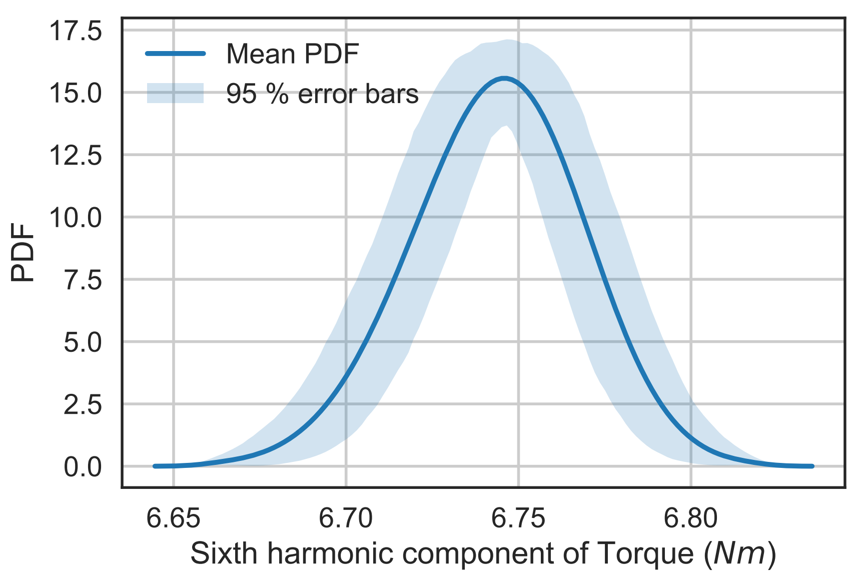

Fig. 6.5.: Illustration of PDF of sixth harmonic component of torque with variation of parameters for operating point B

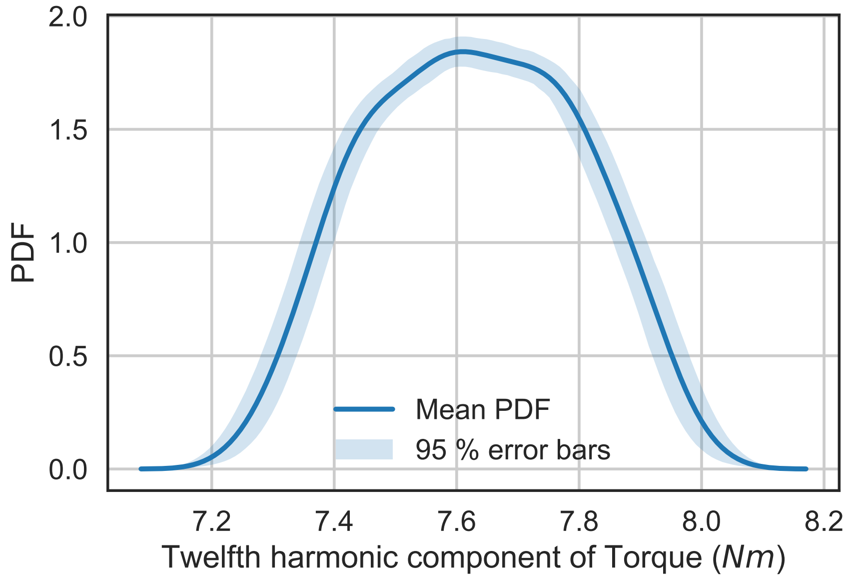

Fig. 6.6.: Illustration of PDF of twelfth harmonic component of torque with variation of input parameters for operating point B

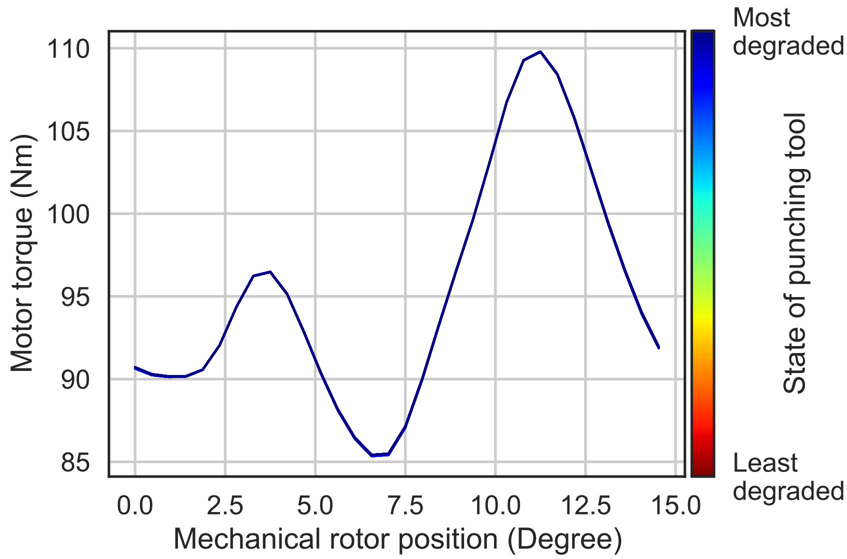

Fig. 6.7.: Illustration of torque waveform with the gradual wearing of punching tool

their lower bound to the upper bound. To do so, we sample 1000 points that vary linearly in this space and obtain the predictive mean values of the torque waveform from the surrogate. The variation in the waveform with the variation of the state of the punching tool can be visualized in Fig. 6.7. The histogram of the average torque can be observed in Figs. 6.8. It can be seen that the effect of punching has minimal effect on the torque profile of the machine. Since we have established in Section 5.2.3 that the sensitivity of sixth and twelfth harmonic components of torque cannot be predicted adequately by the surrogate model, we do not perform the study concerning the sensitivity of these QoIs to punching uncertainty.

Furthermore, we perform a similar study in an entire operating range by varying I_{pk} from 0 to 250 A and ϕ_c from 0 to 75 degrees. The mean and standard deviation of the average torque can be observed in Figs. 6.9 and 6.10. Fig. 6.10 confirms that the effect of punching is minimal in the considered operating range as well. Since, an interior PMSM is designed to operate in the flux-weakening region, it can be conveniently claimed that punching has minimal effect on the torque waveform of a interior PMSM from the results shown in Fig. 6.10.

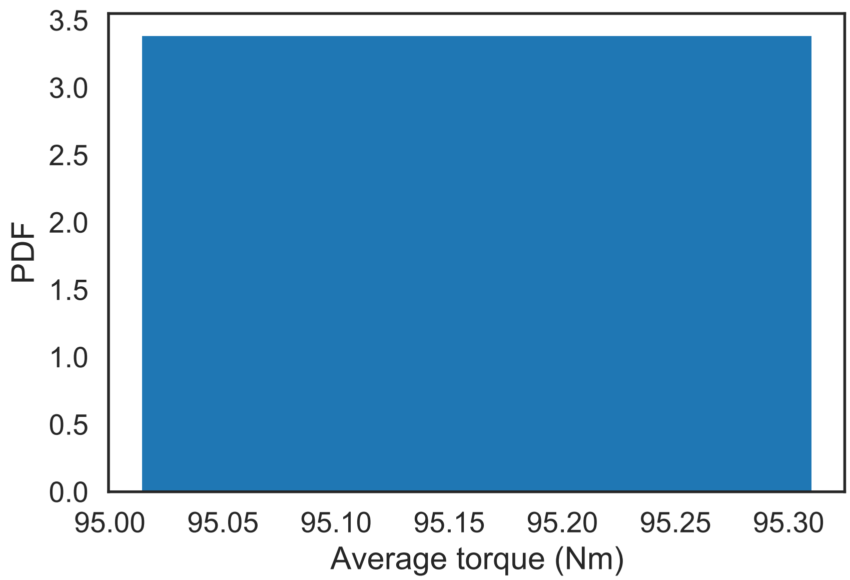

Fig. 6.8.: Illustration of average torque with the gradual wearing of punching tool

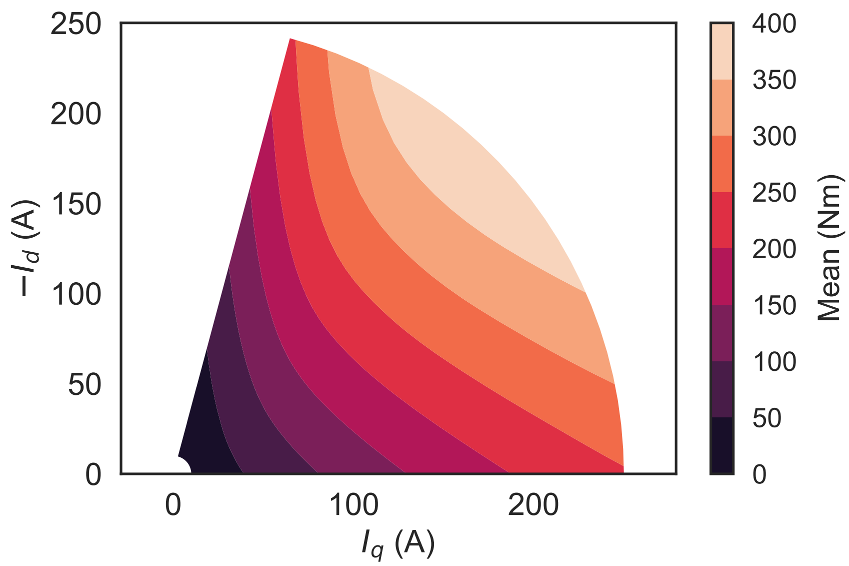

Fig. 6.9.: Illustration of mean of average torque with the gradual wearing of punching tool in an operating range

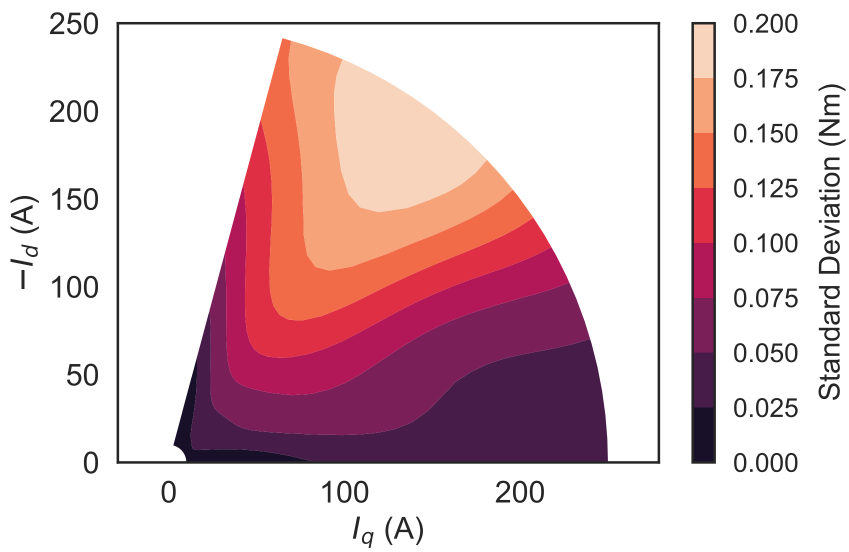

Fig. 6.10.: Illustration of standard deviation of average torque with the gradual wearing of punching tool in an operating range

7. PROPAGATION OF UNCERTAINTY IN B-H CURVES AND REMANENT FLUX DENSITY OF PERMANENT MAGNETS TO THE PMSM DRIVE SYSTEM

In this chapter, we assess the combined effect of uncertainty in B-H curves and remanent magnetic flux density (B_r) of permanent magnets on the maximum average torque ($\max(\bar{T})$) vs rotor mechanical speed (ω_{rm}) characteristics of the permanent magnet synchronous machine (PMSM), minimum DC-link voltage required for the machine/drive system and the current limit of the PMSM operating under maximum torque per ampere (MTPA) condition.

7.1 Case Study 1

Initially, we evaluate the $\max(\bar{T})$ vs ω_{rm} characteristics of the PMSM operating under no uncertainty in B-H curves and B_r. We obtain these characteristics by solving an optimization problem at discrete points in the speed range, $\omega_{\text{rm}} \in$ [0, 6000 rpm] . The problem is defined as follows,

Objective function: maximize $\bar{T}(I_{\text{pk}}, \phi_c)$

Subject to:

1. $V_{\min}(I_{\text{pk}}, \phi_c, \Lambda_{\text{qs}}(I_{\text{pk}}, \phi_c), \Lambda_{\text{ds}}(I_{\text{pk}}, \phi_c)) \leq V_{\text{dc}}$,
2. $I_{\text{pk}} \leq I_{\max}$

where $V_{\text{dc}} = 500$ V is the DC-link voltage and $I_{\max} = 250$ A is the current limit of the windings in the PMSM.

We use a non-linear optimization method, constrained optimization by linear approximation (*COBYLA*) [44], to solve the problem. This method uses the surrogate model of $\bar{T}$ to obtain the $\max(\bar{T})$ and the surrogate models corresponding to Λ_{qs} and

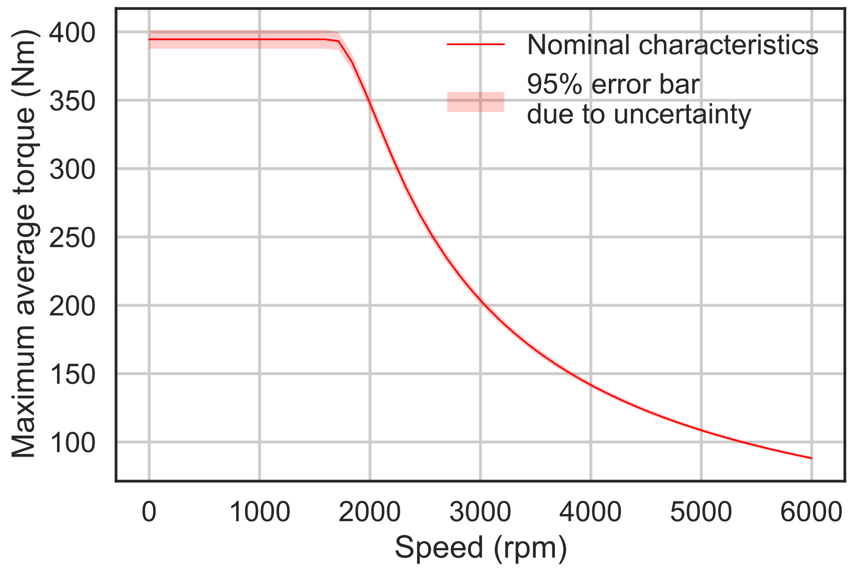

Fig. 7.1.: Impact of uncertainty in B-H curves and B_r on the $\max(\bar{T})$ vs ω_{rm} characteristics

Λ_{ds} to evaluate $V_{\min}$. To remove the effect of uncertainty in B-H curves and B_r, we set the uncertain parameters (rows 3-6 in Table 5.1) of the surrogate models to their mean values. Thereafter, we prepare a look-up table of I_{pk} and ϕ_c at discrete ω_{rm}'s by solving the optimization problem. The values of the look-up table are reported in Tables 7.1 and 7.2.

Our goal is to observe the uncertainty in the nominal $\max(\bar{T})$ vs ω_{rm} characteristics of the machine due to the uncertainty in B-H curves and B_r. Thus, at each operating point in the prepared look-up table, we evaluate the average torque from the surrogate at 1000 random samples from the original distribution of the parameters from rows 3-6 mentioned in Table 5.1, i.e. the parameters reflecting uncertainty in B-H curves and B_r. The $\max(\bar{T})$ vs ω_{rm} curve under the impact of considered uncertainties can be observed in Fig. 7.1. The 95% error bar corresponds to the 95% of the total variation caused due to the influence of uncertainties in B-H curves and B_r about the nominal characteristics.

Table 7.1.: Look-up table of $\max(\bar{T})$ vs ω_{rm} characteristics of PMSM

Mechanical rotor speed (rpm)	**Amplitude of current (A)**	**Current angle (degree)**
0.0000	250.0000	47.5700
122.4490	250.0000	47.5700
244.8980	250.0000	47.5700
367.3469	250.0000	47.5700
489.7959	250.0000	47.5700
612.2449	250.0000	47.5700
734.6939	250.0000	47.5700
857.1429	250.0000	47.5700
979.5918	250.0000	47.5700
1102.0408	250.0000	47.5700
1224.4898	250.0000	47.5700
1346.9388	250.0000	47.5700
1469.3878	250.0000	47.5700
1591.8367	250.0000	47.5701
1714.2857	250.0000	50.8713
1836.7347	250.0000	58.2778
1959.1837	250.0000	62.9381
2081.6327	250.0000	66.2818
2204.0816	250.0000	68.8989
2326.5306	241.0405	70.0448
2448.9796	232.1874	70.9050
2571.4286	224.4625	71.6639
2693.8776	217.6144	72.3386
2816.3265	211.4580	72.9413
2938.7755	205.8735	73.4832

Table 7.2.: Look-up table of $\max(\bar{T})$ vs ω_{rm} characteristics of PMSM (contd.)

Mechanical rotor speed (rpm)	**Amplitude of current (A)**	**Current angle (degree)**
3061.2245	200.7831	73.9742
3183.6735	196.1444	74.4248
3306.1224	191.9171	74.8426
3428.5714	188.0651	75.2336
3551.0204	184.5475	75.6016
3673.4694	181.3265	75.9495
3795.9184	178.3638	76.2788
3918.3673	175.6282	76.5911
4040.8163	173.0917	76.8875
4163.2653	170.7317	77.1693
4285.7143	168.5289	77.4373
4408.1633	166.4688	77.6928
4530.6122	164.5359	77.9364
4653.0612	162.7216	78.1694
4775.5102	161.0153	78.3923
4897.9592	159.4096	78.6061
5020.4082	157.8966	78.8114
5142.8571	156.4712	79.0089
5265.3061	155.1258	79.1992
5387.7551	153.8560	79.3827
5510.2041	152.6572	79.5600
5632.6531	151.5237	79.7313
5755.1020	150.4531	79.8972
5877.5510	149.4398	80.0579
6000.0000	148.4804	80.2137

Consequently, due to the variation of the $\max(\bar{T})$ vs ω_{rm} characteristics, there is variation of the minimum DC-link voltage, V_{min}, required to sustain the demanded torque of the machine. This deviation can be observed in Fig. 7.2. The maximum deviation of V_{min} is at $\omega_{\mathrm{rm}} = 6000$ rpm. Thus, we observe the probability density function (PDF) of the variation of V_{min} at $\omega_{\mathrm{rm}} = 6000$ rpm in Fig. 7.3. It can be inferred from Fig. 7.3 that to be able to sustain the required torque, the V_{dc} must be at least greater than 520 V (4% greater than the nominal value).

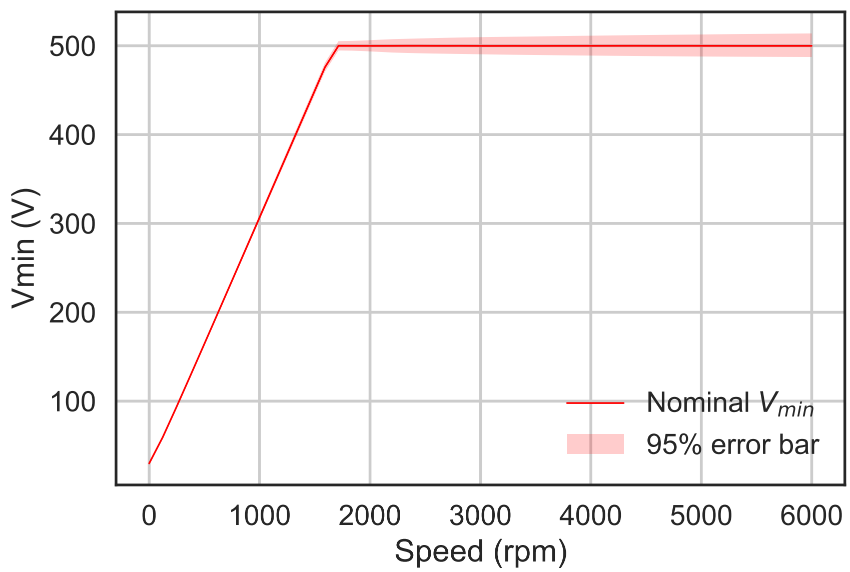

Fig. 7.2.: Impact of uncertainty in B-H curves and B_r on V_{min} vs ω_{rm} characteristics

7.2 Case Study 2

In the previous study, it can be observed that at low speeds, the PMSM operates under current limited region where the torque capability of the nominal machine, i.e. the PMSM operating under no uncertainty, is limited by I_{max}. In this zone, the PMSM is operating under MTPA condition. Considering the nominal machine, it can be observed in Fig. 7.1 that the I_{pk} required to sustain the $\max(\bar{T})$ would be more than I_{max}. We intend to observe the PDF of the variation of I_{pk} of the nominal

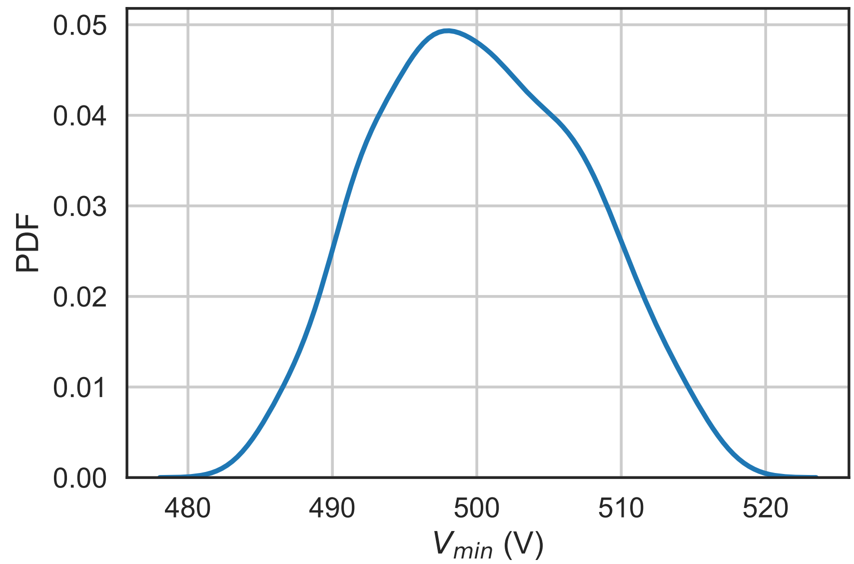

Fig. 7.3.: PDF of V_{min} at $\omega_{\mathrm{rm}} = 6000$ rpm due to uncertainty in B-H curves and B_r on V_{min}

machine in this region. To this end, we evaluate the MTPA curve of the machine using the surrogate of $\bar{T}$ at discrete points varying $I_{\mathrm{pk}} \in [0,\ 300\ \mathrm{A}]$ (see Fig. 7.4). It can be observed that at low torque/current region, the surrogate fails to adequately predict the average torque as established in Section 5.3.1. We use a shape-preserving piecewise cubic Hermite polynomial (PCHIP) function to interpolate the values of I_{pk} as a function of $\max(\bar{T})$, $I_{\mathrm{pk}}(\max(\bar{T}))$. Using this function, we obtain the variation of I_{pk} with the variation of $\max(\bar{T})$ under the influence of uncertainty in B-H curves and B_r. The PDF of this variation is shown in Fig. 7.5. It can be observed that I_{pk} overshoots I_{max} by more than 5 A.

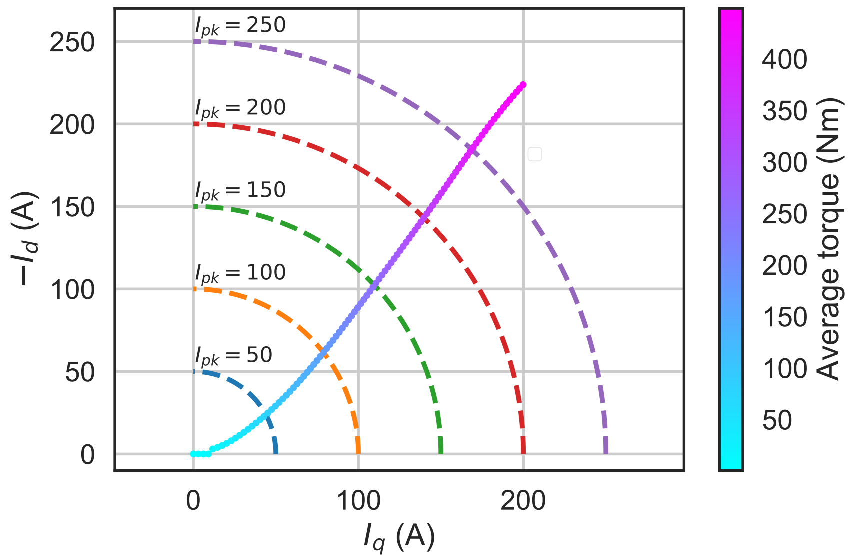

Fig. 7.4.: Illustration of MTPA operation of the PMSM in the entire operating range

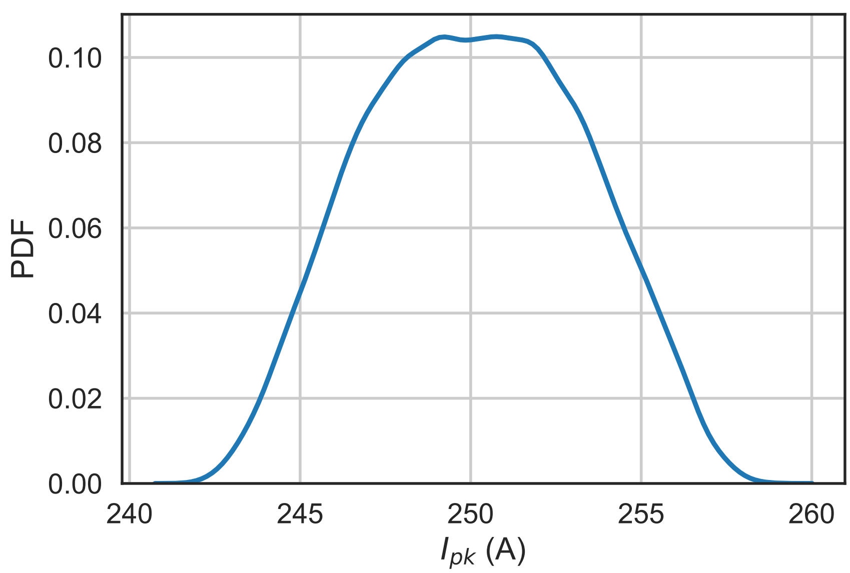

Fig. 7.5.: PDF of I_{pk} due to uncertainty in B-H curves and B_r operating under MTPA condition

8. CONCLUSION

In this study, our attempt was to quantify the effect of uncertainty in the B-H curves due to the state of the punching tool, unpredictability of the material composition and the uncertainty in the value of saturation magnetization on the torque profile of a permanent magnet synchronous motor (PMSM). We extended the work further to consider the combined effect of uncertainty in B-H curves and remanent flux density of permanent magnets on the PMSM machine/drive system.

The model for quantifying the uncertainty in B-H curves of steel due to punching was built using principal component analysis (PCA). Using a synthetic data set of B-H curves, it was shown that by applying PCA on the data set, the number of uncertain dimensions was reduced from 41 to 1. Additionally, using this 1 uncertain input in the low-dimensional space, samples of B-H curves could be generated for training the surrogate model cheaply. Furthermore, while conducting the propagation study, it was computationally efficient to deal with 1 uncertain input in the low-dimensional space instead of 41 in the high-dimensional space. We considered the material uncertainty and the epistemic uncertainty in the saturation flux density of the B-H curve as well. To this end, we modeled the uncertainties in these quantities using random variables based on our knowledge from literature.

The mesh in the finite element (FE) simulator was modified to incorporate the degraded zones reflecting the local plastic deformation due to punching. All the elements in the zone were assumed to have a certain magnetic characteristic (dictated by the degraded B-H curves) depending on the sample obtained from the reduced order stochastic model. In Chapter 5, an inexpensive surrogate model using Gaussian process (GP) regression was built to conduct the propagation study. Again, PCA was used to reduce the dimensionality of the output from the FE simulator reducing the number of GP functions required to learn and predict the output. The dimensionality of the output was reduced from 32 in the high-dimensional space to 8 in the low-dimensional space. Thus, only 8 scalar GP functions were used to learn the 8 principal components in the low-dimensional space. Using these GP functions, a prediction accuracy of 99% was achieved for 92% of the samples from the validation set. However, at low-torque region (average torque < 50 Nm), the surrogate fails to predict the output with significant accuracy (maximum relative L_2-norm error $> 5\%$).

Using the trained surrogate, certain statistics were evaluated about the torque response of the machine. We conducted a parametric uncertainty study where it was found that the limited number of training points used in training of the surrogate has an impact on the surrogate evaluation providing an uncertain statistics about the average torque, the sixth and twelfth harmonic components of the torque. Additionally, in the second case study, we found that the uncertainty due to punching on *B*-*H* curves has negligible impact on the output torque of the PMSM.

We extended this work further to consider the combined impact of uncertainties in *B*-*H* curves and remanent flux density of permanent magnets on the PMSM machine/drive system. To this end, we built 3 surrogate models for average torque and *q*- and *d*- axes flux linkages of the machine using GP regression. Finally, using the surrogate models, we conducted a propagation study observing the effect of the considered uncertainties on the maximum average torque ($\max(\bar{T})$) vs speed (ω_{rm}) characteristics of the PMSM, the minimum DC-link voltage ($V_{\min}$) required to drive the machine and the current limit of the PMSM operating under maximum torque per ampere (MTPA) condition. It was found that the considered uncertainties have greater effect on $\max(\bar{T})$ vs ω_{rm} characteristics of the PMSM in the MTPA region than in the Voltage limited region. Additionally, it was found that the $V_{\min}$ required to drive the machine under uncertainty has to be atleast 4% greater than its nominal value and the current rating of the phase windings must be at least 2% greater than their nominal value to be able to operate under the considered uncertainties.

The future scope of this work would be to consider the impact of uncertainties due to variations in geometry of the machine on the output torque of the PMSM.

Furthermore, it would be interesting to observe the effects of B-H curve uncertainties on the core loss of the machine. The training of the surrogate models in this study was done by sampling input points from the entire parameter space. However, this method of sampling training points can be improved by strategic sampling using the information of epistemic uncertainty provided by the model. Additionally, the length scale of each input parameter from the covariance function (Eq. (5.25)) that provides the sensitivity of the each input dimension to the response is another variable that can be used for strategic sampling. Using an acquisition function that depends on these variables, strategic sampling can be done in the input parameter space. By employing this technique, the number of samples required to train the surrogate would reduce, improving the prediction at low torque region at the same time.

REFERENCES

REFERENCES

[1] E. Mangiorou, "Correlation of grain growth phenomena with magnetic properties in non - oriented electrical steels," *IOP Conference Series: Materials Science and Engineering*, vol. 108, p. 012016, March. 2016.

[2] S. Szymura, C. Adamczyk, H. Majchrzak, J. Mehlis, and A. Zawada, "Effect of composition and impurities on the magnetic properties of low-carbon electrical steels," *Journal of Material Science Letter*, vol. 6, no. 11, pp. 1259–1260, November. 1987.

[3] K. Honma, T. Nozawa, H. Kobayashi, Y. Shimoyama, I. Tachino, and K. Miyoshi, "Development of non-oriented and grain-oriented silicon steel," *IEEE Transaction on Magnetics*, vol. 21, no. 5, pp. 1903–1908, September. 1985.

[4] M. deCampos, T. Yonamine, M. Fukuhara, F. Landgraf, C. Achete, and F. Missell, "Effect of Frequency on the Iron Losses of 0.5% and 1.5% Si Nonoriented Electrical Steels," *IEEE Transaction on Magnetics*, vol. 42, no. 10, pp. 2812–2814, October. 2006.

[5] N. Takahashi, M. Morishita, D. Miyagi, and M. Nakano, "Comparison of Magnetic Properties of Magnetic Materials at High Temperature," *IEEE Transaction on Magnetics*, vol. 47, no. 10, pp. 4352–4355, October. 2011.

[6] A. Krings, S. A. Mousavi, O. Wallmark, and J. Soulard, "Temperature influence of NiFe Steel laminations on the characteristics of small slotless permanent magnet machines," *IEEE Transaction on Magnetics*, vol. 49, no. 7, pp. 4064–4067, July. 2013.

[7] A. Schoppa, J. Schneider, and J.-O. Roth, "Influence of the cutting process on the magnetic properties of non-oriented electrical steels," *Journal of Magnetism and Magnetic Material*, vol. 215-216, pp. 100–102, June. 2000.

[8] M. Oka, M. Kawano, K. Shimada, T. Kai, and M. Enokizono, "Evaluation of the magnetic properties of the rotating machines for the building factor clarification," *Przeglad Elektrotechniczny (Electrical Review)*, vol. 87, no. 9B, pp. 43–46, 2011.

[9] W. Deprez, J. Schneider, T. Kochmann, F. Henrotte, and K. Hameyer, "Influence of the manufacturing process on the magnetic properties of electrical steel in e-cores," *Soft Magnetic Materials*, vol. 16, 2003.

[10] H. M. S. Harstick, M. Ritter, and W. Riehemann, "Influence of punching and tool wear on the magnetic properties of non-oriented electrical Steel," *IEEE Transaction on Magnetics*, vol. 50, no. 4, pp. 1–4, April. 2014.

[11] H. A. Weiss, P. Trober, R. Golle, S. Steentjes, N. Leuning, S. Elfgen, K. Hameyer, and W. Volk, "Impact of punching parameter variations on magnetic properties of nongrain-Oriented Electrical Steel," *IEEE Transactions on Industrial Applications*, vol. 54, no. 6, pp. 5869–5878, November. 2018.

[12] H. Weiss, N. Leuning, S. Steentjes, K. Hameyer, T. Andorfer, S. Jenner, and W. Volk, "Influence of shear cutting parameters on the electromagnetic properties of non-oriented electrical steel sheets," *Journal of Magnetism and Magnetic Material*, vol. 421, pp. 250–259, January. 2017.

[13] M. Bali and A. Muetze, "The degradation depth of non-grain oriented electrical steel sheets of electric machines due to mechanical and laser cutting: A state-of-the-art review," *IEEE Transactions on Industrial Applications*, vol. 55, no. 1, pp. 366–375, January. 2019.

[14] D. K. Rao and V. Kuptsov, "Effective use of magnetization data in the Design of electric machines with overfluxed regions," *IEEE Transaction on Magnetics*, vol. 51, no. 7, pp. 1–9, July. 2015.

[15] A. Krings, *Iron losses in electrical machines : influence of material properties, manufacturing processes and inverter operation.* KTH Royal Institute of Technology, 2014.

[16] K. Bourchas, A. Stening, J. Soulard, A. Broddefalk, M. Lindenmo, M. Dahlen, and F. Gyllensten, "Quantifying effects of cutting and welding on Magnetic properties of electrical steels," *IEEE Transactions on Industrial Applications*, vol. 53, no. 5, pp. 4269–4278, September. 2017.

[17] M. Bali, H. De Gersem, and A. Muetze, "Finite-Element Modeling of Magnetic Material Degradation Due to Punching," *IEEE Transaction on Magnetics*, vol. 50, no. 2, pp. 745–748, February. 2014.

[18] A. J. Clerc and A. Muetze, "Measurement of stator core magnetic degradation during the manufacturing process," *IEEE Transactions on Industry Applications*, 2012.

[19] Z. Wang, S. Li, R. Cui, X. Wang, and B. Wang, "Influence of grain Size and blanking clearance on magnetic properties deterioration of non-oriented electrical steel," *IEEE Transaction on Magnetics*, vol. 54, no. 5, pp. 1–7, May. 2018.

[20] D. Schuller, D. Hohs, S. Schweizer, D. Goll, and G. Schneider, "Tailoring the microstructure of soft magnetic composites for electric motor applications," *IEEE Transaction on Magnetics*, vol. 55, no. 2, pp. 1–4, February. 2019.

[21] J. Brauer, "Simple equations for the magnetization and reluctivity curves of steel," *IEEE Transaction on Magnetics*, vol. 11, no. 1, pp. 81–81, January. 1975.

[22] A. E. Umenei, Y. Melikhov, and D. C. Jiles, "Models for extrapolation of magnetization Data on magnetic cores to high fields," *IEEE Transaction on Magnetics*, vol. 47, no. 12, pp. 4707–4711, December. 2011.

[23] A. M. Knight and D. G. Dorrell, "Improving the torque prediction of saturated automotive drive machines by accurate representation of saturated \$B/H\$ Curves," *IEEE Transaction on Magnetics*, vol. 48, no. 11, pp. 4630–4633, November. 2012.

[24] R. Ramarotafika, A. Benabou, and S. Clenet, "Stochastic modeling of soft magnetic properties of electrical steels: Application to stators of electrical machines," *IEEE Transaction on Magnetics*, vol. 48, no. 10, pp. 2573–2584, October. 2012.

[25] S. Clenet, "Uncertainty quantification in computational electromagnetics: The stochastic approach," *International Compumag society Newsletters*, vol. 20, no. 1, pp. 2–12, March. 2013.

[26] P. Offermann and K. Hameyer, "A polynomial chaos meta model for non linear stochastic magnet variations," *COMPEL*, vol. 32, no. 4, pp. 1211–1218, 2013.

[27] A. Kallaste, A. Belahcen, and T. Vaimann, "Effect of pm parameters variability on the operation quantities of a wind generator," in *2015 IEEE WEMDCD*, March. 2015, pp. 242–247.

[28] Z. Bontinck, H. De Gersem, and S. Schops, "Response Surface Models for the Uncertainty Quantification of Eccentric Permanent Magnet Synchronous Machines," *IEEE Transaction on Magnetics*, vol. 52, no. 3, pp. 1–4, March. 2016.

[29] A. Bartel, H. De Gersem, T. Hulsmann, U. Romer, S. Schops, and T. Weiland, "Quantification of uncertainty in the field quality of magnets originating from material measurements," *IEEE Transaction on Magnetics*, vol. 49, no. 5, pp. 2367–2370, May. 2013.

[30] R. Tripathy, I. Bilionis, and M. Gonzalez, "Gaussian processes with built-in dimensionality reduction: Applications to high-dimensional uncertainty propagation," *Journal of Computational Physics*, vol. 321, pp. 191–223, 9 2016.

[31] T. Burress, C. Coomer, S. Campbell, L. Seiber, L. D. Marlino, R. Staunton, and J. Cunningham, "Evaluation of the 2007 toyota camry hybrid synergy drive system," Oak Ridge National Laboratory (ORNL), Oak Ridge, TN, Tech. Rep., 2008.

[32] P. Krause, O. Wasynczuk, S. D. Sudhoff, and S. Pekarek, *Reference-Frame Theory*. IEEE, 2013.

[33] J. P. A. Bastos and N. Sadowski, *Electromagnetic modeling by finite element methods*. Marcel Dekker, 2003.

[34] N. Sadowski, Y. Lefèvre, M. Lajoie-Mazenc, and J. Cros, "Finite element torque calculation in electrical machines while considering the movement," *IEEE transactions on magnetics*, vol. 28, no. 2, pp. 1410–1413, 1992.

[35] J. Coulomb, "A methodology for the determination of global electromechanical quantities from a finite element analysis and its application to the evaluation of magnetic forces, torques and stiffness," *IEEE Transaction on Magnetics*, vol. 19, no. 6, pp. 2514–2519, November. 1983.

[36] A. Arkkio, "Finite element analysis of cage induction motors fed by static frequency converters," *IEEE Transaction on Magnetics*, vol. 26, no. 2, pp. 551–554, March. 1990.

[37] S.-K. Kuo, W.-C. Lee, S.-Y. Lin, and C.-Y. Lu, "The Influence of Cutting Edge Deformations on Magnetic Performance Degradation of Electrical Steel," *IEEE Transactions on Industry Applications*, vol. 51, no. 6, pp. 4357–4363, November. 2015.

[38] L. v. d. Maaten, L. van der Maaten, E. O. Postma, and H. J. van den Herik, "Dimensionality Reduction: A Comparative Review," *Journal of Machine Learning Research*, 2008.

[39] C. M. Bishop, *Pattern Recognition and Machine Learning*. Springer, 2006.

[40] I. Bilionis, E. M. Constantinescu, and M. Anitescu, "Data-driven model for solar irradiation based on satellite observations," *Sol. Energy*, vol. 110, pp. 22–38, December. 2014.

[41] C. M. Bishop, "Continuous latent variables," in *Pattern Recognition and Machine Learning*. Springer, 2006, p. 561.

[42] A. I. H. Committee, *Metals Handbook, 8th Edition. Volume 1: Properties and Selection*. American Society for Metals, 1966.

[43] J. Hsu, C. Ayers, C. Coomer *et al.*, "Report on toyota/prius motor design and manufacturing assessment," Oak Ridge Nat. Laboratory (ORNL), Oak Ridge, TN (United States), Tech. Rep., 2004.

[44] A. Conn, K. Scheinberg, and P. Toint, *On the convergence of derivative-free methods for unconstrained optimization*. Cambridge University Press, 1997, pp. 83–10.

APPENDIX

A. APPENDIX

The data for the synthetic B-H is provided here. The vector of B values, **b**, is same for all the curves. The vector of H values for the curves are represented as columns of **H** matrix mentioned in Section 4.1.

Table A.1.: Table of B values of synthetically generated data

b		
0.0416	0.6241	1.2065
0.0832	0.6657	1.2481
0.1248	0.7073	1.2897
0.1664	0.7489	1.3313
0.2080	0.7905	1.3729
0.2496	0.8321	1.4140
0.2912	0.8737	1.4542
0.3328	0.9153	1.4936
0.3744	0.9569	1.5335
0.4160	0.9985	1.5736
0.4576	1.0401	1.6139
0.4992	1.0817	1.6538
0.5409	1.1233	1.6934
0.5825	1.1649	

Table A.2.: Table of H values of synthetically generated data

$\mathbf{h}^{(1)}$		$\mathbf{h}^{(2)}$		$\mathbf{h}^{(3)}$	
26.5302	666.1948	21.7077	476.8970	28.6060	747.6765
38.3408	774.9766	31.0894	567.7889	41.4621	864.1589
45.4029	892.9599	36.4757	673.8647	49.2455	987.2677
52.0498	1047.6323	41.4198	819.9388	56.6254	1145.6411
58.3107	1279.2378	45.9534	1045.2204	63.6298	1379.9688
64.4285	1699.7925	50.2749	1455.8066	70.5208	1804.8143
71.0394	2370.8106	54.8802	2126.7851	77.9951	2475.8495
78.2768	3363.5671	59.8617	3138.8251	86.2034	3460.3055
86.6422	4505.5536	65.5877	4323.6852	95.7049	4583.8375
95.6479	5880.6249	71.6713	5722.1750	105.9684	5948.8284
105.4933	7285.2091	78.2520	7115.8279	117.2191	7358.1180
116.8408	8865.0238	85.8063	8661.6379	130.1994	8952.5696
128.9929	10653.2414	93.8053	10408.8416	144.1391	10758.4414
142.2119		102.4362		159.3331	
157.3568		112.3092		176.7472	
173.4059		122.6890		195.2366	
190.6790		133.8146		215.1558	
210.1184		146.3607		237.5623	
232.6636		160.9942		263.5132	
257.3212		177.0555		291.8709	
284.8009		195.0916		323.4156	
314.0539		214.4717		356.9183	
346.5500		236.3287		393.9940	
383.4672		261.6450		435.9046	
423.5610		289.8297		481.1246	
469.1894		322.8652		532.1734	
525.2690		364.7034		594.3832	
588.8726		414.1770		664.0689	

$\mathbf{h}^{(4)}$		$\mathbf{h}^{(5)}$		$\mathbf{h}^{(6)}$	
28.6060	747.6765	22.4091	504.4305	20.8604	443.6395
41.4621	864.1589	32.1441	597.9245	29.8154	531.3884
49.2455	987.2677	37.7742	705.7322	34.9073	635.3722
56.6254	1145.6411	42.9660	853.0570	39.5523	779.9356
63.6298	1379.9688	47.7508	1079.2584	43.7824	1004.1062
70.5208	1804.8143	52.3335	1491.2945	47.7882	1412.9411
77.9951	2475.8495	57.2306	2162.2788	52.0412	2083.9126
86.2034	3460.3055	62.5402	3171.5139	56.6264	3099.3405
95.7049	4583.8375	68.6501	4350.1381	61.8887	4291.7330
105.9684	5948.8284	75.1587	5745.2217	67.4589	5694.3372
117.2191	7358.1180	82.2143	7140.4645	73.4661	7086.0696
130.1994	8952.5696	90.3202	8691.2205	80.3538	8625.9054
144.1391	10758.4414	98.9234	10444.3898	87.6233	10365.9034
159.3331		108.2216		95.4481	
176.7472		118.8614		104.3949	
195.2366		130.0658		113.7786	
215.1558		142.0856		123.8242	
237.5623		155.6343		135.1592	
263.5132		171.4185		148.4027	
291.8709		188.7302		162.9537	
323.4156		208.1399		179.3307	
356.9183		228.9560		196.9762	
393.9940		252.3605		216.9641	
435.9046		279.3641		240.2422	
481.1246		309.2810		266.3347	
532.1734		344.1482		297.1577	
594.3832		388.0578		336.4939	
664.0689		439.5866		383.4850	

$\mathbf{h}^{(7)}$		$\mathbf{h}^{(8)}$		$\mathbf{h}^{(9)}$	
20.8604	443.6395	19.3772	385.4185	27.7004	712.1265
29.8154	531.3884	27.5852	467.6652	40.1003	825.2491
34.9073	635.3722	32.1617	567.9866	47.5690	946.1217
39.5523	779.9356	36.2829	709.9056	54.6291	1102.8804
43.7824	1004.1062	39.9817	932.1312	61.3091	1336.0204
47.7882	1412.9411	43.4351	1337.9001	67.8628	1758.9938
52.0412	2083.9126	47.0712	2008.8594	74.9604	2430.0216
56.6264	3099.3405	50.9626	3030.2182	82.7451	3418.0990
61.8887	4291.7330	55.4132	4235.7971	91.7509	4549.6826
67.4589	5694.3372	60.0846	5645.6039	101.4656	5919.0716
73.4661	7086.0696	65.0877	7033.9742	112.1032	7326.3082
80.3538	8625.9054	70.8088	8563.3515	124.3711	8914.3738
87.6233	10365.9034	76.8009	10290.7351	137.5309	10712.5431
95.4481		83.2145		151.8632	
104.3949		90.5399		168.2873	
113.7786		98.1800		185.7120	
123.8242		106.3348		204.4767	
135.1592		115.5497		225.5887	
148.4027		126.3598		250.0537	
162.9537		138.2670		276.7971	
179.3307		151.7395		306.5682	
196.9762		166.3484		338.2167	
216.9641		183.0641		373.2944	
240.2422		202.7742		413.0264	
266.3347		225.2039		456.0099	
297.1577		252.1539		504.6938	
336.4939		287.1099		564.2290	
383.4850		329.7551		631.2612	

$\mathbf{h}^{(10)}$		$\mathbf{h}^{(11)}$		$\mathbf{h}^{(12)}$	
27.7004	712.1265	23.6546	553.3196	28.5697	746.2492
40.1003	825.2491	34.0169	651.4340	41.4074	862.5966
47.5690	946.1217	40.0798	762.3171	49.1782	985.6157
54.6291	1102.8804	45.7113	911.8624	56.5452	1143.9242
61.3091	1336.0204	50.9423	1139.6971	63.5367	1378.2042
67.8628	1758.9938	55.9889	1554.3078	70.4141	1802.9746
74.9604	2430.0216	61.4040	2225.3023	77.8732	2474.0095
82.7451	3418.0990	67.2962	3229.5572	86.0646	3458.6109
91.7509	4549.6826	74.0878	4397.1085	95.5461	4582.4661
101.4656	5919.0716	81.3510	5786.1439	105.7877	5947.6337
112.1032	7326.3082	89.2498	7184.2099	117.0137	7356.8408
124.3711	8914.3738	98.3354	8743.7482	129.9654	8951.0360
137.5309	10712.5431	108.0111	10507.5099	143.8738	10756.5985
151.8632		118.4943		159.0332	
168.2873		130.4957		176.4075	
185.7120		143.1643		194.8542	
204.4767		156.7717		214.7270	
225.5887		172.1007		237.0816	
250.0537		189.9283		262.9728	
276.7971		209.4601		291.2657	
306.5682		231.3088		322.7392	
338.2167		254.6747		356.1674	
373.2944		280.8269		393.1628	
413.0264		310.8266		434.9860	
456.0099		343.8193		480.1162	
504.6938		381.9387		531.0701	
564.2290		429.5264		593.1725	
631.2612		484.7045		662.7517	

$\mathbf{h}^{(13)}$		$\mathbf{h}^{(14)}$		$\mathbf{h}^{(15)}$	
28.5697	746.2492	25.1148	610.6350	24.7978	598.1945
41.4074	862.5966	36.2125	714.1661	35.7359	700.5498
49.1782	985.6157	42.7827	828.6544	42.1960	814.2557
56.5452	1143.9242	48.9298	980.8032	48.2313	965.8393
63.5367	1378.2042	54.6838	1210.5526	53.8717	1195.1732
70.4141	1802.9746	60.2743	1628.1815	59.3442	1612.1469
77.8732	2474.0095	66.2966	2299.1880	65.2347	2283.1508
86.0646	3458.6109	72.8719	3297.6043	71.6617	3282.8344
95.5461	4582.4661	80.4626	4452.1744	79.0789	4440.2222
105.7877	5947.6337	88.6107	5834.1192	87.0349	5823.7059
117.0137	7356.8408	97.4979	7235.4950	95.7076	7224.3634
129.9654	8951.0360	107.7320	8805.3291	105.6925	8791.9627
143.8738	10756.5985	118.6652	10581.5089	116.3527	10565.4472
159.0332		130.5376		127.9235	
176.4075		144.1352		141.1747	
194.8542		158.5203		155.1872	
214.7270		173.9890		170.2519	
237.0816		191.4052		187.2151	
262.9728		211.6283		206.9182	
291.2657		233.7628		228.4878	
322.7392		258.4709		252.5752	
356.1674		284.8260		278.2816	
393.1628		314.1996		306.9559	
434.9860		347.7118		339.7057	
480.1162		384.3103		375.5216	
531.0701		426.2425		416.6262	
593.1725		478.1423		467.5900	
662.7517		537.5986		526.1178	

$\mathbf{h}^{(16)}$		$\mathbf{h}^{(17)}$		$\mathbf{h}^{(18)}$	
24.7978	598.1945	23.3389	540.9286	21.1204	453.8467
35.7359	700.5498	33.5423	637.8720	30.2064	542.5603
42.1960	814.2557	39.4954	747.9756	35.3887	647.1861
48.2313	965.8393	45.0155	896.9581	40.1255	792.2132
53.8717	1195.1732	50.1334	1124.3788	44.4487	1016.7248
59.3442	1612.1469	55.0625	1538.3370	48.5514	1426.0972
65.2347	2283.1508	60.3462	2209.3289	52.9125	2097.0708
71.6617	3282.8344	66.0908	3214.8460	57.6194	3111.4589
79.0789	4440.2222	72.7096	4385.2038	63.0240	4301.5397
87.0349	5823.7059	79.7816	5775.7721	68.7517	5702.8811
95.7076	7224.3634	87.4666	7173.1226	74.9350	7095.2029
105.6925	8791.9627	96.3040	8730.4350	82.0273	8636.8723
116.3527	10565.4472	105.7078	10491.5120	89.5207	10379.0818
127.9235		115.8907		97.5928	
141.1747		127.5470		106.8239	
155.1872		139.8445		116.5134	
170.2519		153.0495		126.8904	
187.2151		167.9273		138.5971	
206.9182		185.2370		152.2672	
228.4878		204.2061		167.2818	
252.5752		225.4366		184.1680	
278.2816		248.1562		202.3459	
306.9559		273.6120		222.9074	
339.7057		302.8524		246.8110	
375.5216		335.0655		273.5457	
416.6262		372.3606		305.0478	
467.5900		419.0162		345.1519	
526.1178		473.2693		392.9048	

$\mathbf{h}^{(19)}$		$\mathbf{h}^{(20)}$		$\mathbf{h}^{(21)}$	
21.1204	453.8467	20.9101	445.5892	29.3123	775.4000
30.2064	542.5603	29.8901	533.5223	42.5241	894.5023
35.3887	647.1861	34.9993	637.6287	50.5529	1019.3551
40.1255	792.2132	39.6618	782.2808	58.1822	1178.9877
44.4487	1016.7248	43.9096	1006.5165	65.4396	1414.2415
48.5514	1426.0972	47.9340	1415.4540	72.5937	1840.5470
52.9125	2097.0708	52.2076	2086.4259	80.3616	2511.5880
57.6194	3111.4589	56.8161	3101.6552	88.9004	3493.2198
63.0240	4301.5397	62.1056	4293.6062	98.7884	4610.4728
68.7517	5702.8811	67.7058	5695.9691	109.4799	5972.0340
74.9350	7095.2029	73.7466	7087.8141	121.2087	7382.9245
82.0273	8636.8723	80.6735	8628.0002	134.7445	8982.3562
89.5207	10379.0818	87.9857	10368.4206	149.2925	10794.2347
97.5928		95.8577		165.1584	
106.8239		104.8589		183.3446	
116.5134		114.3010		202.6643	
126.8904		124.4099		223.4838	
138.5971		135.8159		246.8999	
152.2672		149.1408		274.0094	
167.2818		163.7804		303.6262	
184.1680		180.2547		336.5539	
202.3459		198.0019		371.5025	
222.9074		218.0993		410.1363	
246.8110		241.4969		453.7460	
273.5457		267.7120		500.7101	
305.0478		298.6648		553.6032	
345.1519		338.1477		617.8987	
392.9048		385.2842		689.6538	

$\mathbf{h}^{(22)}$		$\mathbf{h}^{(23)}$		$\mathbf{h}^{(24)}$	
29.3123	775.4000	19.6318	395.4134	28.4684	742.2750
42.5241	894.5023	27.9680	478.6046	41.2552	858.2469
50.5529	1019.3551	32.6330	579.5548	48.9908	981.0159
58.1822	1178.9877	36.8442	721.9277	56.3220	1139.1440
65.4396	1414.2415	40.6342	944.4872	63.2772	1373.2912
72.5937	1840.5470	44.1824	1350.7824	70.1169	1797.8523
80.3616	2511.5880	47.9244	2021.7439	77.5340	2468.8863
88.9004	3493.2198	51.9350	3042.0845	85.6780	3453.8926
98.7884	4610.4728	56.5248	4245.3997	95.1041	4578.6479
109.4799	5972.0340	61.3505	5653.9700	105.2843	5944.3071
121.2087	7382.9245	66.5260	7042.9175	116.4418	7353.2847
134.7445	8982.3562	72.4474	8574.0902	129.3138	8946.7660
149.2925	10794.2347	78.6588	10303.6394	143.1350	10751.4675
165.1584		85.3147		158.1981	
183.3446		92.9184		175.4618	
202.6643		100.8578		193.7894	
223.4838		109.3373		213.5332	
246.8999		118.9161		235.7430	
274.0094		130.1439		261.4681	
303.6262		142.5050		289.5806	
336.5539		156.4761		320.8558	
371.5025		171.6063		354.0767	
410.1363		188.8837		390.8488	
453.7460		209.2064		432.4285	
500.7101		232.2649		477.3086	
553.6032		259.8797		527.9981	
617.8987		295.5877		589.8015	
689.6538		338.9790		659.0841	

$\mathbf{h}^{(25)}$		$\mathbf{h}^{(26)}$		$\mathbf{h}^{(27)}$	
28.4684	742.2750	26.1947	653.0255	24.6855	593.7841
41.2552	858.2469	37.8363	760.5627	35.5670	695.7227
48.9908	981.0159	44.7818	877.7176	41.9881	809.1511
56.3220	1139.1440	51.3103	1031.7918	47.9836	960.5344
63.2772	1373.2912	57.4510	1262.9574	53.5838	1189.7209
70.1169	1797.8523	63.4438	1682.8186	59.0144	1606.4624
77.5340	2468.8863	69.9153	2353.8340	64.8582	2277.4654
85.6780	3453.8926	76.9957	3347.9320	71.2326	3277.5982
95.1041	4578.6479	85.1774	4492.9012	78.5884	4435.9849
105.2843	5944.3071	93.9799	5869.6017	86.4763	5820.0143
116.4418	7353.2847	103.5982	7273.4254	95.0729	7220.4170
129.3138	8946.7660	114.6818	8850.8744	104.9694	8787.2241
143.1350	10751.4675	126.5449	10636.2387	115.5329	10559.7530
158.1981		139.4448		126.9968	
175.4618		154.2229		140.1251	
193.7894		169.8776		154.0056	
213.5332		186.7230		168.9271	
235.7430		205.6828		185.7296	
261.4681		227.6776		205.2485	
289.5806		251.7372		226.6178	
320.8558		278.5599		250.4851	
354.0767		307.1260		275.9615	
390.8488		338.8820		304.3879	
432.4285		374.9921		336.8675	
477.3086		414.2574		372.4058	
527.9981		459.0097		413.2171	
589.8015		514.0986		463.8491	
659.0841		576.7192		522.0476	

$\mathbf{h}^{(28)}$		$\mathbf{h}^{(29)}$		$\mathbf{h}^{(30)}$	
24.6855	593.7841	29.8066	794.8007	26.3887	660.6421
35.5670	695.7227	43.2673	915.7366	38.1281	768.8991
41.9881	809.1511	51.4679	1041.8097	45.1410	886.5331
47.9836	960.5344	59.2716	1202.3236	51.7380	1040.9533
53.5838	1189.7209	66.7061	1438.2255	57.9483	1272.3733
59.0144	1606.4624	74.0442	1865.5526	64.0133	1692.6356
64.8582	2277.4654	82.0178	2536.5977	70.5654	2363.6526
71.2326	3277.5982	90.7877	3516.2532	77.7366	3356.9747
78.5884	4435.9849	100.9462	4629.1121	86.0246	4500.2189
86.4763	5820.0143	111.9372	5988.2732	94.9446	5875.9771
95.0729	7220.4170	124.0006	7400.2840	104.6942	7280.2407
104.9694	8787.2241	137.9252	9003.2008	115.9305	8859.0578
115.5329	10559.7530	152.8988	10819.2827	127.9607	10646.0724
126.9968		169.2349		141.0452	
140.1251		187.9614		156.0354	
154.0056		207.8622		171.9182	
168.9271		229.3117		189.0110	
185.7296		253.4343		208.2481	
205.2485		281.3547		230.5613	
226.6178		311.8524		254.9667	
250.4851		345.7480		282.1695	
275.9615		381.7084		311.1328	
304.3879		421.4327		343.3169	
336.8675		466.2313		379.8938	
372.4058		514.4159		419.6383	
413.2171		568.5996		464.8972	
463.8491		634.3547		520.5591	
522.0476		707.5580		583.7482	

$\mathbf{h}^{(31)}$		$\mathbf{h}^{(32)}$		$\mathbf{h}^{(33)}$	
26.3887	660.6421	26.7533	674.9518	27.1308	689.7700
38.1281	768.8991	38.6762	784.5612	39.2439	800.7798
45.1410	886.5331	45.8159	903.0954	46.5147	920.2461
51.7380	1040.9533	52.5415	1058.1655	53.3736	1075.9893
57.9483	1272.3733	58.8824	1290.0636	59.8497	1308.3824
64.0133	1692.6356	65.0833	1711.0794	66.1912	1730.1786
70.5654	2363.6526	71.7870	2382.0994	73.0519	2401.2016
77.7366	3356.9747	79.1287	3373.9638	80.5702	3391.5565
86.0246	4500.2189	87.6162	4513.9670	89.2643	4528.2036
94.9446	5875.9771	96.7571	5887.9549	98.6340	5900.3583
104.6942	7280.2407	106.7535	7293.0448	108.8859	7306.3039
115.9305	8859.0578	118.2765	8874.4325	120.7059	8890.3535
127.9607	10646.0724	130.6207	10664.5475	133.3752	10683.6790
141.0452		144.0520		147.1656	
156.0354		159.4408		162.9671	
171.9182		175.7521		179.7222	
189.0110		193.3096		197.7609	
208.2481		213.0678		218.0588	
230.5613		235.9791		241.5894	
254.9667		261.0343		267.3175	
282.1695		288.9510		295.9734	
311.1328		318.6606		326.4559	
343.3169		351.6489		360.2770	
379.8938		389.1028		398.6390	
419.6383		429.7475		440.2159	
464.8972		475.9584		487.4126	
520.5591		532.6969		545.2659	
583.7482		596.9541		610.6292	

$\mathbf{h}^{(34)}$		$\mathbf{h}^{(35)}$		$\mathbf{h}^{(36)}$	
27.1308	689.7700	23.9366	564.3877	21.3315	462.1326
39.2439	800.7798	34.4409	663.5481	30.5238	551.6292
46.5147	920.2461	40.6017	775.1273	35.7795	656.7763
53.3736	1075.9893	46.3328	925.1754	40.5908	802.1798
59.8497	1308.3824	51.6648	1153.3799	44.9896	1026.9681
66.1912	1730.1786	56.8165	1568.5733	49.1710	1436.7768
73.0519	2401.2016	62.3488	2239.5702	53.6199	2107.7522
80.5702	3391.5565	68.3729	3242.6976	58.4255	3121.2962
89.2643	4528.2036	75.3188	4407.7422	63.9456	4309.5004
98.6340	5900.3583	82.7529	5795.4083	69.8012	5709.8167
108.8859	7306.3039	90.8426	7194.1135	76.1273	7102.6170
120.7059	8890.3535	100.1500	8755.6399	83.3857	8645.7748
133.3752	10683.6790	110.0685	10521.7997	91.0609	10389.7796
147.1656		120.8200		99.3339	
162.9671		133.1296		108.7957	
179.7222		146.1296		118.7333	
197.7609		160.0965		129.3795	
218.0588		175.8286		141.3879	
241.5894		194.1188		155.4043	
267.3175		214.1531		170.7951	
295.9734		236.5540		188.0947	
326.4559		260.4971		206.7047	
360.2770		287.2714		227.7319	
398.6390		317.9494		252.1434	
440.2159		351.6384		279.3993	
487.4126		390.4941		311.4526	
545.2659		438.9145		352.1801	
610.6292		494.9188		400.5515	

$\mathbf{h}^{(37)}$		$\mathbf{h}^{(38)}$		$\mathbf{h}^{(39)}$	
21.3315	462.1326	27.8925	719.6698	29.7770	793.6407
30.5238	551.6292	40.3892	833.5054	43.2228	914.4669
35.7795	656.7763	47.9247	954.8525	51.4132	1040.4671
40.5908	802.1798	55.0527	1111.9538	59.2065	1200.9283
44.9896	1026.9681	61.8016	1345.3458	66.6304	1436.7914
49.1710	1436.7768	68.4268	1768.7165	73.9575	1864.0575
53.6199	2107.7522	75.6043	2439.7458	81.9188	2535.1023
58.4255	3121.2962	83.4789	3427.0548	90.6749	3514.8760
63.9456	4309.5004	92.5899	4556.9300	100.8172	4627.9976
69.8012	5709.8167	102.4211	5925.3857	111.7903	5987.3023
76.1273	7102.6170	113.1887	7333.0579	123.8336	7399.2461
83.3857	8645.7748	125.6078	8922.4786	137.7350	9001.9545
91.0609	10389.7796	138.9331	10722.2823	152.6831	10817.7850
99.3339		153.4482		168.9912	
108.7957		170.0824		187.6854	
118.7333		187.7330		207.5514	
129.3795		206.7427		228.9632	
141.3879		228.1294		253.0436	
155.4043		252.9096		280.9155	
170.7951		279.9956		311.3606	
188.0947		310.1431		345.1983	
206.7047		342.1850		381.0982	
227.7319		377.6867		420.7572	
252.1434		417.8810		465.4847	
279.3993		461.3390		513.5964	
311.4526		510.5247		567.7030	
352.1801		570.6275		633.3708	
400.5515		638.2226		706.4874	

$\mathbf{h}^{(40)}$		$\mathbf{h}^{(41)}$		$\mathbf{h}^{(42)}$	
29.7770	793.6407	20.3611	424.0393	22.7924	519.4746
43.2228	914.4669	29.0646	509.9358	32.7204	614.3904
51.4132	1040.4671	33.9830	612.6866	38.4837	723.1444
59.2065	1200.9283	38.4516	756.3598	43.8108	871.1525
66.6304	1436.7914	42.5029	979.8756	48.7329	1097.8565
73.9575	1864.0575	46.3227	1387.6783	53.4584	1510.6848
81.9188	2535.1023	50.3680	2058.6457	58.5148	2181.6722
90.6749	3514.8760	54.7197	3076.0703	64.0037	3189.3749
100.8172	4627.9976	59.7087	4272.9021	70.3234	4364.5918
111.7903	5987.3023	64.9763	5677.9310	77.0642	5757.8142
123.8336	7399.2461	70.6455	7068.5315	84.3793	7153.9258
137.7350	9001.9545	77.1405	8604.8464	92.7867	8707.3843
152.6831	10817.7850	83.9799	10340.5978	101.7199	10463.8130
168.9912		91.3296		111.3827	
187.6854		99.7306		122.4415	
207.5514		108.5273		134.0965	
228.9632		117.9364		146.6048	
253.0436		128.5576		160.7013	
280.9155		140.9819		177.1143	
311.3606		154.6429		195.1092	
345.1983		170.0421		215.2694	
381.0982		186.6653		236.8701	
420.7572		205.5515		261.1201	
465.4847		227.6285		289.0457	
513.5964		252.4879		319.9091	
567.7030		282.0071		355.7770	
633.3708		319.8687		400.8185	
706.4874		365.3967		453.4702	

$\mathbf{h}^{(43)}$		$\mathbf{h}^{(44)}$		$\mathbf{h}^{(45)}$	
22.7924	519.4746	20.7673	439.9831	28.2648	734.2825
32.7204	614.3904	29.6754	527.3864	40.9490	849.4990
38.4837	723.1444	34.7349	631.1402	48.6139	971.7653
43.8108	871.1525	39.3470	775.5376	55.8732	1129.5303
48.7329	1097.8565	43.5437	999.5860	62.7555	1363.4105
53.4584	1510.6848	47.5149	1408.2283	69.5194	1787.5507
58.5148	2181.6722	51.7291	2079.1990	76.8517	2458.5831
64.0037	3189.3749	56.2707	3094.9994	84.9004	3444.4035
70.3234	4364.5918	61.4820	4288.2201	94.2151	4570.9691
77.0642	5757.8142	66.9957	5691.2766	104.2719	5937.6171
84.3793	7153.9258	72.9399	7082.7979	115.2916	7346.1331
92.7867	8707.3843	79.7544	8621.9768	128.0035	8938.1787
101.7199	10463.8130	86.9436	10361.1826	141.6493	10741.1484
111.3827		94.6798		156.5187	
122.4415		103.5248		173.5598	
134.0965		112.7990		191.6481	
146.6048		122.7258		211.1323	
160.7013		133.9277		233.0511	
177.1143		147.0183		258.4421	
195.1092		161.4033		286.1916	
215.2694		177.5979		317.0681	
236.8701		195.0527		349.8722	
261.1201		214.8350		386.1951	
289.0457		237.8891		427.2849	
319.9091		263.7516		471.6622	
355.7770		294.3314		521.8200	
400.8185		333.3925		583.0221	
453.4702		380.1106		651.7081	

$\mathbf{h}^{(46)}$		$\mathbf{h}^{(47)}$		$\mathbf{h}^{(48)}$	
28.2648	734.2825	29.5172	783.4433	24.1518	572.8341
40.9490	849.4990	42.8322	903.3058	34.7644	672.7928
48.6139	971.7653	50.9323	1028.6645	41.0001	784.9033
55.8732	1129.5303	58.6338	1188.6626	46.8072	935.3351
62.7555	1363.4105	65.9647	1424.1851	52.2162	1163.8217
69.5194	1787.5507	73.1951	1850.9141	57.4480	1579.4600
76.8517	2458.5831	81.0483	2521.9568	63.0698	2250.4586
84.9004	3444.4035	89.6829	3502.7693	69.1946	3252.7255
94.2151	4570.9691	99.6830	4618.2005	76.2582	4415.8572
104.2719	5937.6171	110.4987	5978.7667	83.8228	5802.4783
115.2916	7346.1331	122.3662	7390.1216	92.0581	7201.6713
128.0035	8938.1787	136.0632	8990.9982	101.5347	8764.7150
141.6493	10741.1484	150.7876	10804.6193	111.6386	10532.7048
156.5187		166.8485		122.5948	
173.5598		185.2587		135.1396	
191.6481		204.8193		148.3926	
211.1323		225.9000		162.6338	
233.0511		249.6090		178.6734	
258.4421		277.0547		197.3166	
286.1916		307.0367		217.7346	
317.0681		340.3657		240.5568	
349.8722		375.7338		264.9405	
386.1951		414.8197		292.1895	
427.2849		458.9222		323.3851	
471.6622		506.3924		357.6055	
521.8200		559.8206		397.0231	
583.0221		624.7212		446.0790	
651.7081		697.0767		502.7137	

$\mathbf{h}^{(49)}$		$\mathbf{h}^{(50)}$	
24.1518	572.8341	25.4420	623.4814
34.7644	672.7928	36.7046	728.2265
41.0001	784.9033	43.3886	843.5229
46.8072	935.3351	49.6512	996.2552
52.2162	1163.8217	55.5224	1226.4338
57.4480	1579.4600	61.2349	1644.7392
63.0698	2250.4586	67.3932	2315.7484
69.1946	3252.7255	74.1216	3312.8560
76.2582	4415.8572	81.8914	4464.5166
83.8228	5802.4783	90.2378	5844.8721
92.0581	7201.6713	99.3465	7246.9897
101.5347	8764.7150	109.8381	8819.1315
111.6386	10532.7048	121.0531	10598.0947
122.5948		133.2369	
135.1396		147.1922	
148.3926		161.9621	
162.6338		177.8480	
178.6734		195.7320	
197.3166		216.4920	
217.7346		239.2099	
240.5568		264.5588	
264.9405		291.5840	
292.1895		321.6795	
323.3851		355.9791	
357.6055		393.3857	
397.0231		436.1726	
446.0790		489.0388	
502.7137		549.4540	